Beta-decay studies of ^{8}Be and ^{12}C

SOLVEIG HYLDEGAARD

Department of Physics and Astronomy
Aarhus University, Denmark

PhD thesis
2nd Edition, August 2010

This thesis has been submitted to the Faculty of Science at Aarhus University in order to fulfill the requirements of obtaining a PhD degree in physics. The work has been carried out under the supervision of Karsten V. Riisager and Hans O. U. Fynbo at the Department of Physics and Astronomy (IFA).

Acknowledgments

First of all I would like to thank my two supervisors, Karsten Riisager and Hans Fynbo, for competent supervision. Their doors have always been open and I am grateful for our many discussions and for everything they have taught me. Large parts of this work have been completed in collaboration with two fellow Ph.D. students, Christian Diget and Oliver Kirsebom. I would like to thank both and acknowledge the significance of their hard work for obtaining the results presented in this thesis. I also want to express my thanks to the collaborators who made the experiments I have worked on possible.

I am indebted to the now deceased Fred Barker for our correspondence concerning the *R*-matrix analysis of parts of the work presented here.

Thanks to the subatomic physics group at Aarhus University. It has been a pleasure to be part of the group.

I am grateful to my friend and fellow physicist, Maria F. Jensen, for proofreading part of the thesis.

Last but not least I would like to thank my family for their love and support. In particular my beloved husband, Mads, for believing in me and encouraging me through all phases of this project.

Solveig Hyldegaard,
Aarhus, June 2010.

Contents

List of Publications

List of publications relevant to this thesis

I. **S. Hyldegaard**, C. Forssén, C.Aa. Diget, M. Alcorta, F.C. Barker, B. Bastin, M.J.G. Borge, R. Boutami, S. Brandenburg, J. Büscher, P. Dendooven, P. Van Duppen, T. Eronen, S. Fox, B.R. Fulton, H.O.U. Fynbo, J. Huikari, M. Huyse, H.B. Jeppesen, A. Jokinen, B. Jonson, K. Jungmann, A. Kankainen, O. Kirsebom, M. Madurga, I. Moore, P. Navrátil, T. Nilsson, G. Nyman, G.J.G. Onderwater, H. Penttilä, K. Peräjärvi, R. Raabe, K. Riisager, S. Rinta-Antila, A. Rogachevskiy, A. Saastamoinen, M. Sohani, O. Tengblad, E. Traykov, J.P. Vary, Y. Wang, K. Wilhelmsen, H.W. Wilschut, J. Äystö *Precise branching ratios to unbound ^{12}C states from ^{12}N and ^{12}B β-decays*, Physics Letters B **678**, 459 (2009).

II. C. Aa. Diget, F. C. Barker, M. J. G. Borge, R. Boutami, P. Dendooven, T. Eronen, S. P. Fox, B. R. Fulton, H. O. U. Fynbo, J. Huikari, **S. Hyldegaard**, H. B. Jeppesen, A. Jokinen, B. Jonson, A. Kankainen, I. Moore, A. Nieminen, G. Nyman, H. Penttila, V. F. E. Pucknell, K. Riisager, S. Rinta-Antila, O. Tengblad, Y. Wang, K. Wilhelmsen, and J. Äystö, *Breakup channels for ^{12}C triple-α continuum states*, Physical Review C **80**, 034316 (2009).

III. **S. Hyldegaard**, C. Aa. Diget, M. J. G. Borge, R. Boutami, P. Dendooven, T. Eronen, S. P. Fox, L. M. Fraile, B. R. Fulton, H. O. U. Fynbo, J. Huikari, H. B. Jeppesen, A. S. Jokinen, B. Jonson, A. Kankainen, I. Moore, G. Nyman, H. Penttilä, K. Peräjärvi, K. Riisager, S. Rinta-Antila, O. Tengblad, Y. Wang, K. Wilhelmsen, and J. Äystö, *Branching ratios in the β decays of ^{12}N and ^{12}B*, Physical Review C **80**, 044304 (2009).

IV. **S. Hyldegaard**, M. Alcorta, B. Bastin, M. J. G. Borge, R. Boutami, S. Brandenburg, J. Büscher, P. Dendooven, C. Aa. Diget, P. Van Duppen, T. Eronen, S. P. Fox, L. M. Fraile, B. R. Fulton, H. O. U. Fynbo, J. Huikari, M. Huyse, H. B. Jeppesen, A. S. Jokinen, B. Jonson, K. Jungmann, A.

Kankainen, O. S. Kirsebom, M. Madurga, I. Moore, A. Nieminen, T. Nilsson, G. Nyman, G. J. G. Onderwater, H. Penttilä, K. Peräjärvi, R. Raabe, K. Riisager, S. Rinta-Antila, A. Rogachevskiy, A Saastamoinen, M. Sohani, O. Tengblad, E. Traykov, Y. Wang, K. Wilhelmsen, H. W. Wilschut, and J. Äystö, *R-matrix analysis of the β decays of* ^{12}N *and* ^{12}B, Physical Review C **81**, 024303 (2010).

Other publications

i. J. Büscher, J. Ponsaers, R. Raabe, M. Huyse, P. Van Duppen, F. Aksouh, D. Smirnov, H.O.U. Fynbo, **S. Hyldegaard**, C.Aa. Diget, *β-decay studies with an implantation technique*, Nuclear Instruments and Methods in Physics Research B **266**, 4652 (2008).

ii. O.S. Kirsebom, M. Alcorta, M.J.G. Borge, M. Cubero, C.A. Diget, R. Dominguez-Reyes, L. Fraile, B.R. Fulton, H.O.U. Fynbo, D. Galaviz, G. Garcia, **S. Hyldegaard**, H.B. Jeppesen, B. Jonson, P. Joshi, M. Madurga, A. Maira, A. Muñoz, T. Nilsson, G. Nyman, D. Obradors, A. Perea, K. Riisager, O. Tengblad, M. Turrion, *Observation of γ-delayed 3α breakup of the 15.11 and 12.71 MeV states in* ^{12}C, Physics Letters B **680**, 44 (2009).

iii. O.S. Kirsebom, M. Alcorta, M.J.G. Borge, M. Cubero, C.A. Diget, R. Dominguez-Reyes, L.M. Fraile, B.R. Fulton, H.O.U. Fynbo, **S. Hyldegaard**, B. Jonson, M. Madurga, A. Muñoz Martin, T. Nilsson, G. Nyman, A. Perea, K. Riisager, O. Tengblad, *Breakup of* ^{12}C *resonances into three α particles*. Physical Review C **81**, 064313 (2010).

CHAPTER 1

Introduction

1.1 Origins of light nuclei

The elements making up our bodies and the planet we live on were all created by nuclear processes somewhere in the universe. The light elements, hydrogen, helium and a small amount of lithium were created only a few minutes after the Big Bang in the primordial nucleosynthesis. The remaining lithium and all of beryllium and boron originate from spallation of heavier elements by cosmic radiation. Elements from carbon to uranium were created in the furnaces of stars [Rolfs 1988].

Our sun is fuelled by the fusion of four hydrogen nuclei or protons into a helium nucleus, and because helium is lighter than four protons, energy is released in the process. That hydrogen fusion is the energy source powering the sun was first suggested by Eddington in 1920 after the discovery that helium is slightly lighter than four times the hydrogen mass. The calculated reaction rates were too low however, because the quantum mechanical effect of tunnelling was not known at the time. It took almost 20 years before the nuclear processes could be explained [Bethe 1938, Bethe 1939].

In the nucleosynthesis model by Alpher and Gamow [Alpher 1948], all elements were created in the Big Bang by neutron capture followed by β decay. Later it became known that all isotopes with mass five and eight are unstable (see figure 1.1), and these mass gaps prevented the formation of elements heavier than lithium in the primordial nucleosynthesis.

The alternative was found to be stellar nucleosynthesis. In red giant stars, hydrogen is depleted in the core, and three helium nuclei or α particles fuse to a ^{12}C nucleus by the triple-α process. In a two-step process, first two α particles collide and form a ^{8}Be nucleus. This nucleus is very short-lived and decays back to two α particles in about 10^{-16} seconds. Only if another α par-

ticle immediately collides with the ^{8}Be nucleus a ^{12}C nucleus can be formed. This is not enough however, because the excited ^{12}C nucleus will break up again, if it does not live long enough to de-excite to a bound state. ^{12}C is the fourth most abundant element in the universe after ^{1}H, ^{4}He and ^{16}O, and with the knowledge of the ^{8}Be and ^{12}C nuclei in the beginning of the 1950's, Hoyle was not able to explain the high abundances of ^{12}C and ^{16}O from the calculated triple-α reaction rates at the expected stellar temperatures. This led Hoyle to the prediction of an unbound excited state in ^{12}C just above the triple-α threshold energy [Hoyle 1953]. This state could enhance the reaction rate due to the increased cross section for the fusion of an α particle and a ^{8}Be nucleus. The state was soon after found experimentally at almost the exact energy predicted by Hoyle [Dunbar 1953]. This 0^{+}_{2} state in ^{12}C has since been known as the Hoyle state, and its remarkable discovery established the concept of stellar nucleosynthesis [Burbidge 1957].

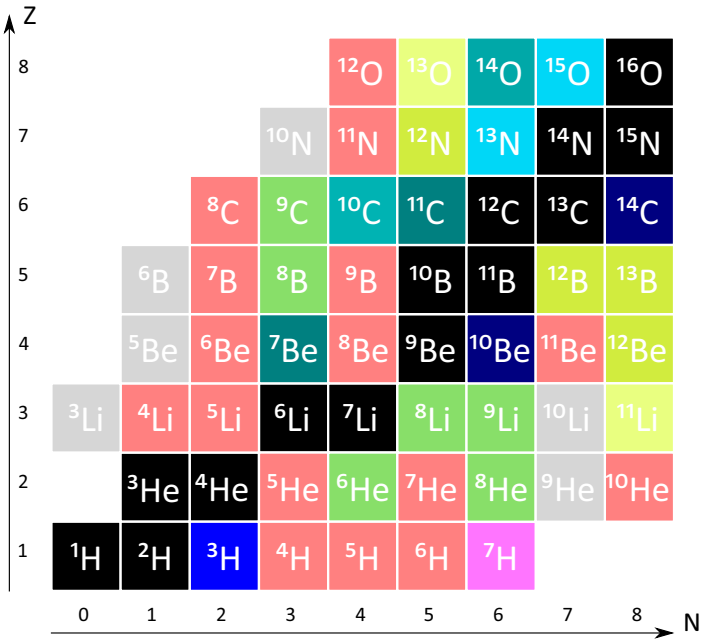

Figure 1.1: Chart of the lightest nuclides. The numbers of neutrons, N, and protons, Z, in the nucleus define the two axes. The Black squares indicate stable nuclides, and all other nuclides shown are unstable with different colours indicating the half-life. The least stable nuclides are light red (gray means the half-life if unknown) [NNDC 2010].

1.2 Nuclear structure

Atomic nuclei are composed of neutrons and protons and in light, stable nuclei the numbers of protons and neutrons are close to equal (except for hydrogen with only one proton) as seen in figure 1.1. The interaction between the nucleons is governed by the strong nuclear interaction and an exact description of even the light nuclei is extremely difficult due to the complex internal structure of the nucleons and complicated internucleon interaction. The most advanced models solve the many-body Schrödinger equation for realistic nucleon-nucleon interaction potentials obtained by fitting nucleon scattering data. This is only possible for the lightest nuclei and the results are not always in correspondence with the experimental data. Three-body forces are often needed to obtain agreement with experimental data, e.g. due to the effect of nucleon excitations [Epelbaum 2009].

Two types of nuclear models have proven very useful for describing nuclear states: The independent particle models and collective models of the nucleus. The nuclear shell model is the quantum mechanical variant of the independent particle models and was developed in analogy to the atomic shell model to explain the occurence of magic numbers - mass numbers for nuclei with unexpectedly high binding energies per nucleon [Mayer 1949, Haxel 1949]. In the independent particle model, the nuclear properties are determined by the least bound nucleons moving in a mean-field potential independently of the remaining nucleons forming an inert core. It is quite surprising that such a model is at all usefull in describing the system of strongly interacting nucleons with no central core, but its usefulness is evident from its ability to explain experimental data. In the collective models the nuclear motion and excitations are correlated or collective. The collective model is useful for deformed nuclei, typically nuclei in between the magic numbers, and for many excited nuclear states. Some collective modes are well described in a cluster model, where one or more groups of nucleons form clusters that can be treated as one entity. The α particle is a prime example of a cluster, and the one relevant for light nuclei [Freer 2007a].

The two isotopes studied in this work are ^{8}Be and ^{12}C. Both are so-called α-conjugate nuclei with an even and equal number of neutrons and protons. The α-conjugate nuclei are particularly stable isotopes and Hafstad and Teller

showed a linear dependency between the binding energy and the number of α-α bonds indicating that their ground states could be described by a cluster of α particles with a constant α-α interaction scaled by the number of bonds [Hafstad 1938]. This picture is now known to be too simplistic. Most ground states are better described in the nuclear shell-model rather than as cluster states. For clustering to arise a lower density is required and clustering is seen to appear when approaching the energy threshold for α break-up [Ikeda 1968]. The ^{8}Be nucleus is unbound in its ground state at 91.8 keV above the 2α threshold and has a clearly clustered 2α structure as seen in figure 1.2. In fact, the ground state of ^{8}Be is quite similar to the Hoyle state of ^{12}C at 0.38 MeV above the 3α threshold, the structure of which is shown in figure 1.3. Both are short-lived cluster states close to an α-particle threshold with spin and parity 0^{+}. Because of their proximity to the threshold the measured energy profiles are highly asymmetric as discussed in detail in later sections. The ground state of ^{12}C is an example of a more compact state described within the nuclear shell-model. ^{12}C with its six protons and six neutrons has filled proton and neutron $p_{3/2}$ sub-shells in its ground state. In advanced no-core shell-model calculations the bound states of ^{12}C are well described, but as seen in figure 1.4 the Hoyle state is missing in the calculations at 7.65 MeV indicating that it is of a more collective than shell-model like type.

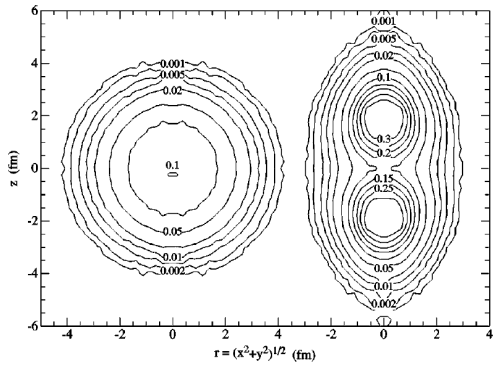

Figure 1.2: Green's function Monte Carlo calculation of the density distribution of the ^{8}Be ground state. The left hand side is in the laboratory frame and the right hand side is in the intrinsic frame [Wiringa 2000].

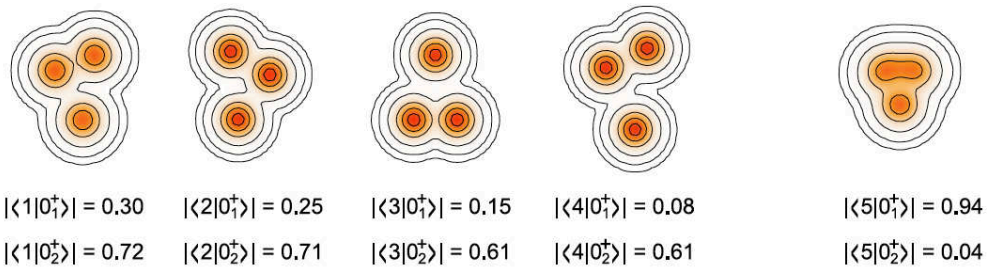

Figure 1.3: Density distributions in Fermionic Molecular Dynamics calculations of ^{12}C. The Hoyle state, 0_2^+, has a large overlap with the four configurations to the left, whereas the ground state, 0_1^+, is of a more compact type as shown to the right [Chernykh 2007]

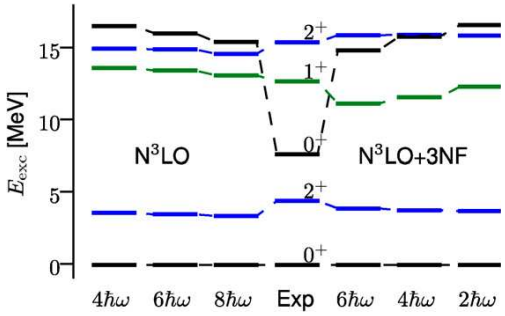

Figure 1.4: No-core shell model calculations for ^{12}C [Hyldegaard 2009b]. The bound states and the unbound 1^+ state are well reproduced, but no states are found close to the Hoyle state energy at 7.65 MeV. Further discussion of these calculations is given in section 4.7.

1.3 Probing light nuclei with β decay

The method used for production of the light nuclei studied in this work is β decay. β decay is a weak interaction process where in β^+ decay a proton in the parent nucleus is converted into a neutron in the daugther nucleus with the emission of a positron and an electron neutrino. In β^- decay a neutron is converted into a proton with the emission of an electron and an electron antineutrino.

$$p \rightarrow n + e^+ + \nu_e \qquad (\beta^+\text{decay}) \qquad (1.1)$$

$$n \rightarrow p + e^- + \bar{\nu}_e \qquad (\beta^-\text{decay}) \qquad (1.2)$$

The available energy for populating excited states in the daughter nucleus, the Q-value, is given by

$$Q_{\beta^+} = (M(A,Z) - M(A,Z-1) - 2m_e)\,c^2 \tag{1.3}$$

$$Q_{\beta^-} = (M(A,Z) - M(A,Z+1))\,c^2 \tag{1.4}$$

for β^+ and β^- decay respectively, where the masses are atomic masses which is the reason for the difference of two electron masses for β^+ decay.

β decay can be classified into two types according to weather or not the spin of the interacting quark inside the nucleon flips its direction. If the spin does not change, the interaction is a Fermi transition, and for allowed decays with orbital angular momentum of the leptons, $l = 0$, the spin and parity of the final state is the same as that of the initial state. If the spin flips over it is a Gamow-Teller transition and the parity in allowed decays is unchanged and the possible spin differences are $\Delta J = 0, \pm 1$ ($0^+ \rightarrow 0^+$ forbidden) [Hodgson 1997].

The selection rules for β decay means that a lot fewer excited states are populated in β decay compared to reaction and scattering. Figure 1.5 illustrates this for the ^{12}C nucleus populated in two reactions compared to ^{12}N β decay. In β decay of ^{12}N the allowed final states are 0^+, 1^+ and 2^+, allowing for much cleaner selection of the interesting 0^+ and 2^+ states (see chapter 4). Another difference is the transition phase space which is a decreasing function of energy going to zero at the Q-value. This limits the applicability of β decay to only low-energy states in the daughter nucleus.

The experimental techniques have undergone dramatic development since the early studies of nuclei. For β-decay studies with halflives of the order 10–20 ms it is a challenge to separate the produced nuclei and transport them to the detector setup before they decay. This was not possible when the first β-decay studies were performed [Cook 1958, Wilkinson 1963, Schwalm 1966, Wilkinson 1971]. The α particles from β-delayed breakup were detected directly as they were emitted from the target. The first isotope separator connected directly to an accelerator was developed for the Copenhagen Cyclotron at Universitetets Institut for Teoretisk Fysik (the later Niels Bohr Institute) in Copenhagen in 1951 by Otto Kofoed-Hansen and Karl Ove Nielsen [Krige 1996]. The technique, now known as Isotope Separation On-Line (ISOL), is used

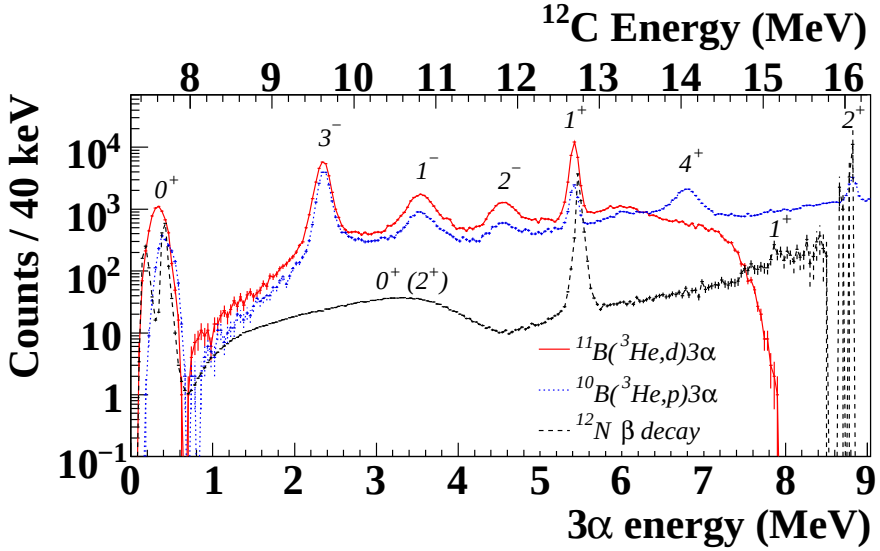

Figure 1.5: 3α sum energy spectra from the reactions ^{3}He+^{11}B $\rightarrow d + \alpha + \alpha + \alpha$ and ^{3}He+^{10}B $\rightarrow p + \alpha + \alpha + \alpha$ compared to β-delayed 3α breakup. The reaction data is from [Kirsebom 2009] and the β-decay results will be discussed in chapter 4. The β-decay spectrum shown in this figure has been corrected for the β-decay phase space and scaled for comparison. The spectrum for the ^{11}B reaction drops down at 15 MeV because the deuterons have too low energy to be detected.

at many research facilities around the world, arguably the principle facility is ISOLDE at CERN, a joint European facility on the Franco-Swiss border near Geneva. The radioactive nuclei are produced by protons impinging on a thick high-temperature target via spallation, fission or fragmentation reactions. Subsequently the produced isotopes diffuse out of the target after which they are ionised, accelerated and mass-separated. More than 600 isotopes with half-lives down to milliseconds have been produced and separated at ISOLDE [ISOLDE 2010]. However some isotopes can not diffuse out of a thick target and in order to produce them a thin target is required. The Ion Guide Isotope Separator On Line (IGISOL) technique was developed in Finland in 1981 at the University of Jyväskylä. Here, a thin target is used and the reaction products recoiling out of the target are stopped in a gas, transported by the gas flow through a differential pumping system, after which they are accelerated and mass-separated. With the IGISOL technique, isotopes with

half-lives down to the sub-millisecond range can be studied. A different technique relevant for this work is isotope production using inverse kinematics followed by mass-separation. This methods yields a high-energy beam useful for implantation experiments as presented in section 4.4.

Not only isotope separation techniques but also detectors have undergone significant development. The Double Sided Si Strip Detectors (DSSSDs) used in this work provide both high energy and spatial resolution allowing for complete kinematics measurements as described in sections 3.2 and 4.2. A smaller detector with increased segmentation has been used for implantation measurements (section 4.4).

1.4 The *R*-matrix

The theoretical framework for treating nuclear resonances was developed starting in the 1930's with Bohr's compound nucleus mechanism. Nuclear resonances were first observed as peaks in the cross section for scattering reactions, with the lifetime of the resonance, τ inversely proportional to the width of the peak, $\Gamma = \hbar/\tau$. The compound nucleus mechanism could explain why the resonances were so long lived as experiments had shown. The idea is, that the projectile energy is shared among the individual nucleons in a collision due to the strong, short-range interaction until a statistical equilibrium is obtained. Due to the constant fluctuations in the energy and spatial distributions of the nucleons, there will be some statistical probability of the compound nucleus to split up into smaller constituents. A less probable scenario is the conversion of the collective exciation energy into radiation and subsequent deexcitation, and it is this very small radiative width of the Hoyle state which makes the triple-α process possible. Rigorous theories of nuclear reactions were developed by Kapur, Peierls, Breit, Wigner and Eisenbud among others and the variant used in this work is the *R*-matrix theory as presented by Lane and Thomas in their review from 1958 [Lane 1958]. The formalism was later generalised to the treatment of β decay followed by two-body breakup by Barker [Barker 1969]. In this work the theory will be taken to its limits with a formalism developed for β-delayed three-body breakup via short-lived intermediate states.

1.5 Outline

The work presented in this thesis is the partial analysis of two experiments performed at the IGISOL facility of the Jyväskylä Accelerator Laboratory (JYFL), Finland, and the full analysis of an experiment performed at the KVI in Groningen, the Netherlands. The first experiment was a complete kinematics experiment studying β decay of ^{12}N and ^{12}B at JYFL in 2004. The analysis of the data from this experiment constitutes the majority of the Ph.D.-work by C. Aa. Diget. A parallel analysis of the single-α data will be presented in section 4.2. A similar experiment was performed at JYFL in 2008, studying the β-decay of ^{8}B. These data have been analysed by O. S. Kirsebom to extract accurate final state distributions. The R-matrix analysis of these spectra will be presented in chapter 3. The full analysis of an implantation experiment for β-decay studies of ^{12}C performed at KVI in 2006 will be presented in chapter 4. The R-matrix model for the mass 8 breakup is simpler than for mass 12, so the analysis of the ^{8}B data will be presented first. The R-matrix theory applied to the analysis will be presented in chapter 2. The possibility of a direct decay component in both the $A = 8$ and $A = 12$ data will be discussed in chapter 5. Finally the work will be summarised in chapter 6.

CHAPTER 2

R-matrix theory

The *R*-matrix formalism has been used to analyse the beta-delayed breakups studied in this work. In this chapter the formalism will be derived starting with the basic theory for nuclear scattering processes involving an unlimited number of reaction channels and energy levels. This will be followed by a generalisation of the theory to encompass beta decay and subsequently the formalism for sequential decay via broad intermediate states will be presented. The *R*-matrix theory was first developed to treat nuclear resonance reactions, but has over the years been applied to many different branches of physics. Some of these alternative applications will be discussed in the final section of this chapter.

2.1 The many-channel, multi-level *R*-matrix theory

The notation used in the following will largely be the same as that of the standard *R*-matrix reference by Lane and Thomas [Lane 1958]. The derivation will be performed for the general many-channels, multi-level scattering process, and large parts of it follows the reviews by Vogt [Vogt 1962, Vogt 2004].

The essence of the *R*-matrix theory is the separation of configuration space into an internal and an external region. The internal region is where the nuclear interactions take place, such as formation of a compound nucleus in resonant reactions. In the external region the interactions are purely Coulomb. The compound nucleus can be formed and decay through various possible channels, which are defined by the two nuclei in the channel and their internal and relative quantum numbers.

To find the cross section of a nuclear process the exact solutions for the wave function in the external region are found and matched to the wave functions in the internal region. The wave functions in the internal region

are constrained by boundary conditions on their logarithmic derivatives. A discussion of the boundary conditions will follow later in this chapter.

First, we consider the solutions in the external region. The wave function in the external region for a nuclear process involving the channels, c, can be factorised as

$$\Psi = \sum_c \psi_c u_c(r), \tag{2.1}$$

where ψ_c is the channel wave function containing all spin and angular momentum dependencies, and $u_c(r)$ is the radial wave function, which is a solution to the radial Schrödinger equation,

$$-\frac{\hbar^2}{2\mu}\frac{d^2u_c}{dr^2} + \frac{l(l+1)}{r^2}u_c + (V_C - E)u_c = 0, \tag{2.2}$$

where V_C is the Coulomb potential. The solutions to this equation are the regular (F_c) and irregular (G_c) Coulomb functions, and in terms of these one can write the incoming wave,

$$I_c = (G_c - iF_c)e^{i\omega_c}, \tag{2.3}$$

and outgoing wave,

$$O_c = (G_c + iF_c)e^{-i\omega_c}, \tag{2.4}$$

where ω_c is the Coulomb phase shift. The radial wave function is a linear combination,

$$u_c = v_c^{-1/2}\left(x_c O_c + y_c I_c\right), \tag{2.5}$$

where x_c and y_c are amplitudes of the incoming and outgoing waves and v_c is the relative velocity. The collision matrix, $\mathbf{U}$, is defined by the relation between the amplitudes:

$$x_{c'} = -\sum_c U_{c'c}y_c. \tag{2.6}$$

Let us now consider the internal region. The Schrödinger equation for the full wave function is

$$H\Psi = E\Psi, \tag{2.7}$$

and the mutually orthogonal eigenfunctions, X_λ, at energy eigenvalues, E_λ, fulfil

$$HX_\lambda = E_\lambda X_\lambda. \tag{2.8}$$

The boundary condition constrains the logarithmic derivatives of the eigenfunctions to a real constant, B_c, for each channel

$$a_c \frac{dX_\lambda}{dr}\bigg|_{r=a_c} = B_c X_\lambda(a_c), \tag{2.9}$$

where a_c is the channel radius of the bounding sphere separating the internal and external regions. The full wave function can be expanded in terms of the internal eigenfunctions as

$$\Psi = \sum_\lambda C_\lambda X_\lambda, \tag{2.10}$$

and the coefficients C_λ are given by

$$C_\lambda = \int_\tau X_\lambda^* \Psi d\tau, \tag{2.11}$$

integrated over the internal region, τ.

2.2 Collision matrix

The physics of the theory has now been presented and the collision matrix can be derived. This requires some mathematical manipulations, and in the process, the R-matrix will be introduced. In the final expression for the collision matrix each internal eigenstate or level, λ, will contribute via its energy, E_λ, and reduced width amplitudes, $\gamma_{\lambda c}$, and the energy dependency will be contained in the shift and penetration functions which only depend on properties of the Coulomb wave-functions on the boundary surface.

First equation 2.7 is multiplied by X_λ^*,

$$X_\lambda^* H\Psi = X_\lambda^* E\Psi, \tag{2.12}$$

and the complex conjugate of equation 2.8 by Ψ,

$$(HX_\lambda)^*\Psi = E_\lambda X_\lambda^* \Psi. \tag{2.13}$$

Subtracting equation 2.12 from 2.13,

$$(E_\lambda - E)X_\lambda^* \Psi = (HX_\lambda)^* \Psi - X_\lambda^* H\Psi, \tag{2.14}$$

and inserting the Hamiltonian,

$$H = -\frac{\hbar^2}{2\mu}\nabla^2 + V, \tag{2.15}$$

where the interaction term, V, is assumed to be self-adjoined, and therefore not to contribute to the right hand side of equation 2.14. Integrating over the internal region, τ, equation 2.14 becomes

$$(E_\lambda - E)\int_\tau X_\lambda^* \Psi d\tau = \frac{\hbar^2}{2\mu}\int_\tau (X_\lambda^* \nabla^2 \Psi - (\nabla^2 X_\lambda)^* \Psi) d\tau. \tag{2.16}$$

Applying Green's theorem to the right hand side transforms the volume integral into a surface integral. Using equation 2.11, the coefficients, C_λ can now be written as

$$C_\lambda = \frac{\hbar^2}{2\mu}\frac{1}{E_\lambda - E}\int_S \left(X_\lambda^* \nabla_n \Psi - (\nabla_n X_\lambda)^* \Psi\right) dS, \tag{2.17}$$

where ∇_n is the gradient normal to the boundary surface. The wave function, Ψ, and its gradient, $\nabla_n \Psi$, must equal the solutions for the external region at the boundary, $\Psi = \sum_c \psi_c u_c$, and $\nabla_n \Psi = \sum_c \psi_c \nabla_n u_c = \sum_c \psi_c du_c/dr$. The boundary condition on the internal eigenfunctions is applied to the last term in the integral:

$$\begin{aligned} C_\lambda &= \frac{\hbar^2}{2\mu}\frac{1}{E_\lambda - E}\sum_c \int_S \left(X_\lambda^* \psi_c \frac{du_c}{dr} - a_c^{-1} B_c X_\lambda^* \psi_c u_c\right) dS \\ &= \sum_c \frac{\hbar^2}{2\mu a_c}\frac{1}{E_\lambda - E}\left(a_c \left.\frac{du_c}{dr}\right|_{r=a_c} - B_c u_c(a_c)\right)\int_S X_\lambda^* \psi_c dS \\ &= \sum_c \left(\frac{\hbar^2}{2\mu a_c}\right)^{1/2} \frac{\gamma_{\lambda c}}{E_\lambda - E}\left(a_c \left.\frac{du_c}{dr}\right|_{r=a_c} - B_c u_c(a_c)\right) \end{aligned} \tag{2.18}$$

where the definition of the reduced width amplitude,

$$\gamma_{\lambda c} = \left(\frac{\hbar^2}{2\mu a_c}\right)^{1/2}\int_S X_\lambda^* \psi_c dS, \tag{2.19}$$

has been introduced. Now this is used in equation 2.10, which is multiplied by $\psi^*_{c'}$ and integrated over the boundary surface:

$$\int_S \psi^*_{c'} \Psi dS = \sum_\lambda C_\lambda \int_S \psi^*_{c'} X_\lambda dS. \tag{2.20}$$

The integral on the right hand side is recognised as $\gamma^*_{\lambda c'}$ (apart from the front factor), but as it turns out that the reduced width amplitudes are real, $\gamma^*_{\lambda c'} = \gamma_{\lambda c'}$. The left hand side is

$$\int_S \psi^*_{c'} \Psi dS = \int_S \psi^*_{c'} \sum_c \psi_c u_c dS = \sum_c u_c(a_c) \int_S \psi^*_{c'} \psi_c dS = \sum_c u_c(a_c) \delta_{c'c} = u_{c'}(a_{c'}), \tag{2.21}$$

where the orthonormality of the channel wave functions has been applied. Inserting the results into equation 2.20 one obtains the fundamental R-matrix relation

$$\begin{aligned} u_{c'}(a_{c'}) &= \sum_{\lambda c} \left(\frac{a_{c'}}{a_c}\right)^{1/2} \frac{\gamma_{\lambda c'} \gamma_{\lambda c}}{E_\lambda - E} \left(a_c \left. \frac{du_c}{dr} \right|_{r=a_c} - B_c u_c(a_c) \right) \\ &= \sum_c \left(\frac{a_{c'}}{a_c}\right)^{1/2} R_{c'c} \left(a_c \left. \frac{du_c}{dr} \right|_{r=a_c} - B_c u_c(a_c) \right), \end{aligned} \tag{2.22}$$

with the R-matrix defined as

$$R_{c'c} = \sum_\lambda \frac{\gamma_{\lambda c'} \gamma_{\lambda c}}{E_\lambda - E}. \tag{2.23}$$

To simplify the expressions the dimensionless derivative rd/dr will be denoted by a prime, and it will not be given explicitly that the functions are evaluated at the boundary. In simplified notation, equation 2.22 is given by

$$a_{c'}^{-1/2} u_{c'} = \sum_c a_c^{-1/2} R_{c'c} \left(u'_c - B_c u_c \right). \tag{2.24}$$

Inserting the solutions for the external wave functions in terms of incoming and outgoing waves,

$$(a_{c'} v_{c'})^{-1/2} \left(x_{c'} O_{c'} + y_{c'} I_{c'} \right) = \sum_c (a_c v_c)^{-1/2} R_{c'c} \left((x_c O'_c + y_c I'_c) - B_c \left(x_c O_c + y_c I_c \right) \right),$$

rearranging the outgoing and incoming terms on each side and using $\rho_c = k_c a_c = \mu_c v_c a_c/\hbar$, where μ_c is the reduced mass,

$$\rho_{c'}^{-1/2} x_{c'} O_{c'} - \sum_c \rho_c^{-1/2} R_{c'c}(O'_c - B_c O_c) x_c = -\rho_{c'}^{-1/2} y_{c'} I_{c'} - \sum_c \rho_c^{-1/2} R_{c'c}(I'_c - B_c I_c) y_c,$$

and, after some manipulations,

$$\sum_c \rho_c^{-1/2} O_c \left(\delta_{c'c} - R_{c'c}\left(\frac{O'_c}{O_c} - B_c\right)\right) x_c = -\sum_c \rho_c^{-1/2} I_c \left(\delta_{c'c} - R_{c'c}\left(\frac{I'_c}{I_c} - B_c\right)\right) y_c. \tag{2.25}$$

The logarithmic derivative of the outgoing wave is denoted by

$$L_c \equiv \frac{O'_c}{O_c} = \rho_c \frac{dO_c}{d\rho_c}\frac{1}{O_c} = S_c + iP_c, \tag{2.26}$$

and can be calculated using equation 2.4. The real part, S_c is called the shift function and is given by

$$S_c = \rho_c \left(F_c \frac{dF_c}{d\rho_c} + G_c \frac{dG_c}{d\rho_c}\right) \frac{1}{F_c^2 + G_c^2}, \tag{2.27}$$

whereas the imaginary part, P_c, is called the penetration function,

$$P_c = \frac{\rho_c}{F_c^2 + G_c^2}, \tag{2.28}$$

where the identity

$$\frac{dF_c}{d\rho_c} G_c - \frac{dG_c}{d\rho_c} F_c = 1 \tag{2.29}$$

has been applied. See section A.1 in the appendix for details about the shift and penetration functions. The logarithmic derivative of the incoming wave function (equation 2.3) is the complex conjugate L_c^*. The collision matrix can now be found from equation 2.25 using the definition, equation 2.6, and changing to matrix form,

$$\begin{aligned} \mathbf{U} &= [(\mathbf{1} - \mathbf{R}\mathbf{L}^0)\rho^{-1/2}\mathbf{O}]^{-1}(\mathbf{1} - \mathbf{R}\mathfrak{L}^0)\mathbf{I}\rho^{-1/2} \\ &= \rho^{1/2}\mathbf{O}^{-1}[\mathbf{1} - \mathbf{R}\mathbf{L}^0]^{-1}(\mathbf{1} - \mathbf{R}\mathfrak{L}^0)\mathbf{I}\rho^{-1/2}, \end{aligned} \tag{2.30}$$

where the following definitions have been introduced:

$$\mathbf{L}^0 = \mathbf{L} - \mathbf{B}, \tag{2.31}$$

$$\mathfrak{L}^0 = \mathfrak{L} - \mathbf{B}, \tag{2.32}$$

$$\mathfrak{L}_c = L_c^*. \tag{2.33}$$

The components of the collision matrix are

$$U_{c'c} = \rho_{c'}^{1/2} O_{c'}^{-1} \sum_{c''} [\mathbf{1} - \mathbf{R}\mathbf{L}^0]^{-1}_{c'c''} (\delta_{c''c} - R_{c''c}\mathfrak{L}^0_c) I_c \rho_c^{-1/2} \tag{2.34}$$

To finally remove the last factor including directly the incoming and outgoing waves one rewrites the factor,

$$\left(\frac{\rho_{c'}}{\rho_c}\right)^{1/2} \frac{I_c}{O_{c'}} = \left(\frac{P_{c'}(F_{c'}^2 + G_{c'}^2)}{P_c(F_c^2 + G_c^2)}\right)^{1/2} \frac{G_c - iF_c}{G_{c'} + iF_{c'}} e^{i(\omega_c + \omega_{c'})}. \tag{2.35}$$

The Coulomb functions can be rewritten in terms of an amplitude, A_c, and the so-called hard-sphere scattering phase shift, ϕ_c, as $F_c = A_c \sin\phi_c$ and $G_c = A_c \cos\phi_c$, so that $\phi_c = \tan^{-1}(F_c/G_c)$ giving

$$\frac{G_c + iF_c}{(F_c^2 + G_c^2)^{1/2}} = e^{i\phi_c} \tag{2.36}$$

to finally obtain

$$\left(\frac{\rho_{c'}}{\rho_c}\right)^{1/2} \frac{I_c}{O_{c'}} = \left(\frac{P_{c'}}{P_c}\right)^{1/2} e^{i(\omega_c + \omega_{c'} - \phi_c - \phi_{c'})} = \left(\frac{P_{c'}}{P_c}\right)^{1/2} \Omega_c \Omega_{c'}, \tag{2.37}$$

where $\Omega_c = I_c/O_c = e^{i(\omega_c - \phi_c)}$. Inserting the result,

$$U_{c'c} = e^{i(\omega_c + \omega_{c'} - \phi_c - \phi_{c'})} P_{c'}^{1/2} \sum_{c''} [\mathbf{1} - \mathbf{R}\mathbf{L}^0]^{-1}_{c'c''} (\delta_{c''c} - R_{c''c}\mathfrak{L}^0_c) P_c^{-1/2}, \tag{2.38}$$

or in matrix form

$$\mathbf{U} = \mathbf{\Omega}\mathfrak{P}^{1/2}[\mathbf{1} - \mathbf{R}\mathbf{L}^0]^{-1}(\mathbf{1} - \mathbf{R}\mathfrak{L}^0)\mathfrak{P}^{-1/2}\mathbf{\Omega} \tag{2.39}$$

$$= \mathbf{\Omega}\mathbf{W}\mathbf{\Omega}, \tag{2.40}$$

where

$$\mathbf{W} = \mathfrak{P}^{1/2}[\mathbf{1} - \mathbf{R}\mathbf{L}^0]^{-1}(\mathbf{1} - \mathbf{R}\mathfrak{L}^0)\mathfrak{P}^{-1/2} \tag{2.41}$$

$$= \mathbf{1} + \mathfrak{P}^{1/2}[\mathbf{1} - \mathbf{R}\mathbf{L}^0]^{-1}\mathbf{R}\mathfrak{P}^{1/2}\mathbf{w}. \tag{2.42}$$

and $\mathfrak{P}_c = P_c$ and $\mathbf{w}_c = w_c = 2i$. The latter form of $\mathbf{W}$ is easily verified by rewriting the unit matrix as $\mathfrak{P}^{1/2}[\mathbf{1} - \mathbf{R}\mathbf{L}^0]^{-1}(\mathbf{1} - \mathbf{R}\mathbf{L}^0)\mathfrak{P}^{-1/2}$, and inserting into equation 2.42.

2.2.1 Level-matrix form of the collision matrix

For systems with many channels, c, the problem of inverting the channel-matrix, $\mathbf{1} - \mathbf{RL}^0$, may be replaced by the inversion of a level-matrix, $\mathbf{A}^{-1}$, with the number of rows and columns equal to the number of levels. The level-matrix form of the collision matrix is, in component form:

$$U_{c'c} = e^{i(w_{c'}+w_c-\phi_{c'}-\phi_c)}\left(\delta_{c'c} + 2iP_{c'}^{1/2}P_c^{1/2}\sum_{\lambda\mu}\gamma_{\lambda c'}\gamma_{\mu c}A_{\lambda\mu}\right). \tag{2.43}$$

To prove this, it is assumed that the channel-matrix form of the collision matrix is equal to equation 2.43, and a solution for $\mathbf{A}^{-1}$ is found. Using the form of $\mathbf{W}$ in equation 2.42 this requires that

$$\sum_{c''}(\mathbf{1} - \mathbf{RL}^0)^{-1}_{c'c''}R_{c''c} = \sum_{\lambda\mu}\gamma_{\lambda c'}\gamma_{\mu c}A_{\lambda\mu}. \tag{2.44}$$

First both sides are multiplied by $[\mathbf{1} - \mathbf{RL}^0]$ from the left. The left hand side becomes just $R_{c'c}$ and the right hand side becomes

$$\begin{aligned}&\sum_{c''}(\delta_{c'c''} - R_{c'c''}L^0_{c''})\sum_{\lambda\mu}\gamma_{\lambda c''}\gamma_{\mu c}A_{\lambda\mu}\\ &= \sum_{\lambda\mu}\gamma_{\lambda c'}\gamma_{\mu c}A_{\lambda\mu} - \sum_{\nu c''}\frac{\gamma_{\nu c'}\gamma_{\nu c''}}{E_\nu - E}L^0_{c''}\sum_{\lambda\mu}\gamma_{\lambda c''}\gamma_{\mu c}A_{\lambda\mu}.\end{aligned} \tag{2.45}$$

Combining the two sides and rearranging the indices,

$$0 = \sum_{\lambda\mu}\frac{\gamma_{\lambda c'}\gamma_{\mu c}}{E_\lambda - E}\left(-\delta_{\lambda\mu} + (E_\lambda - E)A_{\lambda\mu} - \sum_{\nu c''}\gamma_{\lambda c''}\gamma_{\nu c''}L^0_{c''}A_{\nu\mu}\right). \tag{2.46}$$

For the equality to hold for all values of $\gamma_{\lambda c}$ the parenthesis must be zero,

$$\begin{aligned}0 &= -\delta_{\lambda\mu} + (E_\lambda - E)A_{\lambda\mu} - \sum_{\nu c''}\gamma_{\lambda c''}\gamma_{\nu c''}L^0_{c''}A_{\nu\mu}\\ &= -\delta_{\lambda\mu} + \sum_\nu\left(\delta_{\lambda\nu}(E_\nu - E)A_{\nu\mu} - \sum_{c''}\gamma_{\lambda c''}\gamma_{\nu c''}L^0_{c''}A_{\nu\mu}\right)\\ &= -\delta_{\lambda\mu} + \sum_\nu A_{\nu\mu}\left(\delta_{\lambda\nu}(E_\nu - E) - \sum_{c''}\gamma_{\lambda c''}\gamma_{\nu c''}L^0_{c''}\right).\end{aligned} \tag{2.47}$$

The equality becomes true if the parenthesis is $A^{-1}_{\lambda\nu}$. The level-matrix form is therefore equivalent to the channel-matrix form of the collision matrix with

$$A^{-1}_{\lambda\mu} = \delta_{\lambda\mu}(E_\lambda - E) - \sum_c \gamma_{\lambda c}\gamma_{\mu c}L^0_c \tag{2.48}$$

$$= \delta_{\lambda\mu}(E_\lambda - E) - \sum_c \gamma_{\lambda c}\gamma_{\mu c}(S_c - B_c + iP_c). \tag{2.49}$$

2.3 Cross sections

The collision matrix is not directly measurable. The quantity typically measured in reaction or scattering experiments is the differential or integrated cross section. The integrated cross section for an incident particle of type α with spin s, and outgoing type α' and spin s', is given in [Lane 1958, VIII (3.2a)]:

$$\sigma_{\alpha s,\alpha' s'} = \frac{\pi}{k^2_\alpha(2s+1)}\sum_{Jll'}(2J+1)|T^J_{\alpha' s' l',\alpha s l}|^2, \tag{2.50}$$

where T is defined below (2.3) in the same chapter,

$$T_{\alpha' s' l',\alpha s l} = e^{2i\omega_{\alpha' l'}}\delta_{\alpha' s' l',\alpha s l} - U^J_{\alpha' s' l',\alpha s l}. \tag{2.51}$$

To simplify the notation in the following, c denotes the channel $\alpha s l$ and superscript, J, is omitted. The essential part of the cross section is then:

$$\sigma_{cc'} \propto |e^{2i\omega_{c'}}\delta_{c'c} - U_{c'c}|^2. \tag{2.52}$$

The second form of $\mathbf{W}$ (equation 2.42) is used in the collision matrix, denoting the second term of $\mathbf{W}$ by $\mathfrak{W}$. Inserting this into the above,

$$\sigma_{cc'} \propto |e^{2i\omega_{c'}}\delta_{c'c} - \Omega_{c'}(\delta_{c'c} + \mathfrak{W}_{c'c})\Omega_c|^2 = |e^{2i\omega_{c'}}\delta_{c'c} - \Omega_{c'}\Omega_c\delta_{c'c} + \Omega_{c'}\Omega_c\mathfrak{W}_{c'c}|^2. \tag{2.53}$$

First, the cross section for $c \neq c'$ is considered:

$$\begin{aligned}\sigma_{cc'}(c \neq c') &\propto |\Omega_{c'}\Omega_c\mathfrak{W}_{c'c}|^2 = |\mathfrak{W}_{c'c}|^2 \\ &= |[\mathfrak{P}^{1/2}(\mathbf{1} - \mathbf{RL}^0)^{-1}\mathbf{R}\mathfrak{P}^{1/2}\mathbf{w}]_{c'c}|^2 \\ &= 4P_cP_{c'}|\sum_{c''}(\mathbf{1} - \mathbf{RL}^0)^{-1}_{c'c''}R_{c''c}|^2.\end{aligned} \tag{2.54}$$

To get the level-matrix form equation 2.44 is applied, which leads directly to:

$$\sigma_{cc'}(c \neq c') \propto 4P_cP_{c'}|\sum_{\lambda\mu}\gamma_{\lambda c}\gamma_{\mu c'}A_{\lambda\mu}|^2. \tag{2.55}$$

For $c = c'$ the cross section is:

$$\begin{aligned}
\sigma_{cc} \propto & |e^{2i\omega_c} - \Omega_c^2 + \Omega_c^2\mathfrak{W}_{cc}|^2 \\
= & |1 - e^{-2i\phi_c} + e^{-2i\phi_c}\mathfrak{W}_{cc}|^2 \\
= & (1 - e^{-2i\phi_c} + e^{-2i\phi_c}\mathfrak{W}_{cc})(1 - e^{2i\phi_c} + e^{2i\phi_c}\mathfrak{W}^*_{cc}) \\
= & 1 - e^{2i\phi_c} + e^{2i\phi_c}\mathfrak{W}^*_{cc} - e^{-2i\phi_c} + 1 - \mathfrak{W}^*_{cc} + e^{-2i\phi_c}\mathfrak{W}_{cc} - \mathfrak{W}_{cc} + |\mathfrak{W}_{cc}|^2 \\
= & 2 - e^{2i\phi_c} - e^{-2i\phi_c} + (e^{-2i\phi_c} - 1)\mathfrak{W}_{cc} + (e^{2i\phi_c} - 1)\mathfrak{W}^*_{cc} + |\mathfrak{W}_{cc}|^2 \\
= & 2(1 - \cos 2\phi_c) \\
& + 2i(e^{-2i\phi_c} - 1)P_c\sum_{c'}(\mathbf{1} - \mathbf{RL}^0)^{-1}_{cc'}R_{c'c} \\
& - 2i(e^{2i\phi_c} - 1)P_c\sum_{c'}(\mathbf{1} - \mathbf{R}\mathfrak{L}^0)^{-1}_{cc'}R_{c'c} \\
& + 4P_c^2|\sum_{c'}(\mathbf{1} - \mathbf{RL}^0)^{-1}_{cc'}R_{c'c}|^2.
\end{aligned} \tag{2.56}$$

This can be rewritten to

$$\begin{aligned}
\sigma_{cc} \propto & 4\sin^2\phi_c \\
& + 4P_c\left[\sin 2\phi_c \mathrm{Re}\left(\sum_{c'}(\mathbf{1} - \mathbf{RL}^0)^{-1}_{cc'}R_{c'c}\right)\right. \\
& \left. + (1 - \cos 2\phi_c)\mathrm{Im}\left(\sum_{c'}(\mathbf{1} - \mathbf{RL}^0)^{-1}_{cc'}R_{c'c}\right)\right] \\
& + 4P_c^2|\sum_{c'}(\mathbf{1} - \mathbf{RL}^0)^{-1}_{cc'}R_{c'c}|^2.
\end{aligned} \tag{2.57}$$

Using equation 2.44 the equivalent level-matrix form is

$$\begin{aligned}\sigma_{cc} \propto & 4\sin^2\phi_c \\ & + 4P_c\left[\sin 2\phi_c \mathrm{Re}\left(\sum_{\lambda\mu}\gamma_{\lambda c}\gamma_{\mu c}A_{\lambda\mu}\right)\right. \\ & \left. + (1-\cos 2\phi_c)\mathrm{Im}\left(\sum_{\lambda\mu}\gamma_{\lambda c}\gamma_{\mu c}A_{\lambda\mu}\right)\right] \\ & + 4P_c^2\left|\sum_{\lambda\mu}\gamma_{\lambda c}\gamma_{\mu c}A_{\lambda\mu}\right|^2.\end{aligned} \tag{2.58}$$

For the single level case, this expression is equivalent to equation (1.14) in [Lane 1958, XII].

In the case of a single level, λ, the level-matrix cross sections can be simplified by substituting

$$\sum_{\lambda\lambda'}\gamma_{\lambda c}\gamma_{\lambda' c'}A_{\lambda\lambda'} = \frac{\gamma_{\lambda c}\gamma_{\lambda c'}}{E_\lambda - E - \sum_c \gamma_{\lambda c}^2(S_c - B_c + iP_c)}, \tag{2.59}$$

and in the case of only one channel the following can be used:

$$\sum_{c''}(\mathbf{1} - \mathbf{RL}^0)^{-1}_{cc''}R_{c''c'} = \frac{\sum_\lambda \gamma_{\lambda c}\gamma_{\lambda c'}/(E_\lambda - E)}{1 - (S_c - B_c + iP_c)\sum_\lambda \gamma_{\lambda c}^2/(E_\lambda - E)}. \tag{2.60}$$

2.4 R-matrix formalism applied to β decay

The formalism for scattering and reactions can be applied to β-decay in a way analogous to the inclusion of photon channels in [Lane 1958, XIII 3]. The level-matrix form of the collision matrix can be written as

$$U_{cc'}(c \neq c') = i\Omega_c\Omega_{c'}\sum_{\lambda\mu}A_{\lambda\mu}\Gamma^{1/2}_{\lambda c}\Gamma^{1/2}_{\mu c'}, \tag{2.61}$$

where $\Gamma_{\lambda c} = 2P_c\gamma^2_{\lambda c}$. According to [Lane 1958, XIII, (3.9)] the collision matrix element for incoming channel, e, and outgoing photon channel, p, is

$$U_{ep} = i\Omega_e\Omega_p\sum_{\lambda\mu}A_{\lambda\mu}\Gamma^{1/2}_{\lambda e}\Gamma^{1/2}_{\mu p}, \tag{2.62}$$

where Ω_p is the photon phase factor and $\Gamma_{\lambda p}$ the width amplitude. For β decay the corresponding substitution is

$$(\Omega_c \Gamma_{\lambda c}^{1/2})^2 = f_\beta g_{\lambda x}^2, \tag{2.63}$$

where $g_{\lambda x}$ is the beta strength parameter with $x = F$ or G corresponding to Fermi and Gamow-Teller transitions, and f_β is the integrated Fermi function [Barker 1969, App. III] (see section A.3 in the appendix). The cross section is thus replaced by a decay probability:

$$w_c(E) = C^2 f_\beta P_c \sum_{\text{x=F,GT}} |\sum_{\lambda\mu} g_{\lambda x} \gamma_{\mu c} A_{\lambda\mu}|^2, \tag{2.64}$$

$$w(E) = \sum_c w_c(E), \tag{2.65}$$

where C^2 is a normalisation constant chosen to satisfy

$$w = \int w(E) dE = \frac{\ln 2}{t_{1/2}}. \tag{2.66}$$

The single level and single channel approximations are similar to the expressions for scattering. For a single channel:

$$w(E) = C^2 f_\beta P_c \sum_{\text{x=F,GT}} \left| \frac{\sum_\lambda g_{\lambda x} \gamma_{\lambda c}/(E_\lambda - E)}{1 - (S_c - B_c + iP_c) \sum_\lambda \gamma_{\lambda c}^2/(E_\lambda - E)} \right|^2, \tag{2.67}$$

and for a single level:

$$w(E) = C^2 f_\beta \sum_{\text{x=F,GT}} |g_{\lambda x}|^2 \frac{\sum_c P_c \gamma_{\lambda c}^2}{|E_\lambda - E - \sum_c \gamma_{\lambda c}^2 (S_c - B_c + iP_c)|^2}. \tag{2.68}$$

2.5 The R-matrix parameters

The R-matrix parameters entering the cross section and decay rate formulas are for each internal eigenstate or level, λ, the level energy, E_λ, the reduced widths, $\gamma_{\lambda c}$, for each of the channels, c, and for β decay also a β strength parameter, g_λ. For each channel the size of the internal region is determined by the channel radius, a_c, and the boundary parameter, B_c, determines the logarithmic derivative of the outgoing wave on the bounding sphere separating the internal and external regions.

To demonstrate how the R-matrix parameters are related to the physical properties of the nuclear resonances, it will now be shown how the single level approximation can be reduced to the well known Breit-Wigner formula for a narrow resonance. Since the formalism is going to be applied to β decay the single level formula for the β-decay rate will be discussed, but the derivation is similar for cross sections.

First equation 2.68 is rewritten by substituting $\Gamma_\lambda = \sum_c \Gamma_{\lambda c} = \sum_c 2P_c\gamma_{\lambda c}^2$ and $\Delta_\lambda = -\sum_c \gamma_{\lambda c}^2(S_c - B_c)$,

$$\begin{aligned} w(E) &= C^2 f_\beta \sum_{\text{x=F,GT}} |g_{\lambda x}|^2 \frac{\frac{1}{2}\Gamma_\lambda}{|E_\lambda - E + \Delta_\lambda - i\frac{1}{2}\Gamma_\lambda|^2} \\ &= C^2 f_\beta \sum_{\text{x=F,GT}} |g_{\lambda x}|^2 \frac{\frac{1}{2}\Gamma_\lambda}{(E_\lambda - E + \Delta_\lambda)^2 + \frac{1}{4}\Gamma_\lambda^2}. \end{aligned} \tag{2.69}$$

Δ_λ is energy dependent through $S_c(E)$, and can be approximated by a Taylor expansion to first order, if $S_c(E)$ is linear over the resonance energy range,

$$\Delta_\lambda(E) \approx \Delta_\lambda(E_\lambda) + (E - E_\lambda)\left.\frac{\delta\Delta_\lambda}{\delta E}\right|_{E=E_\lambda} = \Delta_\lambda(E_\lambda) + (E_\lambda - E)\sum_c \gamma_{\lambda c}^2 \left.\frac{\delta S_c}{\delta E}\right|_{E=E_\lambda}. \tag{2.70}$$

Inserting this,

$$\begin{aligned} &= C^2 f_\beta \sum_{\text{x=F,GT}} |g_{\lambda x}|^2 \frac{\frac{1}{2}\Gamma_\lambda}{\left((E_\lambda - E)(1 + \sum_c \gamma_{\lambda c}^2 \left.\frac{\delta S_c}{\delta E}\right|_{E=E_\lambda}) + \Delta_\lambda(E_\lambda)\right)^2 + \frac{1}{2}\Gamma_\lambda^2} \\ &= C^2 f_\beta \sum_{\text{x=F,GT}} |M_{\lambda x}|^2 \frac{\frac{1}{2}\Gamma_\lambda^o}{\left(E_\lambda - E + \Delta_\lambda^o\right)^2 + \frac{1}{4}(\Gamma_\lambda^o)^2}. \end{aligned} \tag{2.71}$$

If the penetration function varies slowly over the resonance, Γ_λ is approximately constant, and this is the Breit-Wigner formula for a single resonance, where the resonance energy is

$$E_r = E_\lambda + \Delta_\lambda^o = E_\lambda + \frac{\Delta_\lambda(E_\lambda)}{1 + \sum_c \gamma_{\lambda c}^2 \left.\frac{\delta S_c}{\delta E}\right|_{E=E_\lambda}} = E_\lambda - \frac{\sum_c \gamma_{\lambda c}^2 (S_c(E_\lambda) - B_c)}{1 + \sum_c \gamma_{\lambda c}^2 \left.\frac{\delta S_c}{\delta E}\right|_{E=E_\lambda}}, \tag{2.72}$$

the observed width of the state is

$$\Gamma_\lambda^o = \frac{\sum_c 2P_c\gamma_{\lambda c}^2}{1 + \sum_c \gamma_{\lambda c}^2 \left.\frac{\delta S_c}{\delta E}\right|_{E=E_\lambda}}, \tag{2.73}$$

and the β-decay matrix element is

$$M_{\lambda x} = \frac{g_{\lambda x}}{\left(1 + \sum_c \gamma_{\lambda c}^2 \left.\frac{\delta S_c}{\delta E}\right|_{E=E_\lambda}\right)^{1/2}}. \tag{2.74}$$

The penetration function is generally not a slowly varying function, so the Breit-Wigner formula is only correct for narrow resonances.

Equation 2.74 is only true for the specific normalisation constant, C^2, which fulfills,

$$f_\beta t_{1/2,\lambda} = \frac{B}{|M_{\lambda,F}|^2 + |M_{\lambda,GT}|^2}, \tag{2.75}$$

where $B = 6147(2)$ s [Hardy 2005] and this definition of $M_{\lambda,GT}$ includes the factor $|g_A/g_V| = 1.2695(29)$ [Yao 2006]. Integrating equation 2.71,

$$\frac{\ln 2}{t_{1/2,\lambda}} = C^2 f_\beta \left(|M_{\lambda,F}|^2 + |M_{\lambda,GT}|^2\right)\pi, \tag{2.76}$$

this leads to the normalisation constant,

$$C^2 = \frac{\ln 2}{\pi B} = 3.5893(12) \cdot 10^{-5}\mathrm{s}^{-1}. \tag{2.77}$$

The single-level approximation for narrow states (equation 2.71), is also valid for broad states as long as the shift function is linear over the resonance. In that case the widths, Γ_λ^o, become energy dependent functions. For both narrow and broad states the observed widths are defined by equation 2.73 with P_c evaluated at the level energy. The equivalent definition is here used for the β-decay matrix elements.

2.5.1 Boundary conditions

In R-matrix theory, the boundary condition, B_c, is a real constant which can take any value. For a single resonance, the natural choice is seen from equation 2.72 to be $B_c = S_c(E_\lambda)$, making the resonance energy, E_r, equal to the R-matrix parameter, E_λ. Typically one operates with more than one energy level and in that case the R-matrix energy can only equal the resonance energy for one of the resonances. Also the reduced width amplitudes will depend on the boundary conditions for cases with more than one resonance because the level matrix (equation 2.48) is non-diagonal. In practice one finds a set of

R-matrix parameters giving the observables for one of the resonances, λ, by choosing, $B_c = S_c(E_\lambda)$, and then transforming the parameters to a different boundary condition, $B'_c = S_c(E'_b)$ to get the observables for the other resonances [Barker 1972]. The transformation $(B_c, E_\lambda, \gamma_{\lambda c}, g_{\lambda,x}) \rightarrow (B'_c, E'_\lambda, \gamma'_{\lambda c}, g'_{\lambda,x})$ is performed by diagonalising the matrix, **C**, with entries,

$$C_{\lambda\mu} = E_\lambda \delta_{\lambda\mu} - \sum_c \gamma_{\lambda c}\gamma_{\mu c}(B'_c - B_c), \tag{2.78}$$

such that $\mathbf{D} = \mathbf{KCK}^T$, where $D_{\lambda\mu} = D_\lambda \delta_{\lambda\mu}$, and **K** is an orthogonal matrix. The transformed parameters are:

$$E'_\lambda = D_\lambda, \tag{2.79}$$

$$\gamma'_{\lambda c} = \sum_\mu K_{\lambda\mu}\gamma_{\mu c}, \tag{2.80}$$

$$g'_{\lambda x} = \sum_\mu K_{\lambda\mu} g_{\mu x}. \tag{2.81}$$

It can be shown that the transformation leaves the collision matrix invariant, which is necessary to keep the cross section or decay rate unchanged. It is an iterative process to transform the parameters from boundary conditions calculated at the resonance energy for a level, λ, to the level, μ, because the resonance energy for level μ is unknown. In each step of the iteration, instead of using $E'_b = E_\mu$ as in [Buchmann 2001], it can be an advantage to update the boundary condition energy as $E'_b = \frac{1}{2}\left(E_\mu + E_b\right)$ for easier convergence, where E_b was the boundary condition energy in the previous step.

In the alternative Kapur-Peierls framework the choice of boundary condition is a complex number, $B_c = L_c = S_c + iP_c$. This has some advantages, especially computationally because the channel and level matrices are diagonal and matrix inversion is avoided. The drawbacks are more significant though: The level parameters are not directly connected to the observed values - the level energies and reduced widths are complex numbers. Transforming the parameters back to real values to obtain the observables leads back to the difficulty of matrix inversion [Lane 1958, IX, 2].

2.5.2 Channel radius

The channel radius or interaction radius setting the size of the bounding sphere dividing the internal and external regions of configuration space is given by

$$a_c = r_0(A_1^{1/3} + A_2^{1/3}), \tag{2.82}$$

where A_1 and A_2 are the mass numbers of the two nuclei interacting through channel c. The value of r_0 can formally be arbitrarily chosen as long as it is sufficiently large to only include Coulomb interactions in the external region. The choice of channel radius affects the R-matrix parameters γ_λ and g_λ. These quantities depend linearly on the wave function, which is normalised in the internal region. The observable quantities, Γ_λ^o and $M_{x,\lambda}$, depending on the parameters squared, γ_λ^2 and g_λ^2, therefore need to be renormalised to include the tail of the wave function in the external region.

$$\Gamma_\lambda^o = \frac{\Gamma_\lambda}{1 + \int_{a_c}^{\infty} |\Psi|^2 d\tau}. \tag{2.83}$$

The integral of the wave function in the external region is approximately proportional to the derivative of the shift function on the boundary [Lane 1958, Appendix] leading to the formula for the observed width and matrix element (equations 2.73 and 2.74).

Conventionally the value of r_0 has been chosen to be the radius obtained in electron scattering experiments, typically in the range 1.40–1.50 fm (see the discussion of (1.1) in [Lane 1958]). The rms radius from electron scattering experiments is a measure of the charge distribution of the nucleus. For ^{12}C the rms charge radius is 2.4829(19) fm [Ruckstuhl 1984] corresponding to a value for r_0 of 1.4001(11) fm for a uniformly charged nucleus. The value of r_0 from rms charge radii provides at least a minimum value for the appropriate channel radius. For very loosely bound states with a smeared-out spatial distribution the assumption of a uniform nuclear distribution is far from valid in the conversion from rms charge radius to the actual radius (not rms) of the nucleus. In that case the channel radius should be chosen larger.

In practical applications of the R-matrix theory to fitting experimental data, the basis of internal states is truncated to the minimal model giving the best possible fit to the data. This can introduce an artificial dependency of

the observables from the fit on the channel radius. The truncation of the basis corresponds to neglecting the far-away levels - those levels with high energy contributing only very little to the experimental spectra at low energy. When increasing the channel radius the contribution from higher-energy states becomes larger, because their wave functions will naturally extend to larger distances, and the level parameters for the finite basis of low-energy states will change to compensate for this effect. In applications it is common to introduce so-called background levels to account for the high-energy levels which can not be constrained further (see for example [Buchmann 2001] and [Bhattacharya 2006]). For a good model the parameters for resonant states should not vary with changing channel radii, only the high-energy effective background levels will differ.

The level parameter dependencies on channel radius and boundary condition observed in some applications of R-matrix theory [Barker 1968] has led to some criticism of the phenomenological use of the R-matrix theory by advocates of the competing K-matrix [Humblet 1990]. The two parameterisations are equally valid for an infinite number of levels, but share the difficulties of truncating the basis, although the K-matrix theory does not introduce the unphysical and rather arbitrary boundary and channel radius parameters. On the other hand the K-matrix parameters are not always easy to interpret in terms of physical quantities. For example some applications require the inclusion of echo poles below threshold (see [Humblet 1998] for a comparative analysis using both K- and R-matrix).

2.5.3 Alternative form of the level matrix

An alternative set of R-matrix parameters can be found, where the energies, $\tilde{E}_i$, reduced widths, $\tilde{\gamma}_{ic}^2$ and beta strengths, $\tilde{g}_{ix}$ are the "observed" resonance parameters (equal to the standard R-matrix parameters for which $B_c = S_c(E_\lambda)$). The derivation will follow [Brune 2002] and lead to an alternative formula for the level matrix.

First, the real and symmetric matrix $\mathcal{E}$ is defined:

$$\mathcal{E} = \mathbf{e} - \sum_c \gamma_c \gamma_c^T (S_c(E) - B_c), \tag{2.84}$$

where **e** is a diagonal matrix with $e_{\lambda\mu} = E_\lambda \delta_{\lambda\mu}$, and γ_c is the column-vector with entries $\gamma_{\lambda c}$. The eigenvalue equation for $\mathcal{E}$ is

$$\mathcal{E}_i \mathbf{a}_i = \tilde{E}_i \mathbf{a}_i, \tag{2.85}$$

where $\mathcal{E}_i$ denotes the matrix $\mathcal{E}$ evaluated for the energy $\tilde{E}_i$. The dependency of $\mathcal{E}_i$ upon the eigenvalue makes this eigenvalue problem nonlinear. It is assumed that the eigenvectors are normalized so that $\mathbf{a}_i^T \mathbf{a}_i = 1$. The eigenvalues, $\tilde{E}_i$, are invariant if the boundary conditions are changed, and if $B_c = S_c(E_\lambda)$, E_λ is an eigenvalue. The eigenvalues, $\tilde{E}_i$, therefore correspond to resonance energies. The corresponding reduced width amplitudes,

$$\tilde{\gamma}_{ic} = \mathbf{a}_i^T \gamma_c, \tag{2.86}$$

are also invariant under changes in B_c, and for $B_c = S_c(E_\lambda)$, $\tilde{\gamma}_{\lambda c} = \gamma_{\lambda c}$.

The collision matrix must be invariant when changing to alternative parameters, requiring:

$$\sum_{\lambda\mu} \gamma_{\lambda c} \gamma_{\mu c'} A_{\lambda\mu} = \gamma_c^T \mathbf{A} \gamma_{c'} = \tilde{\gamma}_c^T \tilde{\mathbf{A}} \tilde{\gamma}_{c'}. \tag{2.87}$$

Using the definition, $\tilde{\gamma}_c = \mathbf{a}^T \gamma_c$,

$$\mathbf{A} = \mathbf{a} \tilde{\mathbf{A}} \mathbf{a}^T \Leftrightarrow \tilde{\mathbf{A}}^{-1} = \mathbf{a}^T \mathbf{A}^{-1} \mathbf{a}. \tag{2.88}$$

Inserting the matrix expression for $\mathbf{A}^{-1}$ this becomes,

$$\tilde{\mathbf{A}}^{-1} = \mathbf{a}^T \mathbf{e} \mathbf{a} - E \mathbf{a}^T \mathbf{a} - \sum_c \tilde{\gamma}_c \tilde{\gamma}_c^T (S_c - B_c + iP_c). \tag{2.89}$$

The matrices, $\mathbf{a}^T \mathbf{e} \mathbf{a}$ and $\mathbf{a}^T \mathbf{a}$, are derived in [Brune 2002] from equation 2.85 and 2.86 and will be denoted by **M** and **N**.

$$\mathbf{a}_j^T \mathbf{a}_i \equiv M_{ij} = \begin{cases} 1, & i = j \\ -\sum_c \tilde{\gamma}_{ic} \tilde{\gamma}_{jc} \frac{S_{ic} - S_{jc}}{\tilde{E}_i - \tilde{E}_j}, & i \neq j \end{cases}, \tag{2.90}$$

$$\mathbf{a}_j^T \mathbf{e} \mathbf{a}_i \equiv N_{ij} = \begin{cases} \tilde{E}_i + \sum_c \tilde{\gamma}_{ic}^2 (S_{ic} - B_c), & i = j \\ \sum_c \tilde{\gamma}_{ic} \tilde{\gamma}_{jc} \left(\frac{\tilde{E}_i S_{jc} - \tilde{E}_j S_{ic}}{\tilde{E}_i - \tilde{E}_j} - B_c \right), & i \neq j \end{cases}. \tag{2.91}$$

Inserting the results one obtains:

$$(\tilde{\mathbf{A}}^{-1})_{ij} = (\tilde{E}_i - E)\delta_{ij} - \sum_c \tilde{\gamma}_{ic}\tilde{\gamma}_{jc}(S_c + iP_c) \tag{2.92}$$
$$+ \sum_c \begin{cases} \tilde{\gamma}_{ic}^2 S_{ic}, & i = j \\ \tilde{\gamma}_{ic}\tilde{\gamma}_{jc}\frac{S_{ic}(E-\tilde{E}_j) - S_{jc}(E-\tilde{E}_i)}{\tilde{E}_i - \tilde{E}_j}, & i \neq j \end{cases}$$

where $S_{ic} = S_c(\tilde{E}_i)$. This level matrix can be used equivalently to the standard level matrix in calculations of cross sections and decay rates. This parameterisation is particularly useful when parameters for more than one level need to be fixed in a fit.

The alternative parameters are transformed to standard R-matrix parameters by solving the eigenvalue equation

$$\mathbf{N}\mathbf{b}_\lambda = E_\lambda \mathbf{M}\mathbf{b}_\lambda, \tag{2.93}$$

where $\mathbf{N}$ and $\mathbf{M}$ are determined by the parameters $\tilde{E}_i$, $\tilde{\gamma}_{ic}$ and B_c as given by equations 2.90 and 2.91. The standard level-energy-parameters are the eigenvalues. The reduced widths and β strengths are found as

$$\gamma_c = \mathbf{b}^T\tilde{\gamma}_c \tag{2.94}$$
$$\mathbf{g}_x = \mathbf{b}^T\tilde{\mathbf{g}}_x. \tag{2.95}$$

2.5.4 Threshold effects

For levels close to a threshold, the single-level spectrum differs significantly from the Breit-Wigner shape (equation 2.71). The rapid increase of the penetration function with energy, causes the high-energy tail of the state to increase as well, giving a second local maximum at higher energy. This effect is well known, and the anomalous peaks are often referred to as ghosts [Barker 1962]. Let us consider the β-decay rate corrected for the energy dependency in the entrance channel from f_β. This will be the inverse ft value as a function of energy. The area of the peak compared to the full energy range can be found by integration of equation 2.71 for the peak area giving

$$\int (ft)^{-1}_{\lambda,\mathrm{peak}}(E)dE = C^2 \sum_{\mathrm{x=F,GT}} |g_{\lambda x}|^2 \frac{\pi}{1 + \sum_c \gamma_{\lambda c}^2 \left.\frac{\delta S_c}{\delta E}\right|_{E=E_\lambda}} \tag{2.96}$$

and, comparing to the integral of equation 2.69 for the full state (see section A.2 in the appendix),

$$\int (ft)_\lambda^{-1}(E)dE = C^2 \sum_{x=F,GT} |g_{\lambda x}|^2 \pi. \tag{2.97}$$

Note that equation 5 in [Barker 1996] for this integral only holds for the narrow state approximation and should be replaced by equation 4 in the same reference. The peak ratio is therefore

$$\frac{A_{\text{peak}}}{A_{\text{total}}} = \frac{1}{1 + \sum_c \gamma_{\lambda c}^2 \left.\frac{\delta S_c}{\delta E}\right|_{E=E_\lambda}}, \tag{2.98}$$

and because the derivative of the shift function is always positive and decreasing with energy, the ghost effect is most significant close to the threshold.

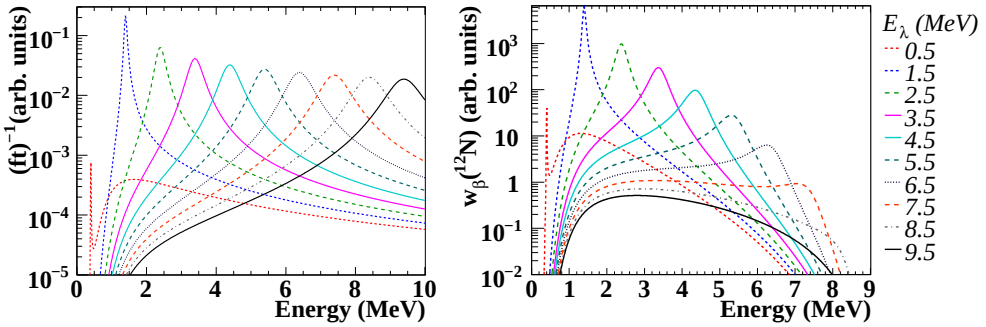

(a) Inverse ft value.

(b) β decay rate.

Figure 2.1: Levels with the same R-matrix parameters except the level energy. Inverse ft values (a) and β-decay rates (b) are shown for a 3α compund breaking up to α particles via ^{8}Be in its ground state.

Figure 2.1 illustrates how the level shape changes with varying level energy. The width of the levels close to the threshold are much smaller than for levels at higher energies and the tails of the levels are clearly altered from the Breit-Wigner shape. The examples in figure 2.1(a) show the inverse ft value, and figure 2.1(b) the β-decay rate, for decay of ^{12}N. The phase space for the β decay decreases with energy, and the contribution of the 9.5 MeV level is given only by the low-energy tail, shaped by the penetration function and phase space.

2.5.5 Interference

Another effect, which alters the level shape from the simple Breit-Wigner form, is interference. Overlapping levels with the same spin and parity can interfere constructively or destructively, so the sum of the single-level distributions differs from the distribution with interference. An example of the interference between two levels is shown in figure 2.2. The dashed curves show the Breit-Wigner distributions for two single levels and their sum. The solid line is the total distribution including the full interference. The curves in figures 2.2(a) and 2.2(b) are calculated using the standard and alternative R-matrix parameterisations respectively, and the interference spectra are seen to be identical. Due to interference, the sum of the single-level approximations is significantly different from the spectrum with interference, so it is a bad approximation to separate the contributions from interfering levels using the single-level approximation. Alternatively the contribution from an individual state, λ, can be calculated using the full R-matrix expression, but assuming that only the level λ is fed [Barker 1988b]. The β-decay rate to the level λ is then

$$w_{\lambda c}(E) = C^2 f_\beta P_c \sum_{\mathrm{x=F,GT}} |\sum_\mu g_{\lambda x}\gamma_{\mu c}A_{\lambda\mu}|^2. \tag{2.99}$$

This approximation includes part of the interference, and the dotted curves in figure 2.2 show, that the agreement with the full interference curve is much better than the single level approximation. The standard and alternative parameterisations yield different results as expected, since only the double sum, $|\sum_{\lambda\mu} g_{\lambda x}\gamma_{\mu c}A_{\lambda\mu}|^2$, is invariant, not $|\sum_\mu g_{\lambda x}\gamma_{\mu c}A_{\lambda\mu}|^2$.

Equation 2.99 can be used to calculate branching ratios to broad states as

$$\mathrm{BR}_\lambda = \frac{w_\lambda t_{1/2}}{\ln 2} = \frac{t_{1/2}}{\ln 2}\sum_c \int w_{\lambda c}(E)dE \tag{2.100}$$

under the condition that $\sum_\lambda w_\lambda \approx w$. For narrow states the branching ratio and ft value are directly related as

$$f_\beta t_{1/2,\lambda} = \frac{f_\beta t_{1/2}}{\mathrm{BR}_\lambda}, \tag{2.101}$$

and the relation to the matrix elements is given by equation 2.75. For broad states, the meaning of the ft value is not well defined, because the phase

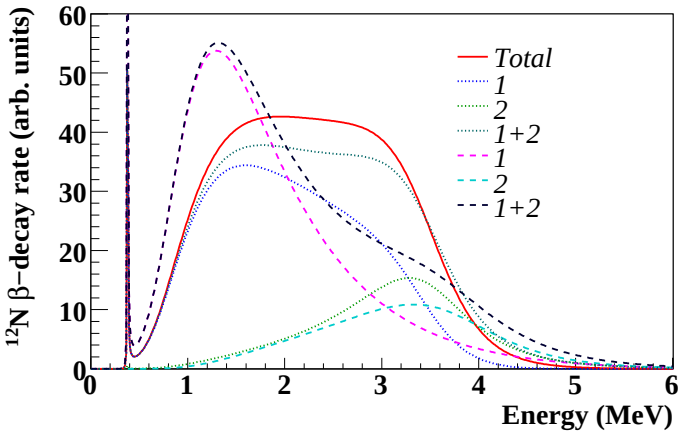

(a) Standard parametrisation.

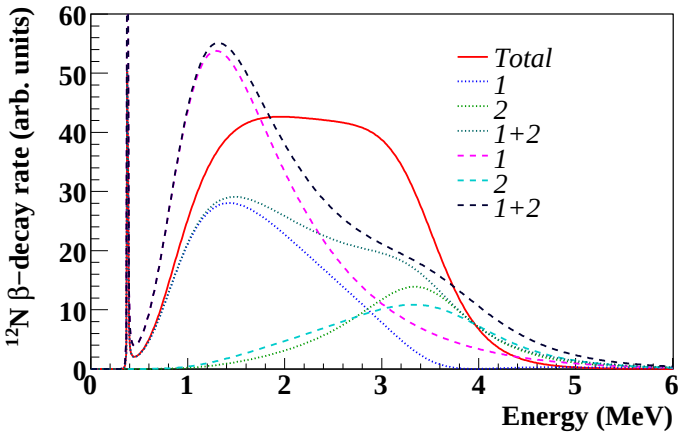

(b) Alternative parametrisation.

Figure 2.2: Interference between two 0^+ states populated in β decay of ^{12}N. The two states are only examples with level parameters put in by hand. $E_1 = 0.38$ MeV and $E_2 = 4.0$ MeV above the 3α threshold. The dashed lines are the single-level approximations, the dotted lines are the level contributions calculated using equation 2.99 and the solid line is the full interference spectrum.

space, f_β, is energy dependent. The ft value can be considered either as related to the matrix elements by equation 2.75 or to the branching ratios by integration of equation 2.101. These two definitions differ due to fact, that the definition of the matrix element used here derives from the narrow-level ap-

proximation and does not depend on the effects on the high- and low-energy tails of the level. A different definition of the matrix elements is to calculate the ft value by integration of equation 2.101 and using equation 2.75, but this would make the matrix element dependent on other levels, which seems to be in contradiction with the matrix element being the overlap between initial and final state. As an example a state close to the threshold is considered, such as level 1 in figure 2.2. This state has a significant ghost, and if the narrow-level approximation is applied, the branching ratio to the state is found to be the branching ratio to the peak only. The matrix element is therefore smaller than the value obtained by integrating the ft value over both peak and high-energy ghost and using equation 2.75. In the following, ft values will not be given to broad states to avoid misinterpretation.

2.6 Sequential decay via broad states

The formalism for reactions, scattering and β-delayed two-body breakup has now been presented, and it will be applied to the analysis of β-delayed breakup of ^{8}Be in the next chapter. In chapter 4, β-delayed breakup of ^{12}C will be analysed, and since this is a three-body process, the theory has to be extended.

Three-body decay is treated using R-matrix theory as a succession of two two-body disintegrations [Lane 1958, XIII, 2]. The initial state breaks up to a bound and an unbound component, and the treatment as a sequential decay only makes sense if the unbound part is sufficiently long lived. This also ensures that the wave function of the unbound part is sufficiently confined and a finite value can be assigned to the channel radius.

First, the standard R-matrix formula for the β-decay rate, equation 2.64, is considered. The differential rate for breakup of an initial state with energy, E, via an intermediate state with energy, E', can be written with explicit energy dependencies as

$$w_c(E,E') = C^2 f_\beta P_c(E-E') \sum_{x=F,GT} |\sum_{\lambda\mu} g_{\lambda x}\gamma_{\mu c}(E')A_{\lambda\mu}(E,E')|^2, \qquad (2.102)$$

where the inverse level matrix is

$$A^{-1}_{\lambda\mu}(E,E') = \delta_{\lambda\mu}(E_\lambda - E) - \sum_c \gamma_{\lambda c}(E')\gamma_{\mu c}(E')(S_c(E-E') - B_c + iP_c(E-E')). \tag{2.103}$$

The reduced widths have become energy dependent and, if it is assumed that the intermediate states are isolated levels, λ', the single level approximation can be used in the factorisation,

$$\gamma^2_{\lambda c}(E') = \gamma^2_{\lambda\lambda'c'}\rho_{\lambda'c'}(E') \tag{2.104}$$

$$\approx \gamma^2_{\lambda\lambda'c'}\frac{1}{2\pi}\frac{\Gamma_{\lambda'c'}(E')}{\left(E'_{\lambda'} + \Delta_{\lambda'c'}(E') - E'\right)^2 + \frac{1}{4}\Gamma_{\lambda'c'}(E')^2} \tag{2.105}$$

$$= \gamma^2_{\lambda\lambda'c'}\frac{1}{\pi}\frac{P_{c'}(E')\gamma^2_{\lambda'c'}}{\left|E'_{\lambda'} - E' - (S_{c'}(E') - B_{c'} + iP_{c'}(E'))\,\gamma^2_{\lambda'c'}\right|^2}, \tag{2.106}$$

where c' denotes the breakup channel of the intermediate state. The approximation for the reduced width can now be inserted into equation 2.102 and the energy of the unbound part, E', is contained in the terms $P_c(E-E')\rho_{\lambda'c'}(E')$ and $S_c(E-E')\rho_{\lambda'c'}(E')$. The decay rate can be obtained as the integral $\int_{\lambda'} w_c(E,E')dE'$, but this turns out to be too computationally demanding and instead it is more convenient to approximate the shift functions and penetrabilities by the weighted mean values:

$$S_c(E) = \int_{\lambda'} S_c(E-E')\rho_{\lambda'c'}dE', \tag{2.107}$$

$$P_c(E) = \int_{\lambda'} P_c(E-E')\rho_{\lambda'c'}dE'. \tag{2.108}$$

In this way the integrals only depend on the intermediate state properties, which are known for our purposes, and only have to be calculated once for each energy bin. The decay rate formula with $S_c(E)$ and $P_c(E)$ defined by the above now becomes

$$w_c(E) = C^2 f_\beta P_c(E) \sum_{x=F,GT} |\sum_{\lambda\mu} g_{\lambda x}\gamma_{\mu\lambda'c'}A_{\lambda\mu}|^2, \tag{2.109}$$

with

$$A^{-1}_{\lambda\mu} = \delta_{\lambda\mu}(E_\lambda - E) - \sum_c \gamma_{\lambda\lambda'c'}\gamma_{\mu\lambda'c'}(S_c(E) - B_c + iP_c(E)). \tag{2.110}$$

In the treatment of ^{12}N and ^{12}B β decay the formalism is going to be applied to broad as well as narrow intermediate states. An effect of this is, that the order of emission of the three identical α particles is not necessarily known, and the decay rate expression should be symmetric with respect to the order of emission. This symmetrisation is known to affect the single-alpha spectrum [Balamuth 1974, Fynbo 2003], but will here be assumed to be of less importance for the sum-energy spectrum. The good agreement between the symmetrised, sequential R-matrix calculation and the data in [Fynbo 2003], lends support to the application of R-matrix theory to sequential decay via broad intermediate states, despite the fact that this in principle makes it impossible to define a finite channel radius because the wave function of the unbound part spreads over all space.

2.7 Parameter constraints

2.7.1 The Wigner limit

The reduced width, $\gamma^2_{\lambda c}$, is, for single-nucleon excitations, constrained to be lower than the Wigner limit, γ^2_{W}, given by,

$$\gamma^2_{\mathrm{W}} = \frac{\hbar^2}{\mu_c a_c^2}, \tag{2.111}$$

where μ_c is the reduced mass and a_c the channel radius. For α-particle excitations the Wigner limit should not be taken too literally. For example the 0^+_2 state in ^{12}C has a reduced width of $\gamma^2 \sim 1.4\gamma^2_W$. The Wigner limit is however a useful guideline for identifying unphysical resonances from a fit with γ^2 several times larger than γ^2_W.

For the 2α system the Wigner limit is

$$\gamma^2_{\mathrm{W}}(2\alpha) = \frac{(197.327\ \mathrm{MeV\ fm})^2}{\frac{4\cdot4}{4+4}\cdot 931.494\ \mathrm{MeV}\cdot r_0^2(4^{1/3}+4^{1/3})^2} = 2.074\ \mathrm{MeV\ fm}^2\ r_0^{-2} \tag{2.112}$$

and for the α+^{8}Be system it is

$$\gamma^2_{\mathrm{W}}(\alpha + {}^8\mathrm{Be}) = \frac{(197.327\ \mathrm{MeV\ fm})^2}{\frac{4\cdot8}{4+8}\cdot 931.494\ \mathrm{MeV}\cdot r_0^2(4^{1/3}+8^{1/3})^2} = 1.218\ \mathrm{MeV\ fm}^2\ r_0^{-2} \tag{2.113}$$

The Wigner limit is also called the sum-rule limit, because it derives from the sum-rule,

$$\sum_{\lambda} \theta_{\lambda c}^2 \sim 1, \tag{2.114}$$

where $\theta_{\lambda c}$ are the dimensionless reduced widths,

$$\theta_{\lambda c}^2 = \left(\frac{\hbar^2}{\mu_c a_c^2} \right)^{-1} \gamma_{\lambda c}^2, \tag{2.115}$$

[Lane 1958, XII (3.13)]. The factor 3/2 in the original paper by Teichmann and Wigner [Teichmann 1952, equation (29)] is not needed in γ_W^2, even though this is still the limit quoted in many papers.

If scattering is considered as an example, the Wigner limit corresponds to the situation with no coupling between the incident particle and the nucleons inside the target nucleus. The incident particle only experiences a mean field from the scattering nucleus. In such a scattering process reactions are not possible, a compound nucleus can not be created. Instead the incident and target nuclei remain in their ground states and only single-particle excitations appear owing to the relative motion. For a mean field given by the square-well potential, the single-particle resonances all have reduced widths given by the Wigner limit. In a more realistic scenario the single-particle states are mixed with the internal excitations of the target nucleus, and the single particle reduced width is spread among the fine-structure resonances. The sum in equation 2.114 is therefore over all levels in any energy interval equal to the spacing between single particle levels. In general a reduced width close to the Wigner limit indicates cluster structure, that is, the colliding nuclei partly conserve their identity within the resonance.

2.7.2 The Gamow-Teller sum rule

The Gamow-Teller strength, or B_{GT} value, is the norm squared of the matrix element for the transition, $B_{\lambda,GT} = |M_{\lambda,GT}|^2$. The non-relativistic Gamow-Teller operators are [Osterfeld 1992, Harakeh 2001]

$$\beta_{\pm}(\mu) = \sum_{k=1}^{A} \sigma_{\mu}(k) t_{\pm}(k), \tag{2.116}$$

where σ_μ denotes the spherical components of the Pauli spin matrices ($\mu = -1, 0, 1$), $t_\pm$ are isospin raising- and lowering-operators and k runs over all nucleons of the nucleus. The isospin operations on neutron and proton states are: $t_z|n\rangle = \frac{1}{2}|n\rangle$, $t_z|p\rangle = -\frac{1}{2}|p\rangle$, $t_-|n\rangle = |p\rangle$, $t_+|p\rangle = |n\rangle$, $t_+|n\rangle = 0$ and $t_-|p\rangle = 0$. The Gamow-Teller strength function is the total GT strength summed over all final states,

$$\begin{aligned} S_\pm(GT) &= \sum_f B_{f,GT}(\beta^\pm) = \sum_{f,\mu} |\langle f|\beta_\pm(\mu)|i\rangle|^2 = \sum_{f,\mu} \langle f|\beta_\pm(\mu)|i\rangle^* \langle f|\beta_\pm(\mu)|i\rangle \\ &= \sum_\mu \langle i|\beta_\pm^\dagger(\mu)\beta_\pm(\mu)|i\rangle. \end{aligned} \tag{2.117}$$

Using $\beta_\pm^\dagger = \beta_\mp$, the difference of the strength functions is (omitting the μ dependencies for readability)

$$\begin{aligned} S_-(GT) - S_+(GT) &= \langle i| \sum_\mu (\beta_-^\dagger \beta_- - \beta_+^\dagger \beta_+)|i\rangle \\ &= \langle i| \sum_\mu (\beta_+ \beta_- - \beta_- \beta_+)|i\rangle. \end{aligned} \tag{2.118}$$

Applying the commutator relation

$$[\beta_+(\mu), \beta_-(\mu)] = 2T_z, \qquad \mu = -1, 0, 1 \tag{2.119}$$

where $T_z = \sum_{k=1}^{A} t_z$, we obtain the so-called Ikeda sum rule [Ikeda 1963],

$$S_-(GT) - S_+(GT) = 3(N - Z). \tag{2.120}$$

The sum rule applies to the β^+ and β^- strengths of a parent nucleus. For example ^{12}N has $Z = 7$ and $N = 5$ giving

$$S_+(GT) = S_-(GT) + 3(Z - N) = S_-(GT) + 6. \tag{2.121}$$

This puts a lower limit on the β^+ strength function, $S_+(GT) > 6$. In the analysis, using R-matrix formalism to fit β-decay spectra, it is more relevant to know the upper limit on the beta strength, and typically $S_+(GT) \gg S_-(GT)$ so equation 2.121 becomes $S_+(GT) = 6$. A very conservative estimate would be a factor of two: $S_-(GT) < \frac{1}{2}S_+(GT)$, constraining $S_+(GT)$ between 6 and 12.

2.8 Other applications of R-matrix formalism

Originally R-matrix theory was developed in nuclear physics as a phenomenological parametrisation of nuclear scattering data. During the last half century since the publication of the standard R-matrix reference by Lane and Thomas [Lane 1958] its range of applications has increased to encompass also atomic and molecular physics [Allison 1972, Berrington 1974, Chang 1975, Berrington 1995, Aymar 1996]. In this context, R-matrix theory is used as a method for solving the Scrödinger equation rather than as a parametrisation of experimental data and exists in different variants as for example the eigenchannel and Wigner-Eisenbud R-matrix methods [Aymar 1996]. This use of the R-matrix theory also has applications in nuclear physics where it is denoted the calculable R-matrix by Descouvemont and Baye [Descouvemont 2010b].

As in the standard or phenomenological use of the R-matrix method the interaction region is separated in an internal and an external region when trying to solve a given Schrödinger equation. The wave function in the internal region is expanded in a finite basis and the solution is matched to the wave function in the external region which is approximated by the exact asymptotic expression, equation 2.5. A toy example is shown in figure 2.3 taken from [Descouvemont 2010b] showing the wave function for the ^{12}C+p system at 2 MeV with a channel radius of 8 fm and 15 basis functions. The matching of the wave functions at the channel radius is seen to be poor for a basis of sine functions and following the exact solution for Lagrange functions.

Calculations within the R-matrix framework have been applied to three-body continuum states such as ^{6}He ($\alpha + 2n$) and ^{12}C (3α) [Thompson 2000, Descouvemont 2006, Descouvemont 2010b, Descouvemont 2010a]. These systems are treated using the hyperspherical formalism, where the radial coordinate for two-body systems is replaced by the hyperradius, ρ. For the three-α system, $\rho = \sum_{i=1}^{3} 4r_i^2$, where r_i is the center-of-mass coordinate of the i'th α particle. The channel radius in hyperspherical coordinates will therefore naturally be larger than in typical applications with radial coordinates. The potentials are also slowly decreasing as ρ^{-3} and this leads to very large channel radii of typically 200–300 fm for obtaining convergence. Such a large channel radius requires a very large basis, and to avoid this, a solution for a lower chan-

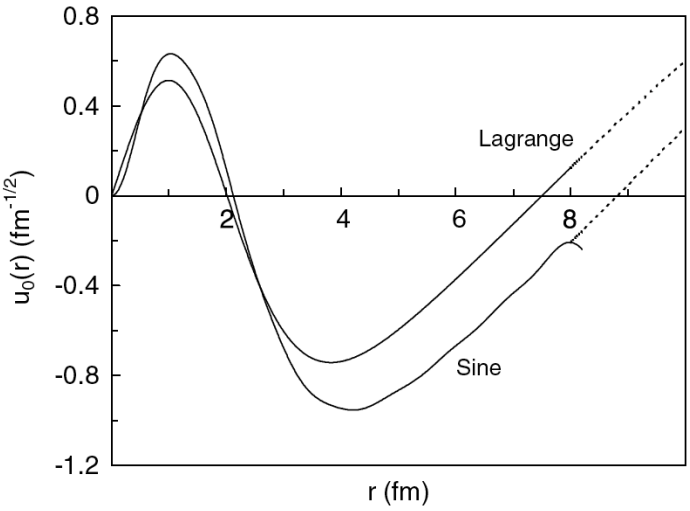

Figure 2.3: *R*-matrix calculations of the ^{12}C+p system using Lagrange and sine basis functions respectively [Descouvemont 2010b].

nel radius is found ($a_c \sim 30 - 40$ fm) and propagated to the larger channel radius for which the wave functions have reached their proper assymptotic behaviour [Light 1976, Baluja 1982, Burke 1995].

CHAPTER 3

Beta decay of ^{8}B

In this chapter, results from a complete kinematics measurement of ^{8}B β decay will be presented. The experiment was performed in 2008 at the Jyväskylä Accelerator Laboratory, Finland. The raw data has been analysed by O. S. Kirsebom to obtain the 2α sum-energy spectra analysed within the R-matrix framework in section 3.4. The preliminary analysis of the implications for an updated ^{8}B neutrino spectrum will be presented in section 3.8.

3.1 Motivation

3.1.1 0^+ and 2^+ intruder states in ^{8}Be

The ^{8}Be nucleus is one of the most well studied of all isotopes. Despite this, controversy remains concerning the proposed existence of broad 0^+ and 2^+ states in ^{8}Be around 6 and 9 MeV respectively. These states were first proposed in 1968 and 1969 by Barker [Barker 1968, Barker 1969] who performed simultaneous fits to scattering, reaction and decay data probing the ^{8}Be nucleus. Barker argued, that to give a consistent description of all types of measurements feeding the same nucleus, the (R-matrix) parameters of the fit model should only differ in the feeding parameters (see also [Barker 1988a]). If only data from one type of measurement were considered, the results depended on the choice of channel radius with reasonable fits for a range of radii. Simultaneously fitting different data sets constrained the channel radius to the optimum value and also constrained the energy and width parameters. Barker also argued that similar excited 0^+ states exist in other light even nuclei (see table 2 in [Barker 1988a]) with energies of about 6–8 MeV and large reduced widths. These states can be interpreted as intruder states within the shell model - states belonging to a higher shell configuration. That such states exist in neighbouring even nuclei makes it probable that similar states could

exist in ^{8}Be with the same properties. One of the examples of neighbour nuclei with intruder states is ^{12}C with its 0^+_1 excitation (the Hoyle state). The 0^+ state found by Barker [Barker 1968] has the same dimensionless reduced width, $\theta = 1.4$, as the Hoyle state in ^{12}C, although their respective observed widths are 10 MeV compared to 7.65 eV. This is a good example of the threshold effect (see figure 2.1).

Several critics have over the years disputed Barker's results [Warburton 1986, Fayache 1998, Humblet 1998, Bhattacharya 2002, Bhattacharya 2006]. One of the major difficulties with the interpretation is that the broad resonances are overlapping and unresolved. None of the proposed intruder states are seen as peaks in the data spectra. Another point of criticism is the size of the channel radius obtained by Barker. Warburton [Warburton 1986] states that the natural choice is $r_0 = 1.4$ fm from electron scattering giving $a_c = 4.5$ fm. However, as Barker replies in [Barker 1988a], the rms charge-radius measured with electron scattering does not directly correspond to the R-matrix channel radius as discussed in chapter 2.

Low-energy 0^+ and 2^+ intruder states have not been found theoretically in shell-model calculations for ^{8}Be [Navrátil 1998, Fayache 1998]. In the work by Fayache *et al.*, no low-lying intruder states were found in ^{8}Be, while for the neighbour nuclei, ^{10}Be and ^{12}C, they found the known 0^+ intruder states close to their experimental energies, 6.111 MeV and 7.654 MeV. Fayache *et al.* claimed that this disproved Barker's argument that similar intruder states were likely to be found in ^{8}Be. However these results differ from more sophisticated shell-model calculations, which do not find any intruder states in either ^{8}Be, ^{10}Be or ^{12}C [Navrátil 1998, Navrátil 2000, Navrátil 2003]. Such spatially extended states are very difficult to accommodate in the finite harmonic-oscillator model space and are characterised by slow convergence. In consequence it is difficult to get the correct, low enough energies of these states [Hyldegaard 2010]. Excited states in the ^{8}Be nucleus have also been calculated with the Green's function Monte Carlo approach, and this reproduces the known 2^+ states around 3, 16 and 20 MeV, but no state is seen between 3 and 16 MeV [Pieper 2004].

Barker's 2^+ intruder state is supported by a combined fit to data for 11 different reactions leading to the ^{8}Be intermediate state [Page 2005]. Here the 2^+

state was found at 16.4 MeV with a 19.2 MeV width. The channel radii were chosen rather arbitrarily based in earlier R-matrix analyses ranging from 3 fm to 6.5 fm. In other works no need was found for intruder states [Warburton 1986, Bhattacharya 2006], but here fits were performed separately to $\alpha - \alpha$ scattering and β-decay data and, as will be discussed in section 3.4.1, the 16 MeV doublet was not treated correctly.

The β-delayed 2α breakup of ^{8}Be will be analysed here within the R-matrix formalism to test the different models of the 2α continuum supported by Barker [Barker 1969, Barker 1989] and Warburton [Warburton 1986, Bhattacharya 2006].

3.1.2 Solar neutrinos

The ^{8}B β decay, $^8\mathrm{B} \rightarrow ^8\mathrm{Be} + e^+ + \nu_e$, takes place in the Sun as one step in the hydrogen-burning processes. For a long time, the measured flux of neutrinos from the Sun was found to be too small compared to predictions by the solar models, and this became known as “the solar neutrino problem". It requires very large underground detectors to detect the very weakly interacting neutrinos emitted from the Sun. Davis performed the first of such measurements using the ^{37}Cl(ν,e)^{37}Ar reaction in a tank filled with 470 tons of C_2Cl_4 within a cavity in the Homestake mine. The neutrino flux was extracted by counting the number of argon atoms in the tank and less than half of the expected number predicted by the standard solar model was detected [Davis 1968]. This led to a series of experiments measuring solar neutrinos, and it was not until the beginning of this century, when the SNO collaboration performed an experiment sensitive to other neutrino flavours than the electron neutrino, that the problem was finally solved [Ahmad 2001]. It is now known that neutrinos have mass, and due to flavour oscillations, an electron neutrino created in the Sun has a probability of being detected as a muon or tau neutrino on Earth.

The large water and heavy-water Cerenkov detectors, Super-Kamiokande [Fukuda 2001] and SNO, are sensitive to the high-energy end of the neutrino spectrum and this is the part dominated by ^{8}B neutrinos. The Homestake experiment and gallium experiments such as SAGE [Abdurashitov 2002] and GALLEX [Hampel 1999] were sensitive to lower energies as well, but these experiments did not measure the neutrino energy. For precise calculations of

the solar-neutrino spectrum, the ^{8}B neutrino spectrum has to be measured in the laboratory. This is done indirectly by measuring the positron from the β decay or the α particles from the β-delayed breakup of ^{8}Be and determining the missing energy escaped with the neutrino. In the neutrino spectrum compilation from 1996 Bahcall finds disagreement between the peak energy in the single-alpha spectra existing in the literature at the time of ±80 keV [Bahcall 1996]. The standard neutrino spectrum was therefore inferred from the only measurement of the positron spectrum [Napolitano 1987]. A newer 2α coincidence measurement by Ortiz *et al.* [Ortiz 2000] provides a more accurate neutrino spectrum but is in disagreement with the sum spectrum from an implantation experiment by Winter *et al.* [Winter 2006]. New single-alpha measurements by Bhattacharya *et al.* [Bhattacharya 2006] agree with the results in [Winter 2006]. The measured energy spectra from Super-Kamiokande reported in [Hosaka 2006] and [Cravens 2008] are compared to predictions based on the neutrino spectra reported by Ortiz *et al.* This is also the case for the SNO results in [Aharmim 2005], but newer publications use the neutrino spectra by Winter *et al.* for comparison [Aharmim 2008]. The measured solar neutrino spectrum shape is distorted due to the energy dependence of the flavour survival probability. Improving the accuracy of the neutrino spectrum, especially at high energy, will improve the determination of the precise distortion and ultimately constrain the neutrino models.

3.2 2α coincidence experiment

The β decay of ^{8}B provides a clean probe of 2^+ states in ^{8}Be. The decay scheme for the ^{8}B β decay is shown in figure 3.1. ^{8}B has spin and parity 2^+ so, according to the Fermi and Gamow-Teller selection rules, only 1^+, 2^+ and 3^+ states can be populated. The known states in ^{8}Be below the β^+ Q-value are the 0^+ ground state, which is unbound by 91.8 keV, the broad 2^+ first excited state at 3 MeV, a very broad (Γ^o = 3.5 MeV) 4^+ state at 11.4 MeV and the isospin doublet of 2^+ states at 16.6–16.9 MeV. β-decay to the 0^+ and 4^+ states is second forbidden so only the 2^+ states in figure 3.1 are known to be populated. Since only 2^+ states are populated the analysis of the spectrum is simplified to a single channel and the system serves as a relatively simple starting point for

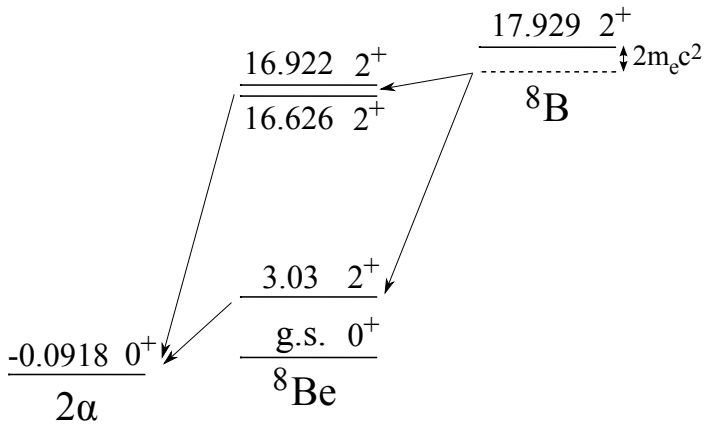

Figure 3.1: Decay scheme for β decay of ^{8}B to known levels in ^{8}Be [Tilley 2004]. Energies are in MeV.

the application of *R*-matrix theory.

3.2.1 Experimental method

The experiment was performed in January 2008 at the IGISOL facility of the Jyväskylä Accelerator Laboratory (JYFL), Finland. ^{8}B was produced and separated using the IGISOL method. IGISOL is an abbreviation for Ion Guide Separator On-Line and is a variant of the ISOL (Isotope Separator On-Line) technique for separation of radioactive nuclei [Äystö 2001]. The ^{8}B nuclei were produced with a ^{6}Li(^{3}He,n)^{8}B reaction using a 0.5 μA, 15 MeV ^{3}He beam impinging on a foil of 1.95 mg/cm^2 LiF on a 3.2 mg/cm^2 Al backing. The use of thin target foils allows the produced ions to leave the target after which they are thermalised in a helium buffer gas, accelerated to 20 keV and mass separated before reaching the detector setup.

The detector setup is shown in figure 3.2. The ^{8}B nuclei were stopped in a 25 μg/cm^2 carbon foil. In the foil, the nuclei would β decay and subsequently breakup to two α-particles. Surrounding the foil were placed four double sided silicon strip detectors (DSSSDs) for α-particle detection. The detectors were rotated 45° with respect to the beam direction as shown in figure 3.2. Each DSSSD was a 60 μm thick 50 mm $\times$ 50 mm silicon wafer with 16 front strips orthogonal to the 16 back strips. The strips were each 3.0 mm wide,

separated by 0.1 mm. The inactive doped layer on the front side of the detector results in a dead layer equivalent to 100 nm of silicon for all the DSSSDs. The most energetic α particles ($\sim$ 8.5 MeV) hitting a DSSSD are fully stopped in the detector. The configuration of the DSSSDs seen in figure 3.2 provides a large solid angle coverage of $\sim$ 30% of 4π with an angular resolution of $\sim$ 3 degrees. A 1.5 mm thick, unsegmented silicon detector is placed behind each DSSSD for the detection of β particles.

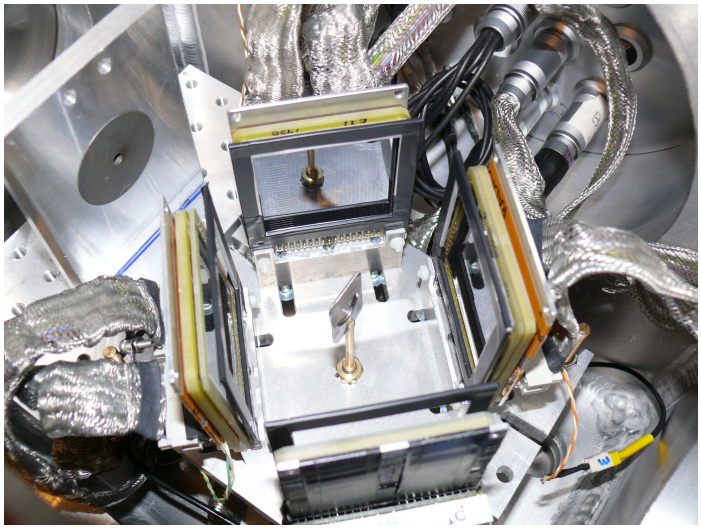

Figure 3.2: Experimental setup. The beam comes in from the upper left through the 5 mm collimator. Clockwise from the top the DSSSDs are numbered as 1, 3, 4 and 2.

The energy calibration was performed using α lines for ^{20}Na, taking into account the effect of non-ionising stopping in the detector. The ^{20}Na lines were also used to extract the detector response distribution as a function of energy for each detector. The resolution of the detectors was better at the beginning of the experiment with a best resolution of $\sigma \approx 14$ keV but deteriorating somewhat during the course of the experiment.

The spectra have been corrected for the energy loss in the carbon foil and detector dead-layers and the 2α coincidences have also been corrected for the geometric detection efficiency. Due to lepton recoil the two α particles are not emitted exactly back-to-back, and this complicates the determination of the coincidence efficiency. For this reason one must consider coincidences in a pair of opposite detectors, including only the central 6×6 pixels in one of the

two detectors. In the analysis presented here, only coincidences between one detector pair is considered (DSSSDs 1 and 4). The details of the energy and efficiency calibrations are given elsewhere [Kirsebom 2010a].

3.3 Data

The coincident measurement of the two individual α particles in the breakup of ^{8}Be makes it possible to obtain ^{8}Be excitation energy spectra directly from the 2α sum spectrum. At the same time the single α-energy spectra provides a comparison to other single-α measurements and serves as a consistency check of the 2α spectrum.

The measured coincidence spectrum is shown in figure 3.3, plotted as the inverse ft value divided by the penetration function for the 2α break-up channel. The resulting spectrum is then essentially the resonant structure of ^{8}Be where the entrance channel and the energy dependency in the exit-channel have been removed. The features seen in the spectrum are the 3 MeV peak, the 16 MeV doublet and a large energy region in between with signs of constructive interference between the two states. One would expect the 3 MeV state and the doublet to contribute significantly to the spectrum, but probably something more is needed to describe much of the strength in between.

3.4 R-matrix analysis

The ^{8}B β-decay probability is given by the many-level, single-channel expression (equation 2.67), where the single channel is 2α breakup with angular momentum $L = 2$. The measured 2α sum-energy spectrum, $N(E)$, is related to the decay probability as $N(E) = (Nt_{1/2}/\ln 2)w(E)$, where $t_{1/2} = 770(3)$ ms is the lifetime of ^{8}B and N is the total number of β decays. The fit function within the standard R-matrix formalism is therefore,

$$N(E) = \frac{Nt_{1/2}}{\pi B} f_\beta(Q-E) P_c(E) \frac{\left|\sum_\lambda \frac{g_{\lambda,F}\gamma_{\lambda c}}{E_\lambda - E}\right|^2 + \left|\sum_\lambda \frac{g_{\lambda,GT}\gamma_{\lambda c}}{E_\lambda - E}\right|^2}{\left|1 - [S_c(E) - B_c + iP_c(E)] \sum_\lambda \frac{\gamma_{\lambda c}^2}{E_\lambda - E}\right|^2}. \tag{3.1}$$

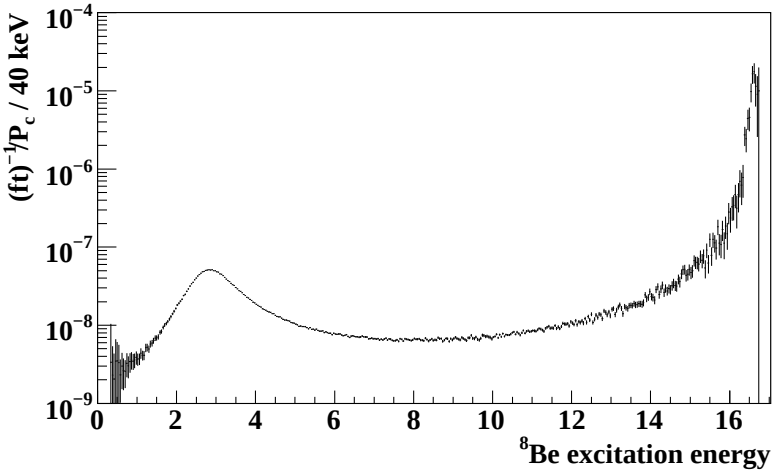

Figure 3.3: The ^{8}B β-decay spectrum corrected for the β-decay phase space and penetration function for the 2α channel.

In this work, the alternative parametrisation has been used giving,

$$N(E) = \frac{Nt_{1/2}}{\pi B} f_\beta(Q-E) P_c(E) \left\{ \left| \sum_{ij} \tilde{g}_{iF} \tilde{\gamma}_{jc} \tilde{A}_{ij} \right|^2 + \left| \sum_{ij} \tilde{g}_{iGT} \tilde{\gamma}_{jc} \tilde{A}_{ij} \right|^2 \right\}, \tag{3.2}$$

which is a slightly more complicated expression than equation 3.1, but provides the observables directly from the fit.

3.4.1 The 16.6–16.9 MeV isospin doublet

The treatment of the isospin doublet will be explained in this section, following Barker's approach in [Barker 1969] and [Barker 1989]. The 2^+ doublet peaks at 16.626 MeV and 16.922 MeV can be described by the splitting of two isospin-mixed states, $|\, a\rangle$ and $|\, b\rangle$. These states are linear combinations of the $T = 1$ isospin analogue of the ^{8}Li and ^{8}B ground states and a $T = 0$ component [Barker 1966, Barker 1975]:

$$|\, a\rangle = \alpha \,|\, T = 0\rangle + \beta \,|\, T = 1\rangle, \tag{3.3}$$

$$|\, b\rangle = \beta \,|\, T = 0\rangle - \alpha \,|\, T = 1\rangle, \tag{3.4}$$

with $\alpha^2 + \beta^2 = 1$. The states $|\ \lambda\rangle$ ($\lambda = a, b$) can be identified as the R-matrix internal eigenfunctions X_λ. Omitting the subscript c in the following, the $\gamma_{\lambda c}$ are linear in $|\ \lambda\rangle$ (equation 2.19) giving

$$\gamma_a = \alpha\gamma_0 + \beta\gamma_1, \tag{3.5}$$

$$\gamma_b = \beta\gamma_0 - \alpha\gamma_1. \tag{3.6}$$

The observed widths are $T = 0$ widths because $\Delta T = 1$ α-decay is forbidden, so the total decay width is $\Gamma_0 = \Gamma_a + \Gamma_b$. The states are high above the α-decay threshold so the denominator in equation 2.73 for the observed width can be set equal to 1, and the penetration function is to a good approximation constant over the doublet, leading to the following reduced widths:

$$\gamma_a^2 = \alpha^2 \frac{\Gamma_0}{2\bar{P}} = \alpha^2 \frac{\Gamma_a + \Gamma_b}{2\bar{P}}, \tag{3.7}$$

$$\gamma_b^2 = \beta^2 \frac{\Gamma_0}{2\bar{P}} = \beta^2 \frac{\Gamma_a + \Gamma_b}{2\bar{P}}, \tag{3.8}$$

where $\bar{P}$ is the mean penetrability over the doublet. α and β are found as

$$\alpha^2 = \Gamma_a/\Gamma_0 = \Gamma_a/(\Gamma_a + \Gamma_b), \tag{3.9}$$

$$\beta^2 = \Gamma_b/\Gamma_0 = \Gamma_b/(\Gamma_a + \Gamma_b). \tag{3.10}$$

The matrix elements $M_{a,x}$ and $M_{b,x}$ are

$$M_{a,x} = \langle a \mid O_x \mid i\rangle = \alpha M_{0,x} + \beta M_{1,x}, \tag{3.11}$$

$$M_{b,x} = \langle b \mid O_x \mid i\rangle = \beta M_{0,x} - \alpha M_{1,x}. \tag{3.12}$$

For Fermi decay $M_{0,\mathrm{F}} = 0$ and $M_{1,\mathrm{F}}^2 = T(T+1) - T_3(T_3+1) = 2$, so

$$M_{a,\mathrm{F}} = \sqrt{2}\beta, \qquad M_{a,\mathrm{GT}} = \alpha M_{0,\mathrm{GT}} + \beta M_{1,\mathrm{GT}}, \tag{3.13}$$

$$M_{b,\mathrm{F}} = -\sqrt{2}\alpha, \qquad M_{b,\mathrm{GT}} = \beta M_{0,\mathrm{GT}} - \alpha M_{1,\mathrm{GT}}. \tag{3.14}$$

The $T = 1$ Gamow-Teller matrix element, $M_{1,\mathrm{GT}}$, is predicted in shell-model calculations to be very small compared to $M_{0,\mathrm{GT}}$ [Warburton 1986], so it is set equal to zero.

R-matrix widths and energies for the doublet states were determined by Hinterberger *et al.* [Hinterberger 1978] using elastic scattering of α particles from ^{4}He. In their analysis the 16 MeV region was analysed with R-matrix

formalism in the single-channel, two-level approximation, without including the effect of other 2^+ states in ^{8}Be. These levels will introduce a third term in the sum in the denominator of equation 3.1, which to a good approximation can be considered constant over the energy range of the doublet.

$$\sum_\lambda \frac{\gamma_\lambda^2}{E_\lambda - E} = \frac{\gamma_a^2}{E_a - E} + \frac{\gamma_b^2}{E_b - E} + \sum_{\lambda,\text{rest}} \frac{\gamma_\lambda^2}{E_\lambda - E} \tag{3.15}$$
$$\approx \frac{\gamma_a^2}{E_a - E} + \frac{\gamma_b^2}{E_b - E} + K.$$

The relations between energies and widths with $K = 0$ and $K \neq 0$ are provided in [Barker 1969], with superscript zero indicating parameters for $K = 0$:

$$E_{a,b} = \frac{1}{2}\left\{E_a^0 + E_b^0 - \frac{1}{2}K'(\Gamma_a^0 + \Gamma_b^0)\right. \tag{3.16}$$
$$\left. \pm \left[\left(E_a^0 - E_b^0 - \frac{1}{2}K'(\Gamma_a^0 - \Gamma_b^0)\right)^2 + K'^2\Gamma_a^0\Gamma_b^0\right]^{1/2}\right\},$$

$$\Gamma_a = (1 + (K')^2)\frac{\Gamma_a^0(E_b^0 - E_a) + \Gamma_b^0(E_a^0 - E_a)}{E_b - E_a}, \tag{3.17}$$

$$\Gamma_b = (1 + (K')^2)\frac{\Gamma_a^0(E_b - E_b^0) + \Gamma_b^0(E_b - E_a^0)}{E_b - E_a}, \tag{3.18}$$

where $K' = K/\bar{P}$. The energies and widths from [Hinterberger 1978] are: $E_a^0 = 16.715(3)$ MeV, $\Gamma_a^0 = 0.1077(5)$ MeV, $E_b^0 = 17.017(3)$ MeV and $\Gamma_b^0 = 0.0744(4)$ MeV (R-matrix energies relative to the alpha threshold). Following Barker [Barker 1989], K and $\bar{P}$ are evaluated in the weighted mean energy

$$E_M = \frac{\Gamma_a^0 E_a^0 + \Gamma_b^0 E_b^0}{\Gamma_a^0 + \Gamma_b^0} = 16.838\text{MeV}. \tag{3.19}$$

The alternative R-matrix parametrisation (equation 3.2) has been used in a fit to the data to obtain observables directly as fit parameters and, equally important, to allow for fixing both the doublet and other level energies. To calculate the value of K used for finding the correct doublet R-matrix parameters it is necessary to transform the parameters to standard R-matrix parameters with boundary condition at the doublet energy (see section 2.5.3). The parameters for the doublet levels are approximated to their previous values when doing the transformation, but are updated using Eqs. 3.16, 3.17 and 3.18 after calculating K. This procedure is repeated until K has sufficiently converged.

3.4.2 Analysis

The minimisation tool used in both this analysis and that described in section 4.6 is the Minuit2 package [Minuit2 2010] implemented within the ROOT framework [ROOT 2010]. The function to minimise is a log-likelihood function

$$\chi^2 = 2\sum_i \left(n_{i,fit} - n_{i,data} + n_{i,data} \ln\left(\frac{n_{i,data}}{n_{i,fit}}\right)\right). \tag{3.20}$$

The detected α energy is given by an asymmetric response function, which broadens the energy distribution and shifts it to lower energy. To take this into account the calculated spectrum is folded by the normalised response function before comparing to the measured spectrum. The fits were restricted to the range from 1.5 MeV to 17 MeV excitation energy, because of the uncertainty in the efficiency calibration at lower energy.

The number of free parameters in the fit depends on the number of levels included. Each level is defined by a level energy, E_λ, a β strength, g_λ, and a reduced width, γ_λ , for the $L = 2$ channel. For the isospin doublet only the β stength is varied.

The analysis proceeds by fitting the data to increasingly more complex models of the 2α continuum. It has been well known since the 1960's that a model representing only the first excited 2^+ state at 3 MeV fails in describing the data above 5 MeV where the transition probability is much too high to be explained by this state alone [Griffy 1960, Alburger 1963]. This is as expected judging from figure 3.3. In Table 3.1 the 5 different models considered in this analysis are listed. Each of these will be discussed here.

- *The 3 MeV state and the 16 MeV isospin doublet.*

  The first model to consider will be one including the 3 MeV state and the isospin doublet. A fit to this model is shown in Fig. 3.4, from which it is seen that the main components of the spectrum can be explained by these known states, although the residuals show that there are regions where this model does not fit so well. For example the 3 MeV peak becomes too broad in the fit as seen from the residuals in the peak region, to compensate for the missing strength above the peak. The width of the 3 MeV state is 2 MeV in this fit, 3.4 times the Wigner limit (equation

Model	χ^2/df	r_0 (fm)	a_c (fm)	Figure
1: 3 MeV + doublet	1.47	1.14	3.61	3.4
2: Model 1 + 37 MeV	0.97	1.35	4.28	3.5
3: Model 1 + $E_\lambda >$ doublet	0.97	1.5	4.8	3.6
4: Model 1 + $E_\lambda <$ doublet	0.98	2.1	6.7	3.7
5: Model 4 + 45 MeV($g_\lambda = 0$)	0.97	2.0	6.4	3.8

Table 3.1: The applied *R*-matrix models (Different combinations of 2^+ states) and their reduced χ^2 values. The number of degrees of freedom is 775 minus the number of free parameters (see text).

2.112). The poor fit quality is evident from the reduced χ^2 value of 1.47, where the number of degrees of freedom is the number of energy bins (775) minus the number of free parameters, which is 3 for the 3 MeV state (E_1, g_1, γ_1) and 1 for the doublet (g_{2+3}) plus the channel radius, which was optimised to $r_0 = 1.14$ fm (see Table 3.1).

- *An additional level fixed at 37 MeV.*

  Fits were performed in [Warburton 1986], [Winter 2006] and [Bhattacharya 2006] to a model including the 3 MeV state, the isospin doublet and a high-energy level which was fixed at 37 MeV. Their approach is slightly flawed in its treatment of the isospin doublet, as discussed by Barker in [Barker 1989], because Hinterberger's *R*-matrix parameters for the doublet [Hinterberger 1978] have not been corrected to allow for interference with other 2^+ states (see Section 3.4.1). In the fits presented here, the doublet parameters have been corrected following Barker's approach.

  If the channel radius is varied a best fit is found for $r_0 = 1.35$ fm with χ^2/df = 0.97 and this is the fit shown in figure 3.5. The 37 MeV level obtains a very large width: $\Gamma^o \approx 130$ MeV, 7.5 times the Wigner limit, indicating that it is not a physical level. The fit parameters for this model are given in the first column of table 3.2.

- *Variable energy level above the isospin doublet.*

  An adequate fit was already obtained for an energy level fixed at 37

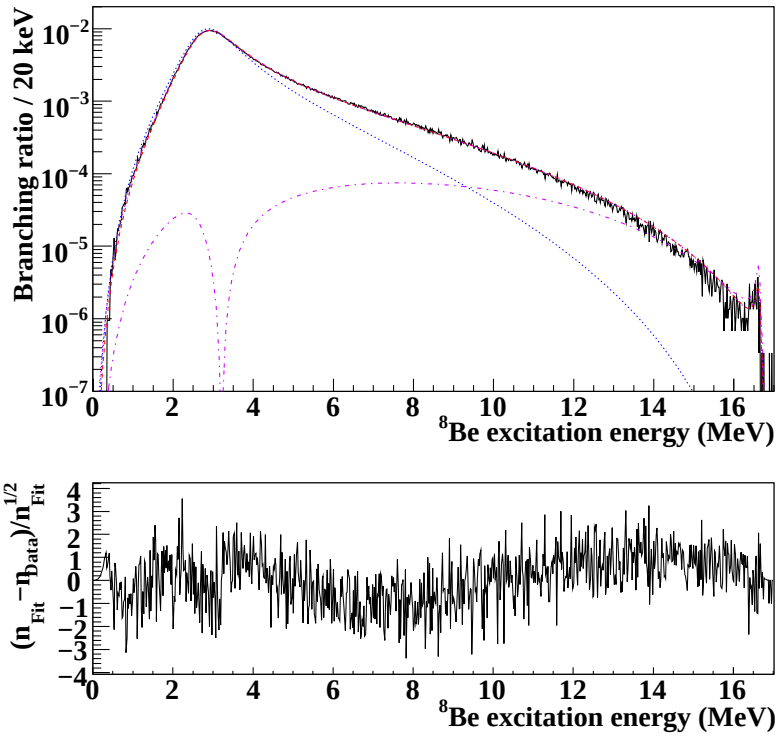

Figure 3.4: Fit to Model 1 in Table 3.1. The solid line is the data spectrum, the dashed line is the fit and the dotted and dot-dashed lines are fit components for the 3 MeV state and 16 MeV doublet respectively. Below, the fit residuals are shown.

MeV, but to explore the parameter space further, the high energy level is now allowed to have a variable energy. The best fit is found for a level energy of 22.7(6) MeV with $\chi^2/\mathrm{df} = 0.97$. The fit quality is unchanged compared to a fixed level energy at 37 MeV, in agreement with Warburton's statement that the fit is insensitive to the energy of this level [Warburton 1986]. Changing the channel radius between 1.35 and 1.6 fm does not affect the fit quality either. It affects the parameter values however - when the channel radius is increased the energy of the high-energy level decreases. Fits for $r_0 = 1.4$ and 1.5 fm are given in the second and third column of table 3.2.

- *Variable energy level below the isospin doublet.*

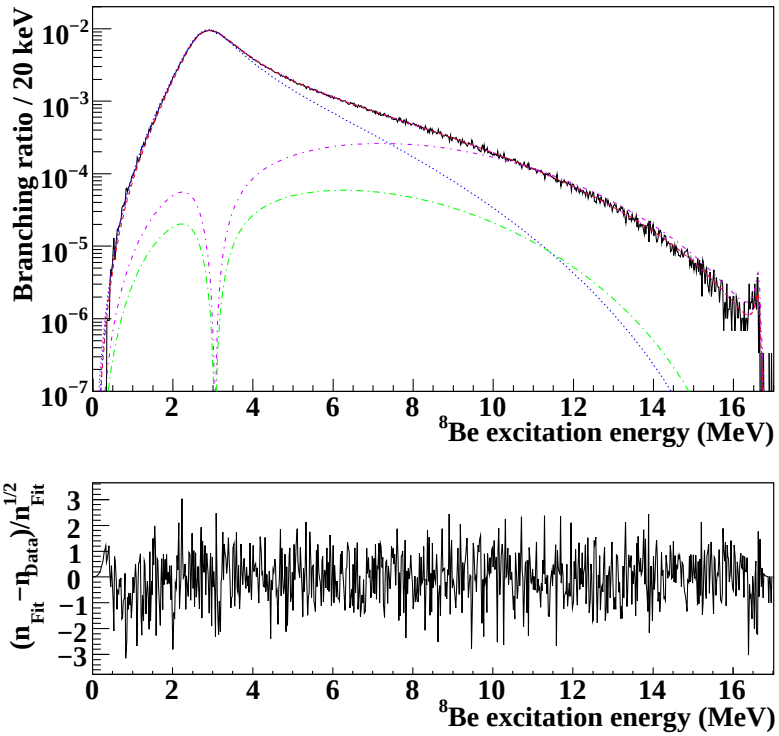

Figure 3.5: Fit to Model 2 in Table 3.1. An extra component corresponding to the 37 MeV level is added compared to the model in figure 3.4.

If the channel radius is further increased a good fit can be obtained with a level below the isospin doublet. The interference with the 3 MeV state and the doublet now has opposite sign. The fit quality of this model does not change significantly from $r_0 = 2.0$ fm to 2.4 fm. The level energy is in the range 13.5–15 MeV and the width of the order 20 MeV. The parameterisation for $r_0 = 2.0$ fm is given in the last column of table 3.2.

- *Model 4 plus a broad 45 MeV level with zero beta strength.*

  The model used in Barker's *R*-matrix fits [Barker 1989] includes the 3 MeV state, the isospin doublet and a level between the two, as in our Model 4, but with an additional high-energy background level with zero Gamow-Teller strength, well above the fitted energy region. The energy used for the background level is not given in [Barker 1989], and in fact it

Parameter		Model 2	Model 3	Model 3	Model 4
r_0 (fm)		1.35	1.4	1.5	2.0
2^+_1	E (MeV)	3.054(5)	3.0306(15)	2.985(2)	2.787(2)
	θ	1.043(18)	1.0224(13)	1.004(2)	1.1264(8)
	Γ^o (MeV)	1.47(2)	1.4154(13)	1.332(2)	1.1317(7)
	M_{GT}	−0.1544(12)	−0.1476(4)	−0.1374(3)	0.11114(13)
	B_{GT}	$1.02(2)\cdot10^{-2}$	$9.84(3)\cdot10^{-3}$	$9.23(5)\cdot10^{-3}$	$7.05(2)\cdot10^{-3}$
2^+_{2+3}	$M_{0,\mathrm{GT}}$	1.84(2)	1.84(2)	1.84(2)	1.842(5)
2^+_2	E (MeV)	16.544	16.517	16.441	16.756
	θ	0.173	0.223	0.376	0.345
	Γ^o (MeV)	0.355	0.537	1.25	0.475
2^+_3	E (MeV)	16.887	16.879	16.863	17.288
	θ	0.0996	0.116	0.155	1.13
	Γ^o (MeV)	0.120	0.148	0.216	5.19
2^+_4	E (MeV)	37.0	28.7(2)	22.7(6)	14.560(7)
	θ	2.56(7)	2.218(13)	2.02(3)	2.398(6)
	Γ^o (MeV)	126(3)	73.6(4)	43.7(7)	20.97(5)
	M_{GT}	−0.23(2)	−0.26(3)	−0.40(4)	−0.906(3)
	B_{GT}	0.032(6)	0.042(2)	0.10(2)	0.504(3)
γ^2_W (MeV)		1.139	1.058	0.922	0.518
K		1.28	1.67	2.68	−5.45
χ^2/df		0.97	0.97	0.97	0.97

Table 3.2: Level parameters for Models 2–4 in table 3.1. Energies are ^{8}Be excitation energies. The matrix elements given here include the factor $|g_A/g_V| = 1.2695(29)$. This factor is not included in the B_{GT} values.

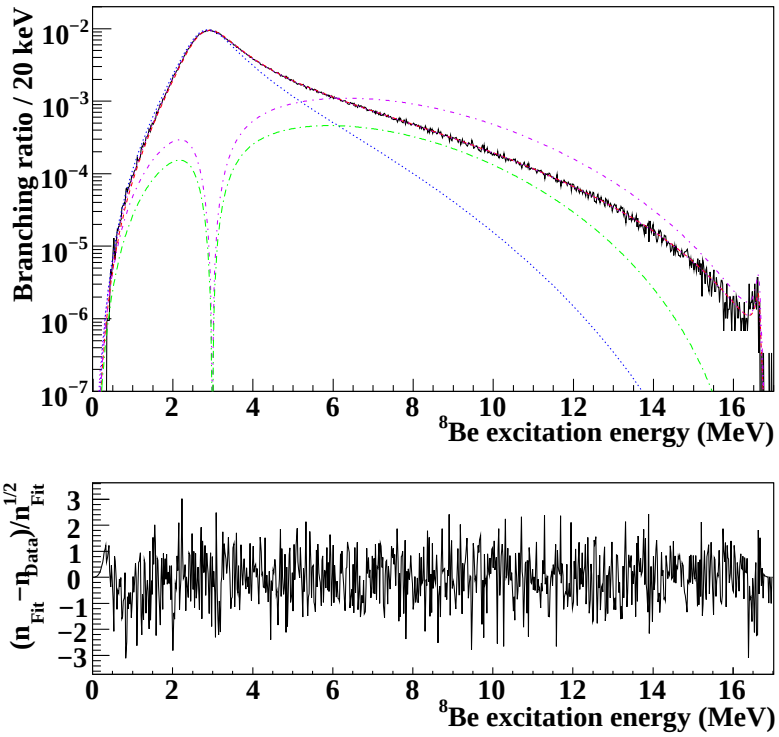

Figure 3.6: Fit to Model 3 in Table 3.1.

was not kept constant in [Barker 1989], only the R-matrix energy of the background level with boundary condition determined at the 3 MeV state energy was fixed, so its observable energy varied in the fit. In this work its observable energy is fixed at 45 MeV, a value similar to the background level energy for $a_c = 6.5$ fm in [Barker 1969]. The energy of the level between the 3 MeV state and the doublet lies between 12 and 14 MeV in fits from $r_0 = 1.8$ fm ($a_c = 5.7$ fm) to $r_0 = 2.4$ fm ($a_c = 7.6$ fm) and χ^2 does not vary significantly for different channel radii. The width of the state is between 13 and 16 MeV, $\sim$ 2 times the Wigner limit. An example fit is shown in figure 3.8 and the parameters for this fit are given in the second column of table 3.3. The 45 MeV level has a very large width, $\Gamma^o \approx 50$ MeV, in all the fits. If the energy of the intruder state is fixed at 9 MeV a good fit can be obtained with a very small change in

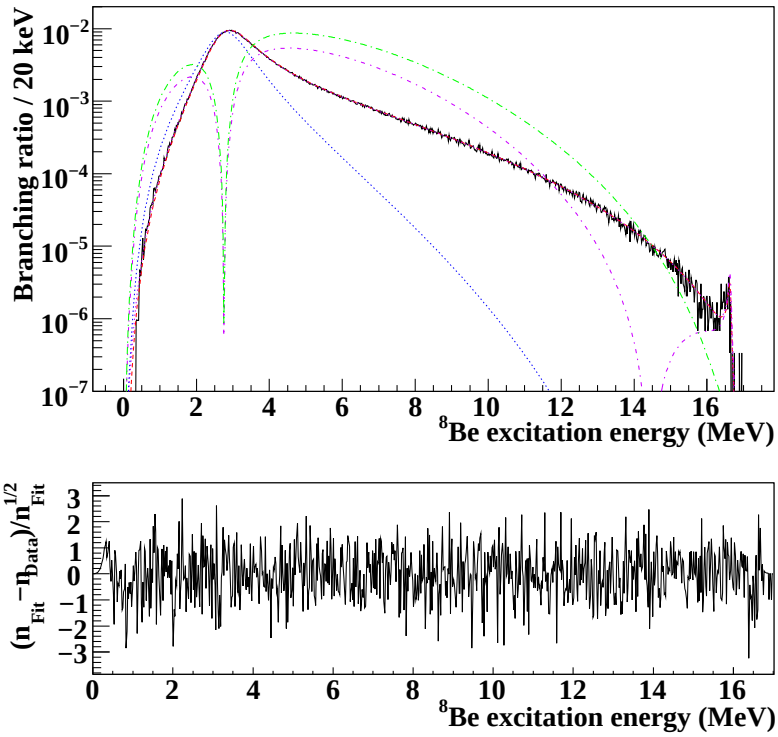

Figure 3.7: Fit to Model 4 in Table 3.1.

χ^2. The width of the intruder state then becomes smaller (Γ^o = 9 MeV) and the width of the background level increases (Γ^o = 78 MeV) (see table 3.3).

The systematic uncertainty of the fits was tested by comparing fits to different energy ranges, and it was found that fits to the energy range 1.5–17 MeV are consistent with fits for 2–17 MeV. The results are also consistent if one changes from a data set with coincidences between detector 1 and the central 6×6 pixels in detector 4 to the data set with coincidences between detector 4 and the central 6×6 in detector 1. Data for detector 2 and 3 was not used for fitting, but the fit results are in excellent agreement with the spectra for these detectors above the 3 MeV peak. Below the peak, small deviations are seen, probably because of a small calibration error of a few keV, which will only be visible in this energy region, where the spectrum changes most

Parameter		Model 5	Model 5
r_0 (fm)		2.047	2.0
2^+_1	E (MeV)	2.711(2)	2.782(2)
	θ	1.1438(10)	1.1283(8)
	Γ^o (MeV)	1.0832(8)	1.1324(8)
	M_{GT}	0.1041(2)	0.11092(15)
	B_{GT}	$6.20(2)\cdot 10^{-3}$	$7.02(2)\cdot 10^{-3}$
2^+_2	E (MeV)	9.0	12.87(2)
	θ	1.857(6)	2.079(12)
	Γ^o (MeV)	8.68(3)	14.64(9)
	M_{GT}	−0.2131(6)	−0.456(2)
	B_{GT}	0.0278(2)	0.1281(14)
2^+_{3+4}	$M_{0,\mathrm{GT}}$	1.75(2)	1.809(10)
2^+_3	E (MeV)	16.635	16.703
	θ	0.169	0.261
	Γ^o (MeV)	0.106	0.272
2^+_4	E (MeV)	16.934	17.025
	θ	0.151	0.393
	Γ^o (MeV)	0.0857	0.622
2^+_5	E (MeV)	45	45
	θ	3.48(4)	2.55(5)
	Γ^o (MeV)	77.6(8)	44.8(9)
	M_{GT}	0	0
	B_{GT}	0	0
γ^2_W (MeV)		0.495	0.518
K		−0.238	−1.97
χ^2/df		0.98	0.97

Table 3.3: Level parameters for Models 5 in table 3.1. See table 3.2 for explanation.

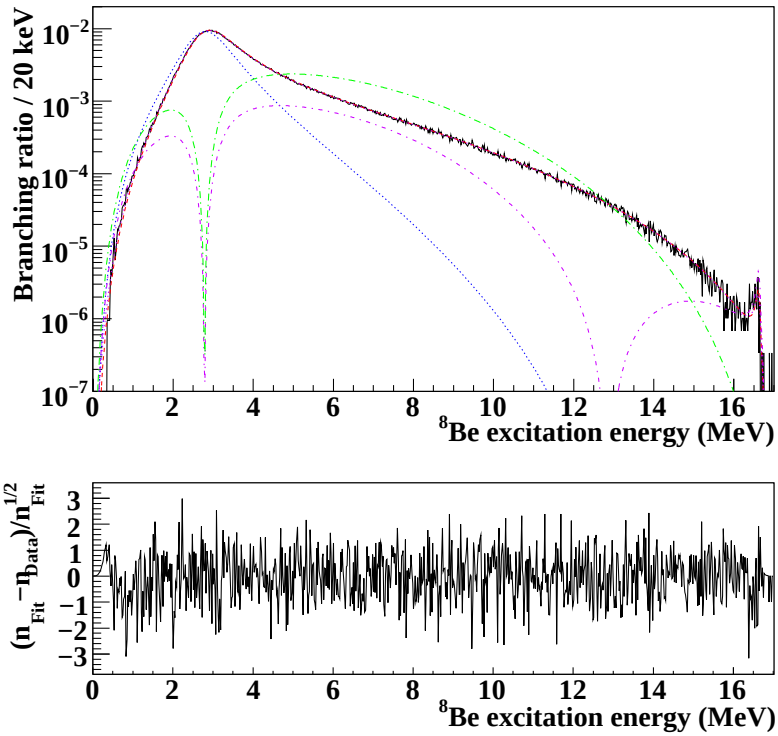

Figure 3.8: Fit to Model 5 in Table 3.1.

rapidly. The fits in tables 3.2 and 3.3 are compared in figure 3.9, where the relative difference between the parameterisations for each of the fits and the fit to Model 3 with $r_0 = 1.5$ fm is shown. The statistical uncertainty from the fit is indicated with the solid lines. The first three models with a 2^+ level above the doublet peaks are consistent within the statistical uncertainty from 0 to 16 MeV, so changing the channel radius does not affect the extrapolation below 1.5 MeV significantly. Above 16 MeV the deviations increase because the strength to the doublet is not very well constrained due to the low amount of counts in this energy region. The models with a 2^+ state below the doublet are seen to differ systematically from the first three models throughout the fit region, but also to be consistent within the statistical uncertainty. Below 1.5 MeV it is evident from the fits that different models will lead to different extrapolations. It is somewhat surprising to see that adding a level with zero

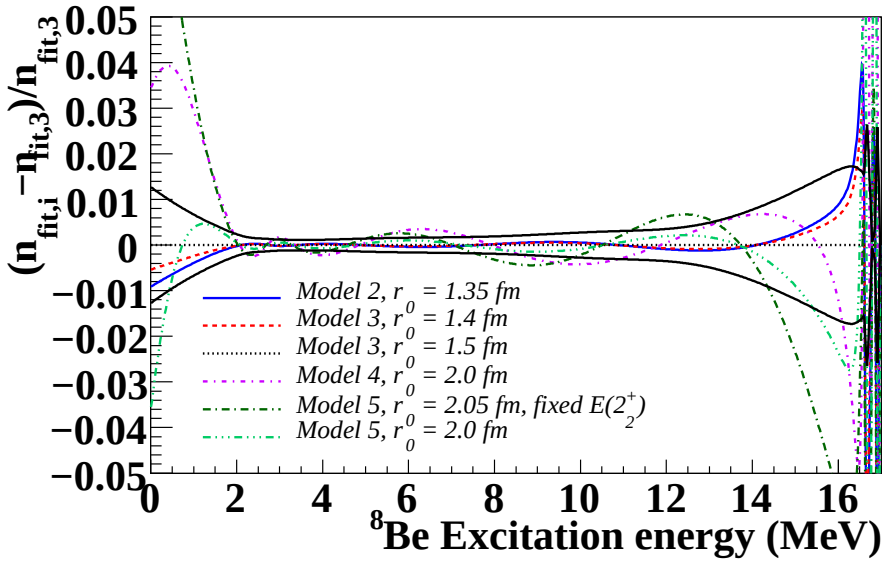

Figure 3.9: The relative difference between each of the fits in tables 3.2 and 3.3 and the fit to Model 3 with r_0 = 1.5 fm (the third model listed). Statistical uncertainty limits on the fit are shown as solid lines.

feeding at 45 MeV changes the extrapolation as much as is seen between the two models for r_0 = 2.0 fm.

In tables 3.2 and 3.3 the doublet parameters are seen to differ very much depending on the model. For models 2–4 with a 2^+ level above the doublet, the term, K, approximating the contribution from interference with other 2^+ states (see equation 3.15), becomes large and positive. This causes the energy parameters to decrease below the peak energies and the width parameters to increase, most significantly for the low-energy doublet state. For the fit to Model 3 with r_0 = 1.5 fm the observed width becomes very large for the low-energy state, Γ^o = 1.25 MeV. The inverse ft value for this fit is shown in figure 3.10 to illustrate that the calculated observed width does not correspond to the width of the peak in this case. The measured spectrum shown for comparison is the sum of coincidences between detector 1 and 4 and detector 2 and 3 in the maximum 14 × 14 strips in both detectors of the pair (the energy dependence of the coincidence efficiency can be neglected in this narrow energy region). The fit is seen to reproduce the experimental data for the low-energy peak.

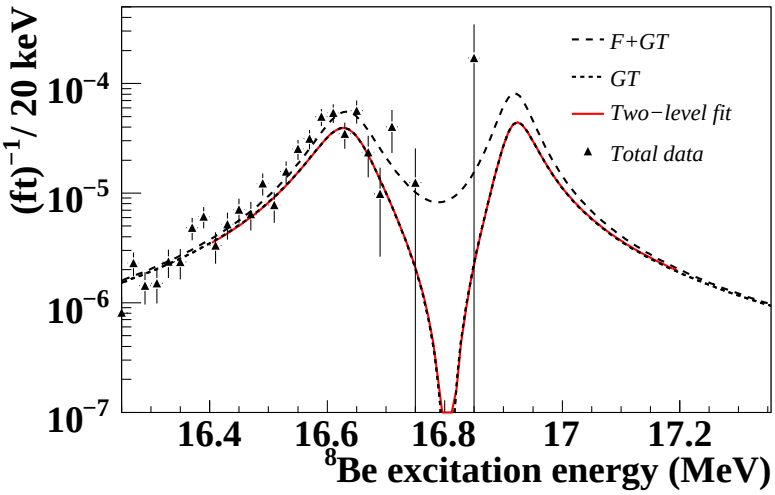

Figure 3.10: The fit from figure 3.6 corrected for the phase space factor, f_β. The dashed curve ($F + GT$) shows the total fit to the data and the finely dashed curve (GT) only the Gamow-Teller contribution. For comparison the measured spectrum is plotted as well. A two-level fit has been performed to the GT strength between 16.4 and 17.2 MeV and the parameters are given in the text.

The Gamow-Teller strength of the parameterisation can be reproduced by a two-level fit (solid line), and the parameters are E_a = 16.7196(5) MeV, Γ_a = 0.1090(14) MeV and E_b = 17.0158(3) MeV, Γ_b = 0.0681(10) MeV (2α energy), confirming the validity of the transformation of the $K = 0$ parameters for the doublet, E_a^0 = 16.715(3) MeV, Γ_a^0 = 0.1077(5) MeV, E_b^0 = 17.017(3) MeV and Γ_b^0 = 0.0744(4) MeV, described in section 3.4.1. The transformation is not exact so small systematic deviations are to be expected. The large effects on the doublet parameters due to interference are consistent with the results in table 6 of [Barker 1969].

The tendency of a decreasing level energy with increasing channel radius is also seen in [Barker 1989] and [Warburton 1986]. It should be noted that Warburton's figure 4 in [Warburton 1986], which shows the level energy dependency on channel radius, actually compares two different R-matrix models. The three points for lowest channel radius are obtained using Model 3 in Table 3.1 and the remaining points for higher channel radius are from Barker's analysis [Barker 1969] using Model 5 in Table 3.1. Figure 3.11 shows the level-

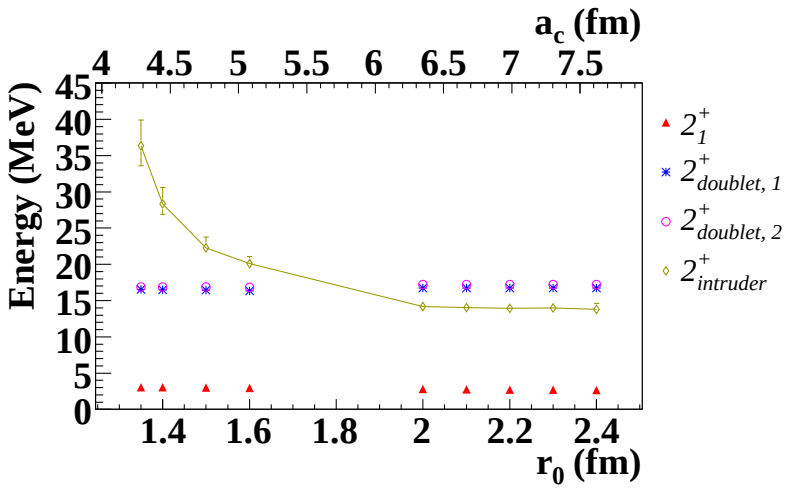

Figure 3.11: *R*-matrix energies for the levels included in Models 3 and 4 in table 3.1 for fits to different channel radii.

energy dependency with channel radius for Models 3 and 4 in Table 3.1. The fit qualities of all the fits used in the figure are almost identical. This confirms the essence of Warburton's similar figure for α-α scattering.

Except for Model 1, all of the above fit models give a very good fit to the data. However, all of the models require levels with very large widths which can not be interpreted as physical resonances. The known 2^+ levels above the isospin doublet at 20.1 and 22.2 MeV do not have large enough widths to affect the spectrum below the doublet significantly. The interpretation of the fit results is discussed in chapter 5. For now, we have a good parametrisation of the final-state distribution, which can be used for the internal consistency check with the single-α spectra, for comparison to other works and finally for the calculation of the ^{8}B neutrino spectrum. The parameterisation used is for Model 3 in table 3.1 given in table 3.2 column 3.

3.5 Internal consistency

The single-α and coincidence spectra are affected differently by the detector response, so to compare the two spectra, a parameterisation from a fit to the coincidence spectrum is used to calculate the single-α spectrum, which is then

folded with the single-α response function before comparison to the measured spectrum.

The single-α spectrum cannot be directly converted to a ^{8}Be excitation spectrum, due to the effect of lepton recoil. A simple and general approximation of this broadening effect is given in [Bhattacharya 2002]:

$$\frac{dN}{dE}(x) = \frac{15}{16T_{max}}(1 - 2x^2 + x^4), \qquad -1 \leq x \leq 1 \tag{3.21}$$

where $x = \delta E/T_{max}$ and δE is the α-energy difference between the measured energy and the energy for no recoil broadening. The maximum α-energy shift due to recoil is

$$T_{max}(E_x) = \sqrt{W_0^2 - 1}\frac{m_e}{M}\sqrt{2Qmc^2\frac{M - m - Q}{M - Q}}, \tag{3.22}$$

where E_x is the ^{8}Be excitation energy, m_e, m and M are the electron, α-particle and ^{8}Be masses, $W_0(E_x) = (Q_\beta - E_x + m_e c^2)/m_e c^2$ is the β end point total energy in units of $m_e c^2$, $Q_\beta = 17.9798$ MeV $- 2m_e c^2$ and $Q = E_x + 91.8$ keV. The parametrisation of the sum spectrum from the R-matrix analysis has been folded with the recoil distribution (equation 3.21) to reproduce the single-α spectrum. The result is shown in figure 3.12. The top graph shows the measured single-α spectrum compared to the spectrum reproduced from the parameterisation of the excitation energy spectrum from fit model 3 in table 3.1. A small shift in the residuals is seen at 1.5 MeV corresponding to a shift in the peak position in the two spectra of $\sim$ 1.5 keV. Allowing for this small error in the calibration, the 2α and single α spectra are seen to be mutually consistent down to a single-α energy of $\sim$ 0.6 MeV, corresponding to an excitation energy of $\sim$ 1.1 MeV.

3.6 ^{8}B β decay in the literature

The β decay of ^{8}B and subsequent ^{8}Be(2α) breakup has been measured in several experiments with different techniques. The ^{8}Be excitation energy spectrum from this work is compared to other works in figure 3.13. The spectra are scaled to show the number of counts in 20 keV energy bins. It is clearly seen that the statistics in this work is far superior to previous coincidence

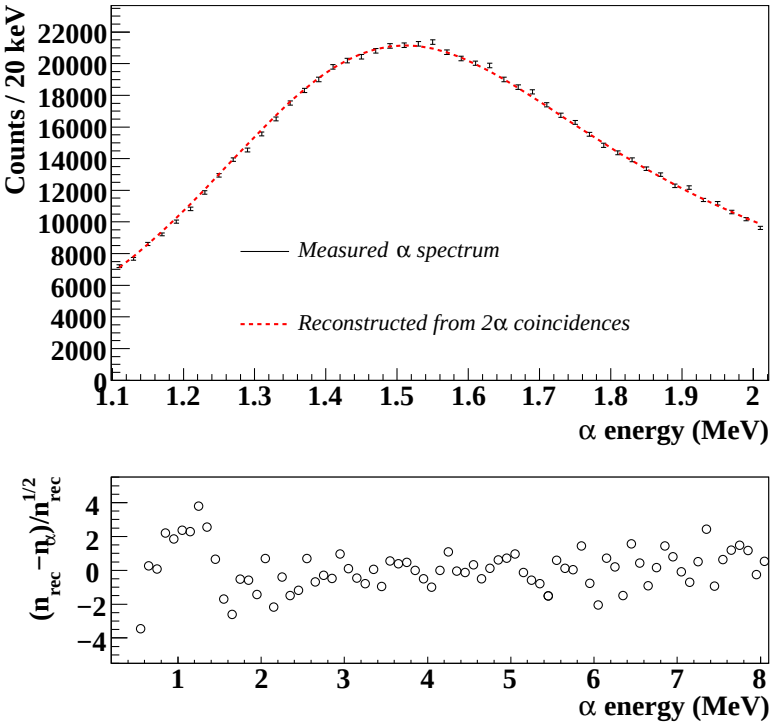

Figure 3.12: Top: The 3 MeV peak region of the measured single-α spectrum (black markers with error bars) compared to the single-α spectrum reproduced by recoil broadening of the ^{8}Be(2α) final-state distribution from fit model 3, folded by the single-α response function (red, dashed line). Bottom: Residuals between the reconstructed and measured spectra.

measurements. The spectra measured by Wilkinson and Alburger [Wilkinson 1971] and by Bhattacharya *et al.* [Bhattacharya 2006] are single-α measurements, which need to be corrected for recoil broadening. The data spectrum shown here from [Wilkinson 1971] has not been corrected, while the spectrum from [Bhattacharya 2006] is the parametrisation from an *R*-matrix fit and therefore corrected for recoil broadening. The spectrum by Ortiz *et al.* [Ortiz 2000] is from a coincident measurement of the 2α breakup and the spectrum from Winter *et al.* [Winter 2006] is an *R*-matrix parametrisation to data from an implantation measurement, affected by a small amount of β energy deposited in the detector.

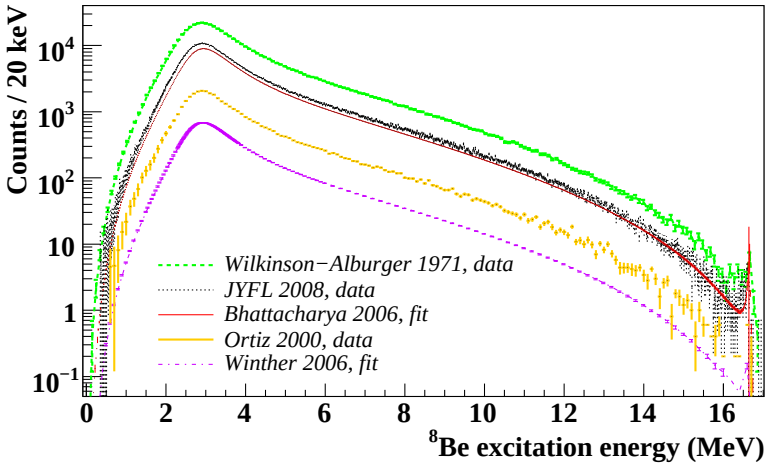

Figure 3.13: Comparison of ^{8}Be(2α) decay spectra from ^{8}B β-decay measurements. From the top are shown spectra from Wilkinson and Alburger (single-α data) [Wilkinson 1971], this work (JYFL 2008, 2α coincidence data), Bhattacharya *et al.* (fit to single-α data) [Bhattacharya 2006], Ortiz *et al.* (2α coincidence data) [Ortiz 2000] and Winter *et al.* (fit to 2α sum spectrum) [Winter 2006].

The single-α spectrum from this work is inconsistent with the spectrum measured by Wilkinson and Alburger provided in [Barker 1989], both for the original calibration (equation 1 in [Barker 1989]) and Barker's alternative calibration (equation 15 in [Barker 1989]).

In figure 3.14 the spectra have been normalised to compare the shape of the 3 MeV peak. Wilkinson and Alburger's spectrum have been omitted, because it has not been corrected for lepton recoil broadening. The final-state distribution from this work lies in between the data spectrum from [Ortiz 2000] and the internally consistent distributions from [Winter 2006] and [Bhattacharya 2006]. If the parametrisation from [Bhattacharya 2006] is shifted by $\sim$ 25 keV to lower energy it agrees with the final-state distribution from this work, except at high energy, where the isospin doublet was not treated correctly as discussed in section 3.4.1. The 3 MeV peak is narrower in the fit to the JYFL data than was the case in [Winter 2006] and [Bhattacharya 2006] as is also seen by comparison of the reduced width for the fit to Model 2 in table 3.2. The width of the 37 MeV level is consistent with [Winter 2006] and the

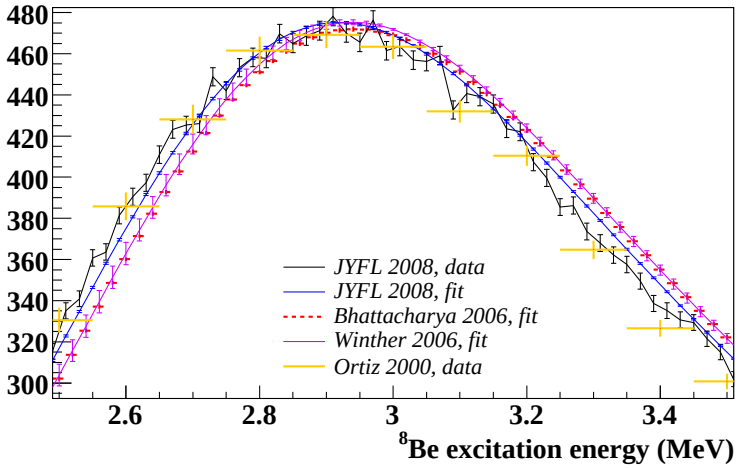

Figure 3.14: ^{8}Be(2α) decay spectra normalized to 1000 with 20 keV energy bins. This work is compared to the final-state distributions from *R*-matrix fits in [Bhattacharya 2006] and [Winter 2006] and to the data spectrum from [Ortiz 2000]. The maximum in the fit to this work is shifted by 15 keV relative to the measured spectrum due to the asymmetric detector response.

β strength with the result in [Bhattacharya 2006]. The *R*-matrix energy of the 3 MeV level is larger in the fit presented here because of the smaller channel radius used. The Gamow-Teller matrix element for the doublet peak is here 0.6 times the value in [Bhattacharya 2006] and 0.8 times the value from [Winter 2006] because of the value of $K = 1.28$ significantly changing the doublet parameters from their literature values.

3.7 Energy of the 2^+_1 state in ^{8}Be

The 2^+_1 state at about 3 MeV in ^{8}Be is very broad and its shape is modified by the interference with other 2^+ states in ^{8}Be. The level energy of the state therefore depends on the specific model chosen to parameterise the data. For example Barker's model with an intruder state between the 3 MeV state and the isospin doublet will give a lower level energy of the 3 MeV state than models with only high-energy background states because of interference between the 3 MeV state and the intruder. Furthermore, the level energy will

Definition	Symbol	Energy (MeV)
^{8}B β-decay fsd. peak pos.	E^{β}_{peak}	2.9185(9)
Resonance dist. peak pos.	$E^{\text{res}}_{\text{peak}}$	2.8688(9)
R-matrix level energy	E_λ	2.985(2)

Table 3.4: Different definitions for the level energy of a broad resonance with precise values given for the ^{8}Be 2_1^+ state from the present data. Statistical uncertainties are given in parenthesis, the systematic uncertainty is $\sim$ 6 keV.

depend on the choice of channel radius, since the level energy of the intruder state is lowered for higher channel radii, pushing the 3 MeV state to lower level energies. When recommending a particular energy as the level energy of a broad resonance it should therefore be made clear from which context the figure was obtained. This issue was discussed in the compilation of energy levels for A = 5–7 nuclei [Tilley 2002] (page 12).

In table 3.4 the energy of the 2_1^+ state is given very precisely for three different definitions. The uncertainties given are statistical uncertainties. The systematic uncertainty in the calibrations is estimated to $\sim$ 6 keV at 3 MeV [Kirsebom 2010a]. The first energy was obtained as the peak energy in the final-state distribution for ^{8}B β decay. This energy is directly obtained from the spectrum in figure 3.13 but is only relevant in the context of ^{8}B β decay since the distribution is modified by the β-decay phase space and penetration function for the α channel. A definition less dependent on the entrance and exit channels is the peak position in the resonance distribution in figure 3.3. In this plot the phase space and penetration function dependencies have been removed. This definition will typically not coincide with the level energy from an R-matrix parametrisation due to interference. Different types of experiments will also not feed the involved states with the same strength and this will shift the peak position of interfering states. The last definition in table 3.4 is based on the R-matrix level energy. The tabulated energy in table 3.4 is from Model 3 in table 3.1 with only a background contribution from above the isospin doublet. For such a model the level energy of the 3 MeV state is less affected by the background, which will be a slowly varying contribution at the 3 MeV peak and does not push the 2_1^+ level far below the peak energy.

3.8 Neutrino spectrum

The neutrino spectrum for ^{8}B β decay can be deduced from the measured 2α energy distribution. This was done in the work by Winter et al. [Winter 2006] including recoil order effects. In this section we shall investigate how our slightly different 2α spectrum will affect the neutrino spectrum.

The positron spectrum for β^+ decay is given by [Winter 2006]

$$\frac{dN}{dE_\beta} = p_\beta E_\beta (E_0 - E_\beta)^2 F(Z, E_\beta) R(E_\beta, E_0) C(E_\beta, E_0), \tag{3.23}$$

where p_β and E_β are the momentum and total energy of the positron, and E_0 is the positron end point energy, $E_0(E_x) = Q_\beta - E_x + m_e c^2$. $F(Z, E_\beta)$ is the Fermi factor. Radiative corrections are contained in $R(E_\beta, E_0)$ and the recoil corrections are contained in $C(E_\beta, E_0)$. If kinetic recoil of the daughter nucleus is neglected the positron spectrum is obtained by integration of equation 3.23 over all excitation energies weighted by the final-state distribution from the fit. The neutrino energy is the remaining energy in the decay: $E_\nu = E_0 - E_\beta$.

Neglecting recoil and radiative corrections we obtain the neutrino spectrum shown in figure 3.15 (JYFL simple). This spectrum is shifted slightly to lower energy compared to the spectrum tabulated in [Winter 2006] including recoil order effects. To separate out the effect of the 2α spectrum on the neutrino spectrum we compare the neutrino spectra calculated without recoil order effects using the 2α spectra from this work and [Winter 2006] respectively. The ratio between this work and [Winter 2006] is shown in figure 3.16. From Fig. 3.16 it is evident that our 2α spectrum gives a significant difference in the neutrino spectrum. Because the errors on the extracted 2α final-state ditribution are so small, the uncertainties in the neutrino spectrum will be determined by the uncertainties in the recoil correction factor. Winter et al. state in [Winter 2006] that the uncertainties in the neutrino spectrum from recoil order effects are roughly half as large as the uncertainties from the α-spectrum measurements, so with the new α data we can obtain a neutrino spectrum with roughly half as large error bars.

The effect of correcting for recoil order effects is shown in figure 12 of [Winter 2006]. To obtain an approximate neutrino spectrum corrected for recoil order effects from this work, one can multiply the simple neutrino spectrum

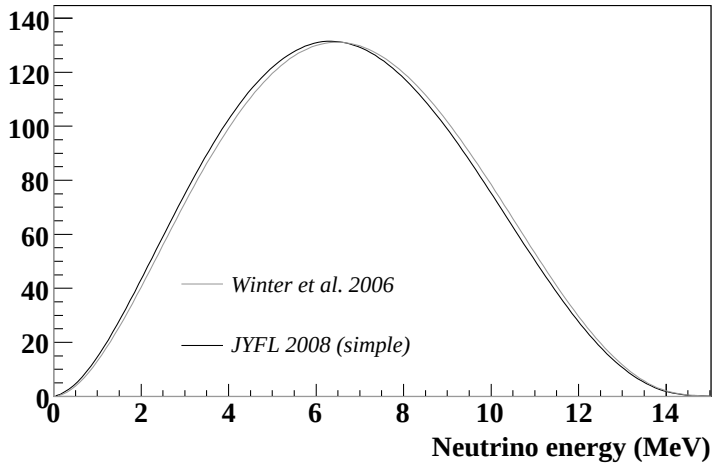

Figure 3.15: The neutrino spectrum calculated without recoil corrections (JYFL simple) compared to the spectrum tabulated in [Winter 2006] (Winter et al. 2006).

in figure 3.15 by this factor. The correction is not exact, since the 2α strength is used for calculating the recoil effect. Work is in progress to perform a full calculation of the neutrino spectrum from the present work.

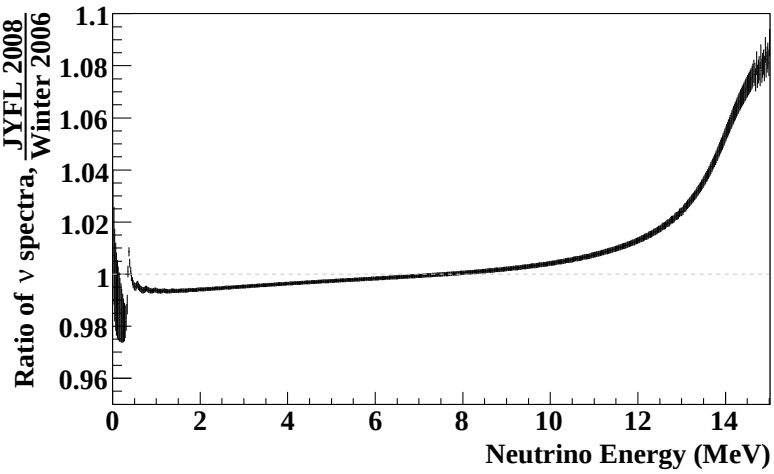

Figure 3.16: The ratio between the neutrino spectra calculated without recoil corrections using ^{8}Be(2α) decay spectra from this work and [Winter 2006] respectively.

CHAPTER 4

Beta decay of ^{12}N and ^{12}B

In this chapter, two complementary experiments utilising β decay of ^{12}B and ^{12}N to study unbound states in ^{12}C will be presented. The first was a complete kinematics experiment performed in 2004 at the Jyväskylä Accelerator Laboratory, Finland. The analysis of the 3α coincidence data from this experiment constituted a major part of the PhD work by C. Aa. Diget [Diget 2006]. The work presented in section 4.2 is a parallel analysis of the single-α data as a consistency check of the 3α analysis and for a more direct comparison to previous single-α measurements. The second experiment was an implantation experiment performed in 2006 at KVI in Groningen, The Netherlands. In section 4.5, model independent branching ratios will be extracted from the two experiments, and both data sets will be used for a simultaneous R-matrix analysis in section 4.6.

4.1 Motivation

The Hoyle state at 7.65 MeV in ^{12}C, just above the threshold for breakup to three α particles, is famous for its anthropic prediction by Hoyle in 1953 [Hoyle 1953] and subsequent discovery [Dunbar 1953]. The existence of the Hoyle state is today well verified, and is known to have spin and parity 0^+ [Cook 1957], but its structure remains to be understood. Depending on the structure of the Hoyle state the first, 2^+, collective excitation of the Hoyle state will be located at different energies [Freer 2009]. Morinaga first proposed the existence of such a 2^+ excitation based on a linear 3α-chain model of the Hoyle state [Morinaga 1956]. The energy of the 2^+ state would be 9.70 MeV, and an additional 4^+ excitation was predicted at 14.18 MeV. In the 1950s not much was known about the spin-parity of states in the 3α continuum, but a known state existed at 9.6 MeV, which Morinaga assumed to

be his 2^+ state. Later the spin-parity of this state has been assigned to 3^- (E_x = 9.641 MeV). The first beta-decay experiments studying the 3α continuum in ^{12}C in the late 1950s and 1960s saw a broad resonance at $\sim$ 10 MeV with a 3 MeV width [Cook 1958, Wilkinson 1963, Schwalm 1966], and subsequently it was adopted as the 2^+ state by Morinaga [Morinaga 1966]. The spin-parity of the 10 MeV state has remained uncertain up till the last decade due to experimental difficulties such as its short lifetime and the overlapping 9.641 MeV 3^- and 10.84 MeV 1^- states. The correct assignment is now known to be 0^+ [Diget 2005, Itoh 2004]. Up to this date several experimental indications of 2^+ states in the low-energy 3α continuum have been presented [John 2003, Itoh 2004, Freer 2007b, Freer 2009], but a consistent picture has not yet emerged.

The unbound 2^+ state could possibly contribute to the triple-α reaction at high temperatures depending on its energy and radiative width. A 2^+ state at 9 MeV with Γ = 0.56 MeV suggested by Descouvemont and Baye [Descouvemont 1987] has been included in the NACRE compilation of astrophysical reaction rates [Angulo 1999].

β decay of ^{12}N and ^{12}B populate only 0^+, 1^+ and 2^+ states in ^{12}C due to the selection rules, and apart from the three narrow states at 7.65 MeV (0^+ Hoyle state), 12.71 MeV (1^+) and 15.11 MeV (1^+), the spectrum consists of broad components which are overlapping and interfering 0^+ and 2^+ states (see figure 4.1). This makes β decay the ideal tool to search for a second 2^+ excited state. In reaction experiments the spectrum will also consist of the strong peaks at 9.64 MeV (3^-), 10.84 MeV (1^-), 11.83 MeV (2^-) and 14.08 MeV (4^+) in the energy window for β decay (see figure 1.5). The same will be the case for scattering experiments such as proton scattering, ^{12}C(p, p'), [Freer 2009] and α-particle scattering, ^{12}C(α, α'), [Itoh 2004]. The reported 2^+_2 state in [Freer 2009] at 9.6(1) MeV overlaps with the 3^- state at 9.64 MeV, and if this state is populated in β decay its peak profile should be clearly visible. The β-decay method is limited to low excitation energies by the decreasing phase space in the decay going to zero at the Q-value. Furthermore only states with a non-negligible overlap with the ground states of the parent nuclei can be populated.

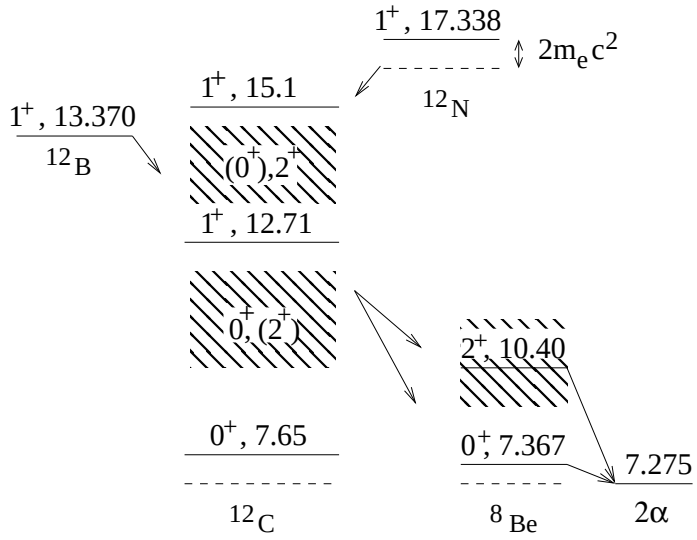

Figure 4.1: Level diagram for ^{12}C populated in β decay of ^{12}N and ^{12}B. 3α breakup via intermediate states in ^{8}Be is illustrated.

4.2 3α coincidence experiment

The ^{12}N and ^{12}B β-decay experiments in the 1950s and 1960s measured spectra of individual α particles from the triple-α breakup of ^{12}C [Cook 1958, Wilkinson 1963, Schwalm 1966]. Today, the experimental techniques allow for complete kinematics measurements of the breakup, and β-decay studies have achieved information about the ^{12}C states and their breakup mechanism with an unprecedented level of detail [Fynbo 2005, Diget 2005]. The experiment presented in this section is the latest in a series of complete kinematics measurements of β-delayed breakup of ^{12}C. It was performed in 2004 at the IGISOL facility of the Jyväskylä Accelerator Laboratory (JYFL), Finland.

4.2.1 Experimental method

The experimental method is very similar to the one described in section 3.2. The ^{12}N and ^{12}B isotopes were produced and separated using the IGISOL method. The ^{12}N nuclei were produced with a ^{12}C$(p,n)^{12}$N reaction using a 25 μA, 28 MeV proton beam impinging on a 1400 μg/cm^2 carbon foil. ^{12}B was produced using a ^{11}B$(d,p)^{12}$B reaction with a 10 μA, 10 MeV deuteron

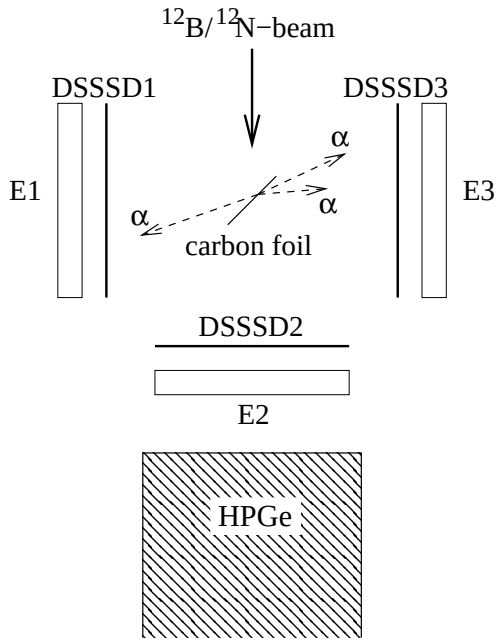

Figure 4.2: Experimental setup.

beam on a 500 μg/cm^2 natural boron target. After extraction from the target the nuclei are accelerated to 25 keV and mass separated before reaching the detector setup.

The detector setup is shown in figure 4.2. The ^{12}B and ^{12}N nuclei were stopped in a thin, 2 cm diameter carbon foil of thickness 33 μg/cm^2 rotated 45° with respect to the beam direction. In the foil, the nuclei would β decay and subsequently break up to three α particles. Surrounding the foil were placed three double sided silicon strip detectors (DSSSDs) for α-particle detection. DSSSD1 and DSSSD3 were of the same design as described in section 3.2. DSSSD2 was of an older design and its larger contact grid yielded a detector dead layer equivalent to 630 nm silicon. All α particles hitting a DSSSD are fully stopped in the detector. The horseshoe configuration of the DSSSDs seen in figure 4.2 was chosen to obtain a large solid angle coverage and a high sensitivity to decays via the ground state of ^{8}Be [Diget 2006].

Positrons and electrons from the decays deposit only a small amount of energy in the DSSSDs and pass through them easily. Instead they are stopped in the thick, unsegmented silicon detectors behind each DSSSD. The γ-rays from

the α-stable 4.44 MeV state were detected in a 70% high purity germanium (HPGe) detector placed with its end cap into a tube going into the detector chamber, about 6.5 cm from the implantation point.

The calibration of the detectors was performed using offline sources of ^{148}Gd and ^{241}Am. An online source of ^{20}Na was used for testing the energy calibration as well as the setup geometry and the dead layer and foil energy losses derived from this geometry. The calibration was performed by C. Aa. Diget and has been described in detail elsewhere [Diget 2006].

4.2.2 Gamma efficiency

The HPGe detector was calibrated after the experiment using two off-line sources: A ^{133}Ba and ^{152}Eu source (JYFL 14) and a ^{228}Th source (JYFL 50). The maximum γ-ray energy emitted by these sources is 1.4 MeV, but the energy, we are interested in, is 4.44 MeV from γ-decay of the first excited state in ^{12}C, so to obtain the efficiency at higher energy we compare to a reference calibration for energies up to 7 MeV performed for another detector setup [Kankainen 2006]. The reference calibration was performed using offline sources of ^{60}Co, ^{134}Cs and ^{228}Th and an online high-energy source of ^{24}Al.

The efficiency calibration for the full energy range is shown in figure 4.3 as open-circle markers. The black line is a fit of the data points to the function:

$$\log \varepsilon = a_1 + a_2 \log E + a_3 (\log E)^2, \tag{4.1}$$

which has been shown to be a valid approximation for energies from $\sim$ 200 keV to $\sim$ 2500 keV [B. Jäckel 1987], but is used for the entire energy range and is seen to reproduce the trend in the data nicely. The fit-parameter values are $a_1 = -3.13(13)$, $a_2 = 1.60(3)$ and $a_3 = -0.183(3)$, giving the efficiency in percent at an energy in keV. Inserting $E = 4439$ keV gives the efficiency $\varepsilon = 0.074(3)\%$. The systematic uncertainty in the validity of the parametrisation up to high energies is estimated by performing a fit including only the data points above 1.37 MeV. The resulting efficiency at 4.44 MeV is $\varepsilon = 0.069(5)\%$. This leads to a revised uncertainty of the efficiency: $\varepsilon = 0.074(5)\%$.

The scaling factor between the reference calibration and the absolute efficiencies for sources at the foil position was found as a weighted average of the

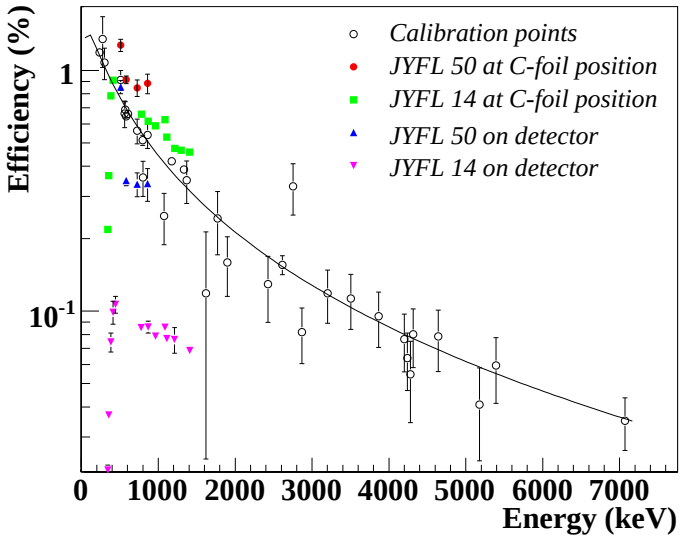

Figure 4.3: Efficiency of the HPGe γ-detector. The solid curve is a fit to the data points with open circle markers from an efficiency measurement for a different detector setup.

ratios between the absolute efficiencies shown with filled circles and squares in figure 4.3 and the black curve. The 4 lowest data points for JYFL 14 were omitted as they are seen to bend off at low energies, which is not the case for the other data. The scaling factor was found to be:

$$\frac{\varepsilon_{abs}}{\varepsilon_{cal}} = 1.30(10). \tag{4.2}$$

Multiplying by this factor the efficiency at 4.4 MeV becomes:

$$\varepsilon_{abs}(4439\text{keV}) = 0.096(10)\%. \tag{4.3}$$

The efficiency was also measured with the sources directly on the detector, and these measurements are shown as the triangular markers in figure 4.3. These efficiencies are seen to be much below the efficiencies for sources at the foil position, which is the opposite of what you would expect, since a much larger solid angle is covered when the source is directly on the detector. An explanation for the lower efficiency is, that the activities of the sources are too high for the data acquisition system to register all the gammas.

Although the measured efficiencies for sources directly on the detector are wrong, we do trust that the efficiency measurements are correct when the

sources are at the foil position. This is supported by the ratio between the absolute and calibration efficiencies, which seems reasonable, judging from the source-detector distances used in the two measurements. Furthermore the efficiency calibration is tested by calculating absolute branching ratios for β-decay of ^{20}Na.

4.3 Relative branching ratios

In this section the JYFL data will be analysed to obtain relative branching ratios. Both triple-α and single-α spectra will be analysed to obtain an internal consistency check, and the single-α analysis also provides a link to the early β-decay studies, where only single-α spectra were obtainable [Cook 1958, Wilkinson 1963, Schwalm 1966].

4.3.1 Triple-α sum-energy spectra

The three α particles in the breakup can be detected in coincidence in the DSSSDs with an energy dependent efficiency between 1 and 4% (see figures 6.2.8 and 7.4.1 in [Diget 2006]). Breakups via the ground state in ^{8}Be, 92 keV above the 2α threshold, can be separated from the remaining events, owing to the fact that the ^{8}Be energy is identified as the relative kinetic energy of the two low-energy α particles [Diget 2009]. The 3α coincidence efficiency depends on the decay channel and for each channel the efficiency has been determined with a Monte Carlo simulation. For the ^{8}Be ground state channel the uncertainties on the efficiency are determined by uncertainties in the geometry of the detector setup and are of the order 5-10%. For the remaining events the decay channel is unknown, and the efficiency varies depending on the initial spin of ^{12}C, the ^{8}Be spin and the angular momentum. The fact that the decay channel is unknown leads to an uncertainty in efficiency of the order 20%.

The efficiency corrected 3α sum-energy spectra for ^{12}N and ^{12}B are shown in figure 4.4. Due to the energy deposition in the stopping foil and detector dead layers there is a low-energy cut-off and the Hoyle state at 0.3794 MeV is not detected. The most prominent feature in the spectra is the peak corresponding to a 1^{+} state at 12.71 MeV excitation energy. At lower energies

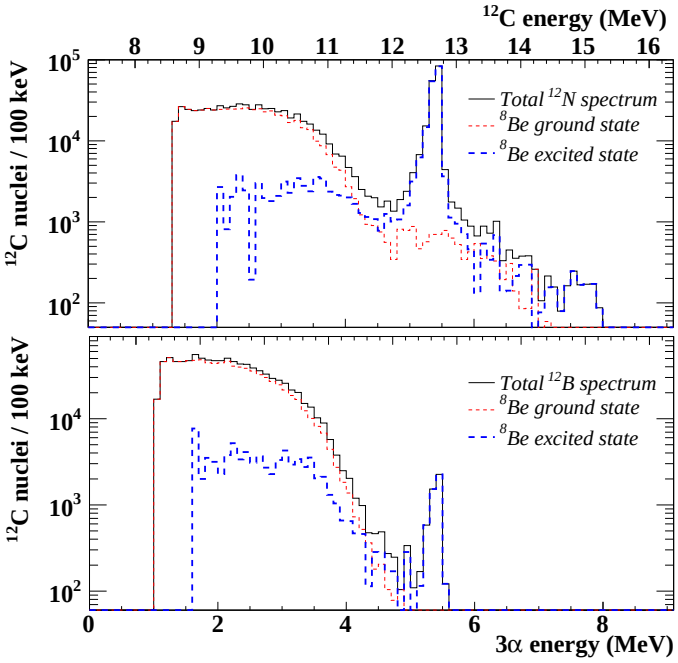

Figure 4.4: Efficiency corrected 3α sum-energy spectra.

a broad distribution is seen, assigned as the 10.3 MeV state in the literature. The low-energy part of this feature is not seen due to the cut-off. Above and overlapping with the 1^+ state another broad distribution is apparent in the ^{12}N data.

From the sum spectra in figure 4.4 one can determine the relative branching ratios to excitation energies above 9 MeV in ^{12}C. The branching ratios are given relative to the sum spectrum from 9 to 16.3 MeV in table 4.1.

4.3.2 Single-α spectra

The total single-α spectra for ^{12}N and ^{12}B are shown in figure 4.5. The detection efficiency for single α particles is energy independent as opposed to the 3α coincidence efficiency, but the relative branching ratios can not be determined as directly from the spectra as was the case in the triple-α analysis because single-α spectra for different ^{12}C excitation energies overlap. Because of the three-particle final state each excitation energy in ^{12}C produces a continuous single-α spectrum ranging from close to zero energy up to a maximum

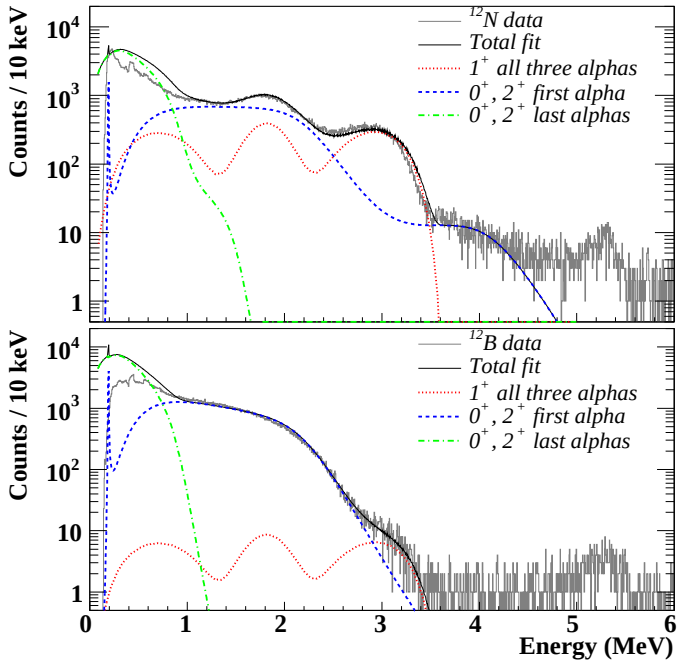

Figure 4.5: Total single-α spectra for ^{12}N and ^{12}B β decay.

value of $\frac{2}{3}(E_x - S_{3\alpha})$, where $S_{3\alpha}$ is the 3α separation energy in ^{12}C equal to 7.275 MeV. The maximum single-α energy for ^{12}N decay is therefore 6.03 MeV and for ^{12}B decay it is 4.06 MeV.

In each breakup, the individual α energies are determined by the break-up mechanism, so to understand the composition of the single-α spectra the break-up mechanism of each contributing state must be understood. In earlier works the breakup of the 12.71 MeV state was not well understood [Wilkinson 1963, Schwalm 1966], but this has now been clarified somewhat and the data is well reproduced with a sequential model of the decay via the first excited state in ^{8}Be [Fynbo 2003, Balamuth 1974]. The physical break-up mechanism is however not perfectly sequential as shown in [Kirsebom 2010b] in the sense that the Coulomb interaction with the first α particle is non-negligible in the secondary breakup of the ^{8}Be compound. The breakups of the broad components in the spectra have been analysed using the 3α coincidence data from the present experiment and it has been shown that they consist of 0^+ and 2^+ states which breakup via both the ground state and higher energies in

^{8}Be [Diget 2009]. In earlier works the broad single-α spectrum was interpreted as a single 10.3 MeV state breaking up via the ground state of ^{8}Be [Cook 1958, Wilkinson 1963, Schwalm 1966].

In figure 4.5 the spectra have been decomposed into contributions from the 12.71 MeV, 1^+ state and the broad, 0^+ and 2^+ components respectively. The single-α distribution from breakup of the 12.71 MeV state is taken from [Diget 2006], where a Monte Carlo simulation of the breakup was performed. The broad 0^+ and 2^+ components are treated as decaying sequentially via the ground state of ^{8}Be in this analysis. Although higher energies in ^{8}Be are known to contribute (see figure 4.4), they contribute less than 10% below 12 MeV, so the simple description of the breakup is used for the purpose of comparison. The decay process is illustrated in figure 4.6, showing the velocities of the α particles. The Q-value is denoted ε_1 for the first decay step,

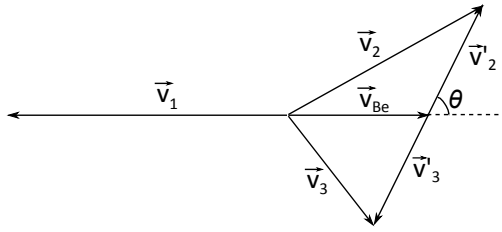

Figure 4.6: Triple-α breakup via an intermediate state in ^{8}Be.

$^{12}C^* \rightarrow^{8}$ Be + α_1, and ε_2 for the second, ^{8}Be $\rightarrow \alpha_2 + \alpha_3$. The energies of the three emitted α particles can be calculated from energy and momentum conservation using the relations shown in figure 4.6 between the velocities in the center of mass system and the ^{8}Be rest frame.

$$E_1 = \frac{2}{3}\varepsilon_1, \tag{4.4}$$

$$E_2 = \frac{\varepsilon_2}{2} + \frac{\varepsilon_1}{6} + \sqrt{\frac{\varepsilon_1\varepsilon_2}{3}}\cos\theta, \tag{4.5}$$

$$E_3 = \frac{\varepsilon_2}{2} + \frac{\varepsilon_1}{6} - \sqrt{\frac{\varepsilon_1\varepsilon_2}{3}}\cos\theta. \tag{4.6}$$

The ground state of ^{8}Be has spin-parity 0^+, so α_2 and α_3 are emitted isotropically in the ^{8}Be rest frame. Therefore the energies of the last emitted α particles are distributed uniformly from $E_{\min} = \frac{\varepsilon_2}{2} + \frac{\varepsilon_1}{6} - \sqrt{\frac{\varepsilon_1\varepsilon_2}{3}}$ to $E_{\max} = \frac{\varepsilon_2}{2} + \frac{\varepsilon_1}{6} + \sqrt{\frac{\varepsilon_1\varepsilon_2}{3}}$.

A three-level *R*-matrix model has been used to parameterise the ^{8}Be ground-state component of the 3α sum-spectrum in figure 4.4. One 0^+ and one 2^+ state were included in the model apart from the 0^+ Hoyle state. From this the energy spectra for the first and last two emitted α particles shown in figure 4.5 were calculated.

In the combined fit to the ^{12}N and ^{12}B data only data above 1.2 MeV were included to avoid the low-energy cutoff and the β background. The ratio between the 12.71 MeV 1^+ component and the energy distribution of the first emitted α particles from the broad states was found in the fit, and also the reduced width, energy and β strength parameter for the broad 0^+ state were varied in the fit. *R*-matrix parameters for the Hoyle state and 2^+ state were taken from [Diget 2006]. The energy distributions of the last emitted α particles were calculated after the fit had converged.

For ^{12}N there is a deviation between the data and the fit around 3.5 MeV, which is caused by a deficiency in the simulated spectrum for decay via the 1^+ state. As discussed in [Diget 2006] and [Kirsebom 2010b] the Coulomb repulsion between the first emitted α particle and the two α particles from ^{8}Be, which is neglected in the simulation, causes a small distortion of the spectrum. The small peak at 5.3 MeV is due to background from a ^{223}Ra source in the beam-line used for beam tuning.

Relative branching ratios from the single-α spectra are found by integrating the curves. The integral of the dashed curve equals the number of decays to the broad components, and this distribution is integrated from 1.2 MeV to 3.2 MeV and from 3.2 MeV to 6.1 MeV to give the relative branching ratios in table 4.1. One third of the area under the dotted curve equals the contribution from the 1^+ state, since all three α particles from the decay contribute to the distribution. Also the small γ width of the 1^+ state is taken into account. The assumption that the broad states break up via the ground state in ^{8}Be is known to be wrong, and to allow for this a systematic uncertainty is added to the relative branching ratios in table 4.1 estimated from the now known ratios between breakup through higher energies in ^{8}Be vs. the ground state from the triple-α analysis. It is gratifying that the single-α and triple-α results are consistent, and since this is the case, combined values of the two methods are given in table 4.1.

^{12}C	^{12}N			^{12}B		
Energy (MeV)	Single alpha	Triple alpha	Comb.	Single alpha	Triple alpha	Comb.
9 – 12	0.772(14)	0.75(2)	0.765(12)	0.995(2)	0.9940(10)	0.9940(10)
12.7	0.207(15)	0.21(2)	0.209(12)	0.0054(11)	0.0058(10)	0.0056(8)
12 – 16.3	0.017($^{20}_{3}$)*	0.042(10)	0.042(10)		0.0011(5)	0.0011(5)

Table 4.1: Relative branching ratios for the decays of ^{12}N and ^{12}B to the triple-α continuum. The branching ratios are given relative to the sum spectrum from 9 to 16.3 MeV. The branching ratio to the 12 – 16.3 MeV region does not include the 12.71 MeV state [Hyldegaard 2009a]. * It is estimated that the single-α determination in this branch is less reliable than the triple-α determination. Therefore the combined result is only from the latter.

4.4 Implantation experiment

The Hoyle state was not measured in the complete kinematics experiment at JYFL. This was due to energy loss in the stopping foil and detector dead layers. Another experiment has been performed at the KVI (Kernfysisch Versneller Instituut) in Groningen, The Netherlands, using implantation of the ^{12}N and ^{12}B nuclei inside a detector to avoid the energy losses and allow for detection of the Hoyle state. This also provides a direct measurement of the 3α sum spectrum independent of the geometry of the experimental setup and an independent measurement of the branching ratios.

4.4.1 Experimental method

Beams of ^{12}N and ^{12}B were produced using the same reactions as at JYFL, but in inverse kinematics. Primary beams of ^{12}C(^{11}B) were produced and accelerated to 22.7 MeV/u (18.3 MeV/u) before impinging on a gas target of hydrogen(deuterium). The secondary beams of ^{12}N and ^{12}B would then leave the target with energies of 16.8 MeV/u and 16.0 MeV/u respectively. The reaction products were separated using the fragment separator for the TRIμP facility [Berg 2006] (TRIμP is an abbreviation for Trapped Radioactive Isotopes: microlaboratories for fundamental Physics). This dual magnetic separator is

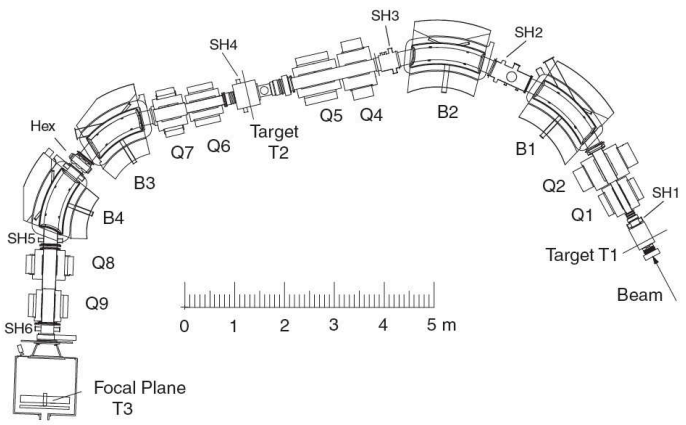

Figure 4.7: The TRIμP dual magnetic separator

shown schematically in figure 4.7. The magnet system consists of 4 bending dipoles ($B1$-$B4$), 8 quadrupole magnets ($Q1$-$Q9$)[1] and a hexapole for second order corrections. The beams are produced in the target $T1$ in the figure and the dispersion created by the dipoles B1 and B2 allows for the separation of isotopes with different rigidities, $B\rho = p/q$, where B is the magnetic field, ρ is the gyroradius of the particle due to this field, p is the particle momentum and q is its charge. Slit systems ($SH2$-$SH4$) stop the beam at various positions depending on its momentum dispersion, which is 3.9cm/% at $T2$. Different isotopes with the same rigidity can not be separated magnetically, so a degrader is inserted at $T2$. In this experiment the degrader was a 85 μm Si detector. Energy loss in the degrader depends on the charge and velocity ($\Delta E \propto Z^2/v^2$) so after the degrader different isotopes will have different rigidity. The beam is therefore efficiently separated after the last dipole, $B4$. Before reaching the detector setup after $Q9$ the beams were defocused to match the surface area of the detector.

The detector setup is shown in figure 4.8(a). The primary detector is a segmented 48×48 double-sided silicon strip detector (DSSSD) with a total active area of 16×16 mm^2. The strip pitch is 335 μm while the strip width is 300 μm [Smirnov 2005, Sellin 1992]. With a thickness of 78 μm, α particles from the decay of a nucleus implanted in the centre of the detector will deposit all of their energy inside the detector. β-particles from the decay will, on the con-

[1] $Q3$ was positioned between $B1$ and $B2$ in the first designs, but was finally omitted

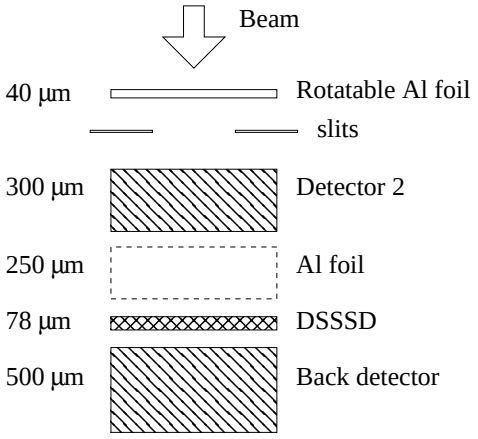

(a) Detector setup. The Al foil was removed when the beam changed to ^{12}N.

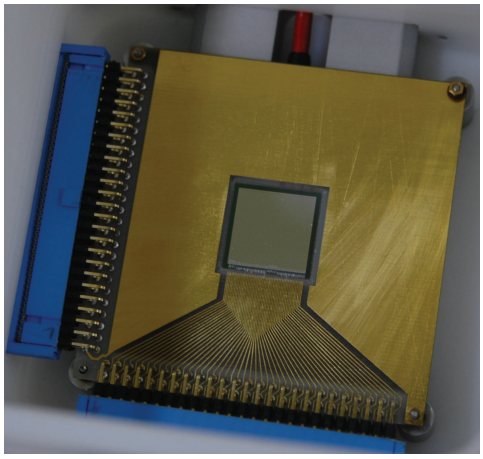

(b) The strip detector (DSSSD).

Figure 4.8: (a) A diagram of the detector setup shown from above. (b) The primary detector is a 48×48 double-sided silicon strip detector (DSSSD).

trary only deposit a small amount of energy in the detector (see section 4.4.4). The beam is defocused before reaching the detector setup to utilise the entire detector area and to avoid pile-up of events. Two different amplifications were used for the detection of implantation and decay events respectively. The high gain amplification for detection of decay events was sensitive to the 0-10 MeV energy region and the low gain amplification made it possible to detect implantations with energies up to 80 MeV. Calibration of the detector was performed using an offline source of ^{239}Pu, ^{241}Am and ^{244}Cm. These radioactive isotopes emit α particles in the 5-6 MeV energy region and the three strongest peaks in the spectrum have been used for the calibration. The resolution of the detector has been determined from the width of the calibration peaks to σ = 12 keV or FWHM = 28 keV for high-gain amplification.

The thick silicon detector in front of the DSSSD (detector 2 in figure 4.8(a)) and the aluminium foils work as degraders lowering the beam energy to implant it as close to the center of the DSSSD as possible. The ^{12}B beam is produced in a reaction with positive Q-value so more energy is available for kinetic energy of the ^{12}B beam than for the ^{12}N beam which is produced in a

reaction with negative Q-value. ^{12}B also has a smaller charge than ^{12}N and therefore lose less energy by ionisation in the degraders. More degraders are therefore needed to stop ^{12}B and the 250 μm Al foil was not used with the ^{12}N beam. The detector behind the DSSSD (Back detector in figure 4.8(a)) is used during tuning of the beam to see if it is stopped in the DSSSD and for the experiment it is used to detect β particles as identification of β-decay events in the DSSSD.

The production and separation of ^{12}N was first demonstrated in November 2005 using a simple setup with a 100 μm thick, unsegmented detector at the DSSSD position in figure 4.8(a). The purity of ^{12}N implanted in the detector was verified using a pulsed beam (50 ms beam on, 50 ms beam off) so only decay events were detected during beam off. The timing of the events relative to the start of beam on was registered and the decay time spectrum was consistent with the known half-life of ^{12}N. Evidence for the production of ^{12}N was also seen in the decay-energy spectrum showing the peak from the 12.71 MeV, 1^+ state at 5.4 MeV.

4.4.2 Electronics chain

The signals from the DSSSD strips and the thick Si detectors (detector 2 and the back detector), were sent to an electronics chain consisting of $2 \times 2 \times 48 = 192$ channels for the two different amplifications of each strip in the DSSSD plus three channels for the thick Si detectors. The signal from the DSSSD was sent to two 64-channel charge-sensitive preamplifiers (MPR-64) for the front and back strips respectively [mesytec 2010]. From the preamplifiers the signals were split for the DSSSD strips into two amplifier modules for amplification ranges relevant for implantation and decay identification respectively (see next section). The amplifiers were 16-channel amplifiers, STM-16, with channel shaper, timing filter and a discriminator, 6 amplifiers for high- and low-gain amplification respectively [mesytec 2010]. The amplifiers both amplify the signal from the preamplifier and also shape the signal to minimise tails of the pulse shape and optimise the signal-to-noise ratio. The discriminator in the module only accepts signals above a predefined voltage threshold to reduce low-energy electronic noise. The trigger is a logic OR between all 96 strip channels. Because the discriminator is of the leading-edge type the pulse

triggers an event when rising above the threshold level. When an event has triggered, the amplified energy signal is send to an Analog-to-Digital Converter (ADC). The ADCs are 32-channel V785 modules [CAEN 2010] converting the analog signal to a digital output which can be read out by the data acquisition system. These ADCs are of the peak-sensing type, determining the energy-proportional output as the amplitude of the pulse. The ADCs have a resolution of 12 bits corresponding to $2^{12} = 4096$ channels. A delayed trigger signal is send from the amplifier to a V1190A Time-to-Digital Converter (TDC) [CAEN 2010]. Once the TDC receives the trigger signal it reads out its output buffer with delayed timing output from the amplifier giving the time from the start of the event to the arrival of each detector pulse.

4.4.3 Implantation and decay data

A charged particle will produce a signal in a pixel of the detector corresponding to one front strip and one back strip. Energy matching between the front and back strips is applied as a condition for a physical signal to eliminate low energy noise. The energy matching condition depends on the resolution of the detector, but should not be too restrictive since all implantations and decays need to be detected to obtain the correct branching ratios. For the low-gain amplification (implantation events) the condition is $|E_{\text{front}} - E_{\text{back}}| < 4$ MeV and for the high-gain amplification (decay events) it is $|E_{\text{front}} - E_{\text{back}}| < 150$ keV. These are conservative values. For α particles the energy difference is within 50 keV for $\sim 90\%$ of the events.

Implanted ^{12}N and ^{12}B nuclei are identified by a signal in detector 2 in front of the DSSSD. To avoid any α particles from the breakups escaping the detector, it is a requirement that the nuclei are implanted in the center of the detector. Figure 4.9 shows the implantation spectra with the implantation depth corresponding to the deposited energy on the upper axes. The energy loss per range in the Si detector is calculated using SRIM for $^{12}B^{5+}$ and $^{12}N^{7+}$ ions respectively [SRIM 2006]. For both beams the majority of the ions are implanted close to the center of the detector as required, but the ^{12}B spectrum is seen to have a low-energy tail of nuclei deposited close to the surface, so a lower limit of 7 MeV is imposed on the implantation energy.

The halflives of ^{12}N and ^{12}B are 11.000(16) ms and 20.20(2) ms respectively.

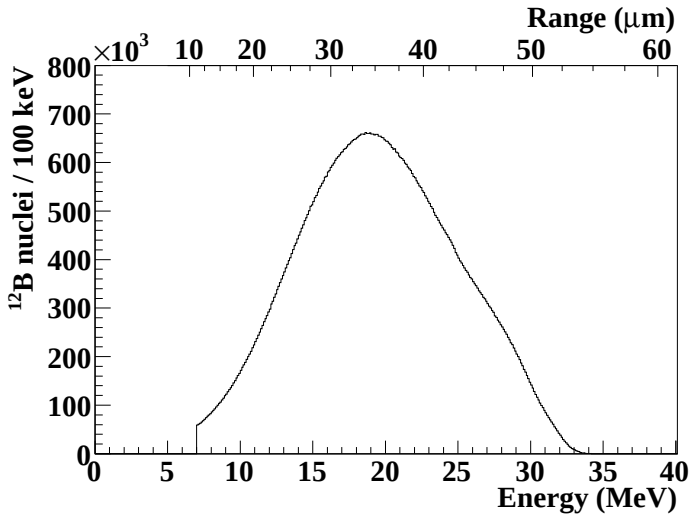

(a) ^{12}B implantations.

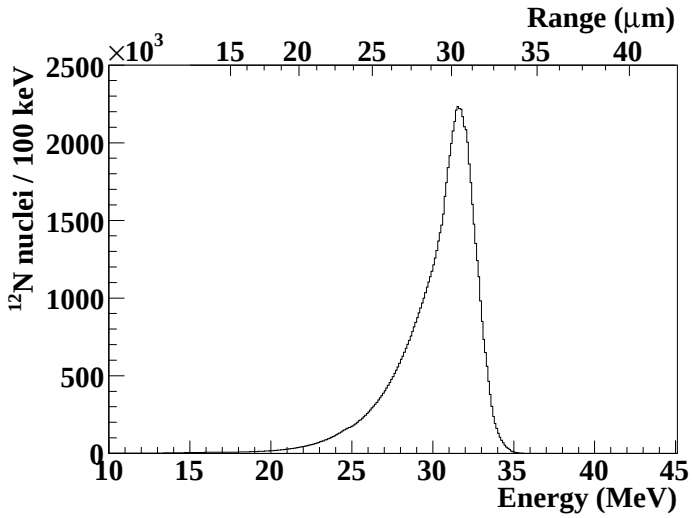

(b) ^{12}N implantations.

Figure 4.9: Implantation spectra showing the energy on the lower axis and the range calculated using SRIM on the upper axis.

For both isotopes 99% of the decays will have taken place within 200 ms after the implantation, and decay events are restricted by this time window.

The beam purity is essential for the interpretation of the data, and figure

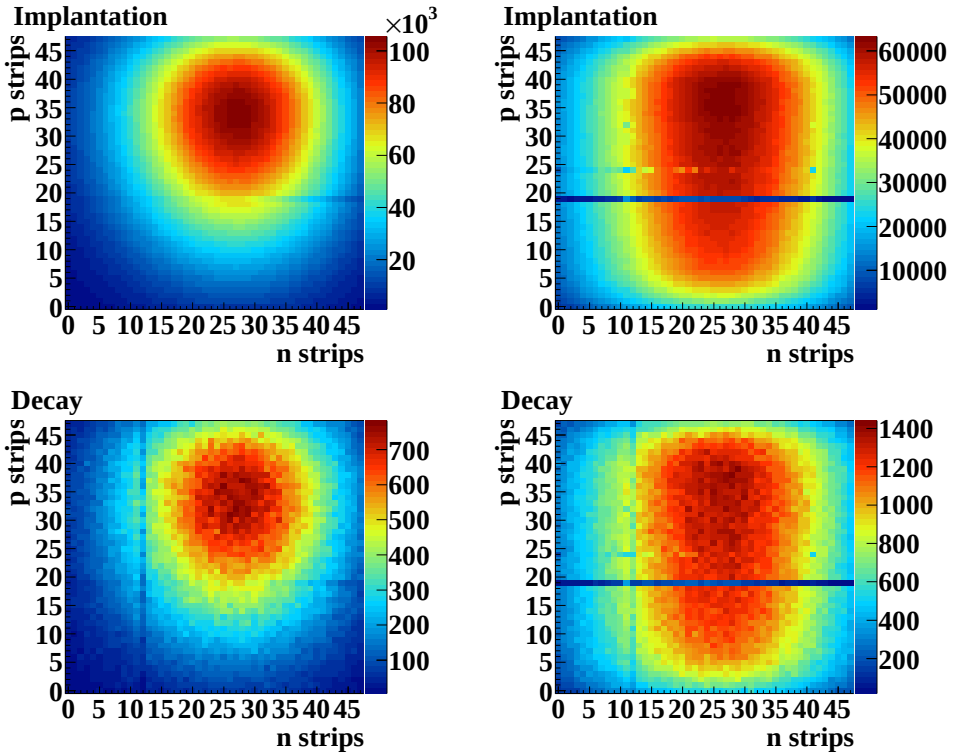

(a) ^{12}B implantation and decay.

(b) ^{12}N implantation and decay.

Figure 4.10: Implantation (top) and decay (bottom) profiles on the DSSSD.

4.10 supports this assumption. The upper graphs show the profiles of implantation events over the detector area, and the decay profiles below are seen to have the same shape, except for a few strips with lower efficiency at these energies. If there were more than one component in the beam, the implantations of the different components would not hit the same spot on the detector, and since their branching ratios would be different, the decay profile on the detector would be different from that for implantations.

To identify the implanted ions as ^{12}N and ^{12}B, one can fit the decay time spectra in figure 4.11 to deduce the half-lives. Fits within the ranges 0-100 ms for ^{12}B and 0-60 ms for ^{12}N give half-lives of 20.20(3) ms and 10.994(10) ms respectively, consistent with the literature values. The decay time spectra in figure 4.11 also show a slower component above 200 ms. The energy spectra

for times greater than 200 ms after an implantation reveal that this component is low energy noise, and as such, it will have an exponential distribution in the decay-time spectrum falling off depending on the implantation rate. The random noise event will on average come at half the time between two implantations, so the rate parameter is expected to be twice the implantation rate. The decay-time spectra have been fit to the sum of two exponential functions, as shown in figure 4.11, and the rate of the slow component is found to be 1.4(3) Hz and 0.85(8) Hz for ^{12}N and ^{12}B respectively. With $48 \times 48 = 2304$ pixels this corresponds to average implantation rates of 1.6(3) kHz (^{12}N) and 0.98(10) kHz (^{12}B). This can be compared to the average rates of registered implantations determined from the total number of implantations and the measurement time, giving 2 kHz (^{12}N) and 0.9 Hz (^{12}B). The good agreement between the average rates supports the interpretation of the slow component as random (noise) events uncorrelated with the implantations.

4.4.4 Beta response

The β-decay sum-energy spectra measured with implantation (KVI) and complete kinematics (JYFL) are compared in figure 4.12. The same features are seen in the spectra in the common energy region, but the KVI spectra hold more information due to the larger number of counts, especially above the 12.71 MeV peak for ^{12}N, and because it is sensitive to low energies, where the Hoyle peak is seen at 7.7 MeV. This comparison of the statistics in the two measurements is only approximate, because the JYFL spectra have been efficiency corrected, and the number of counts for the low-energy points is smaller than the value read off the axis, which is also reflected by the large spread in the data points. The KVI spectra differ from the JYFL 3α sum-spectra because of the small amount of energy deposited by electrons or positrons. For decays to bound states in ^{12}C this leads to the deposition of only β energy contributing to the low-energy peak below the Hoyle peak. For decays to states unstable to 3α breakup the β energy is added to the 3α sum energy, and this is seen as a shift of the spectra compared to the JYFL spectra, especially visible in the position of the 12.71 MeV peak. This peak is broader and has a low-energy tail in the JYFL spectra, which is caused by incomplete reconstruction of the energy loss in foil and detector dead layers for some events.

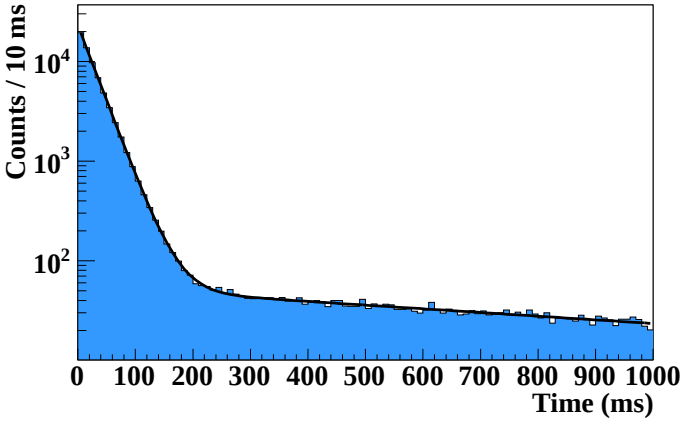

(a) ^{12}B decay time.

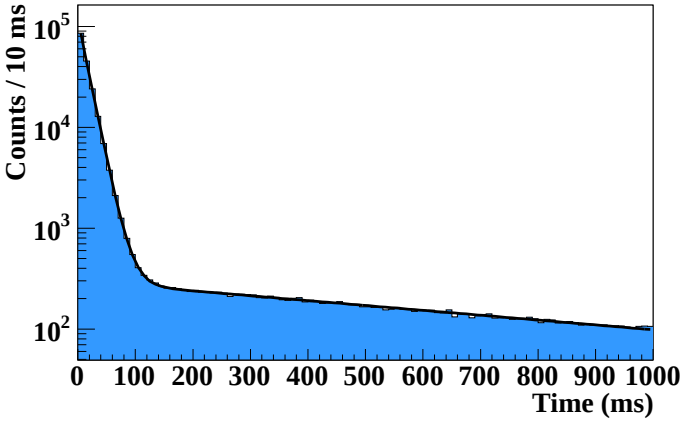

(b) ^{12}N decay time.

Figure 4.11: Decay time spectra for particle hits with $E > 0.33$ MeV. The sum of two decaying exponential functions fit the spectra.

The beta response has been simulated using a simple model assuming the β-particles travel in straight lines through a specified detector geometry. This assumption is in fact not valid, because the particles are scattered in the detector, but, imposing some variability in the range, it is possible to find a model which reproduces the shift of both the Hoyle peak and 12.71 MeV peak and the position of the low-energy beta peak.

For each excitation energy bin the beta response energy distribution is cal-

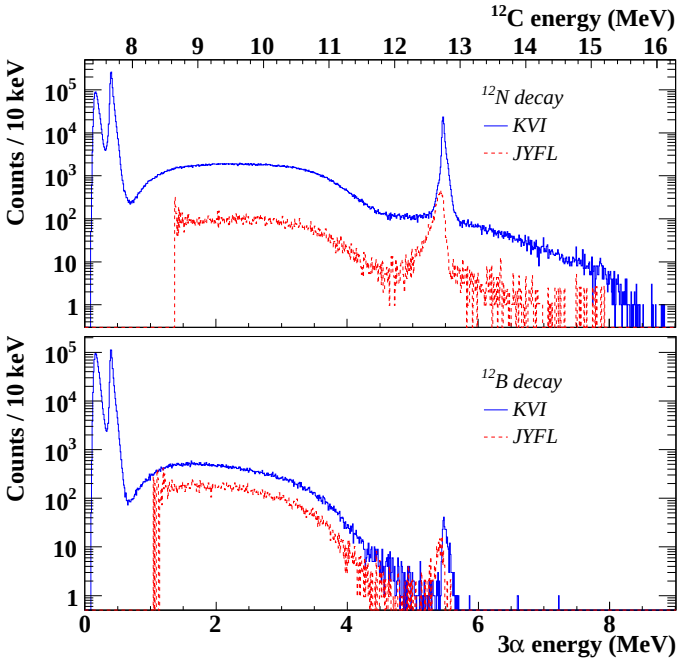

Figure 4.12: Sum-energy spectra for β decay of ^{12}N (top) and ^{12}B (bottom). The JYFL spectra are efficiency corrected.

culated. The implantations are assumed to be uniform over the detector area, and the depths are distributed according to figure 4.9. The β particles are emitted uniformly in 4π and travel through a rectangular box with thickness equal to the detector thickness and widths w_x and w_y. The β energy- distribution is given by formula 3.23, neglecting the recoil and radiative corrections, and the energy deposited in the detector is calculated using the Bethe-Bloch formula for energy loss by inelastic collision with atomic electrons. Radiation energy loss by Bremsstrahlung can be neglected at these energies, since the characteristic energy for $(dE/dx)_{\text{rad}} = (dE/dx)_{\text{coll}}$ is 58 MeV for silicon.

The simulated beta response distributions for decay to the 3α continuum are shown in figure 4.13. For each 3α energy bin, 10000 events are simulated. Up to a few MeV from the maximum 3α energy the distributions are almost unchanged with 3α energy, peaking at about 20 keV. Upon close inspection two peaks are actually seen, somewhat broader for ^{12}B than ^{12}N. This artefact is caused by the range distribution of the beta particles having two peaks, corresponding to particles escaping via the front and back side of the detector

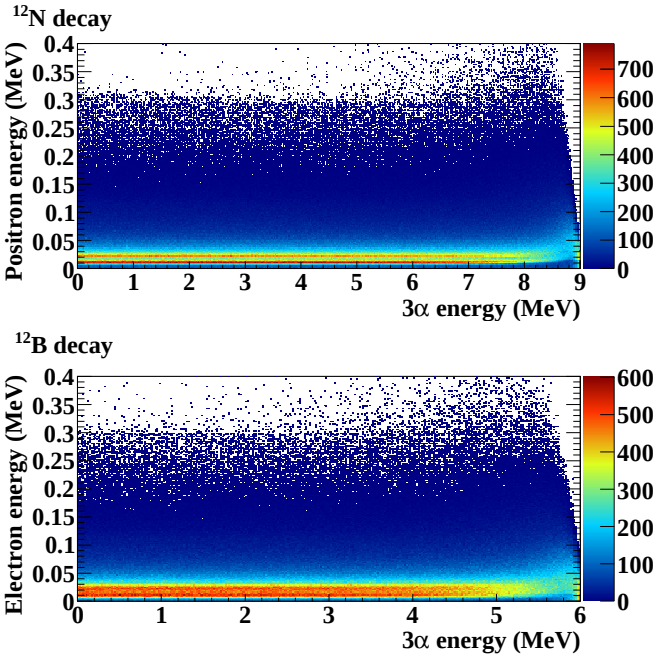

Figure 4.13: Beta response as a function of 3α energy for ^{12}N β^+ decay (top) and ^{12}B β^- decay (bottom).

respectively, and the peaks are broader for ^{12}B due to the larger spread in implantation depth (see figure 4.9). Close to the maximum 3α energy the lepton energy decreases and because the stopping power is larger for slow charged particles, more energy is deposited in the detector.

To test if the beta response can explain the energy shift in the implantation data, the decay spectrum has been simulated by adding the beta energy to a theoretical 3α energy distribution, where the broad components in the spectrum are given by a parametrisation and the Hoyle and 12.71 MeV peaks are delta functions at their respective energies broadened by the detector resolution. Both the 3α and β energies are generated by Monte Carlo sampling. The simulations are shown in figure 4.14, where they are seen to reproduce the main features, such as the position of the two narrow states and the low energy beta peak. The two peaks in the β energy-distribution are hidden in the spectra by the detector resolution. The agreement is not complete as seen from the tails of the peaks, but it is acceptable for our purpose.

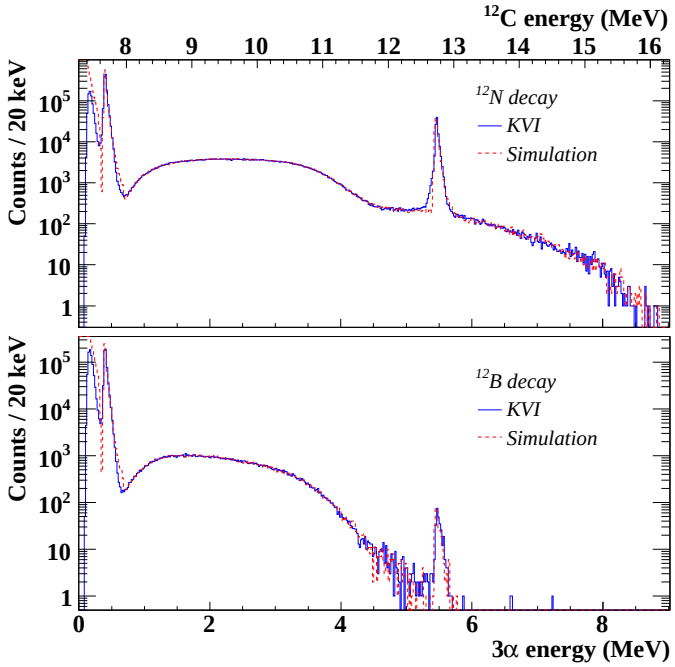

Figure 4.14: ^{12}N (top) and ^{12}B (bottom) decay spectra from the implantation experiment (KVI) compared to a simulated spectrum with beta response.

4.4.5 Low energy efficiency

For each DSSSD strip the trigger efficiency at low energy is reduced due to the low-energy thresholds of the dicriminator and ADC. The energy dependent efficiency below 1 MeV was determined using a pulser signal on each of the 96 high-gain electronics channels, 16 channels at a time. Seven different settings on the pulser were used and measured for one minute each. To obtain the efficiency of a certain channel it is required that the channel itself triggered the event. Figure 4.15(a) shows the efficiency of each of the 96 channels determined from the ADC spectra coincident with a signal in the TDC. A parametrisation of the trigger efficiency has been obtained from the pulser peak area as a function of energy.

Due to a problem with the trigger to the TDC, some events are shifted in the TDC compared to the ADC, so signals from the same event are not seen in coincidence. The TDC output buffer is large enough to store 32000 events

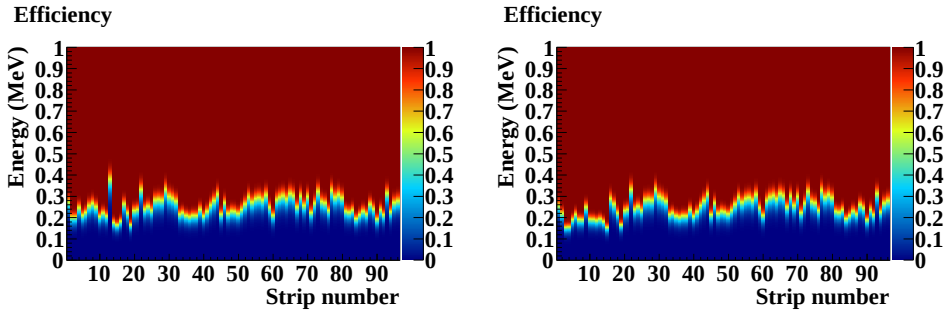

(a) (b)

Figure 4.15: Trigger efficiency calibrations from ADC spectra with a trigger in the TDC (a) and TDC triggers only (b).

before writing them to the data acquisition system, so reconstruction of events should in principle be possible. This has not been possible though, because in some parts of the files, more than 1000 TDC events appear between true events with an ADC signal, and these can not be attributed to just a shift between the ADC and TDC signals. It is not clear what causes this effect.

The problem with the TDC implies that it is unknown which channel triggered the event, and the realiability of the efficiency calibration in figure 4.15(a) is questionable. Figure 4.15(b) shows an alternative efficiency calibration using only the TDC signals. The number of signals for one pulser setting has been determined by integrating the TDC signals in the corresponding time interval. Simultaneous with the pulser signals, α sources were measured for the energy calibration, and this gives a small background contribution to the integrated pulser signal, but this bachground is approximately constant. The two efficiency calibrations in figure 4.15 are very similar, even though 100% efficiency in figure 4.15(b) corresponds to twice the number of counts as in figure 4.15(a). The average efficiencies are shown in figure 4.16, and for both calibrations the efficiency is better than 99% above 0.38 MeV.

Figure 4.17 shows the effect of efficiency correction on the ^{12}N spectrum. Events where the efficiency is below 1% in either front or back strip have not been corrected. The efficiency correction does not affect the Hoyle peak at 0.4 MeV 3α energy.

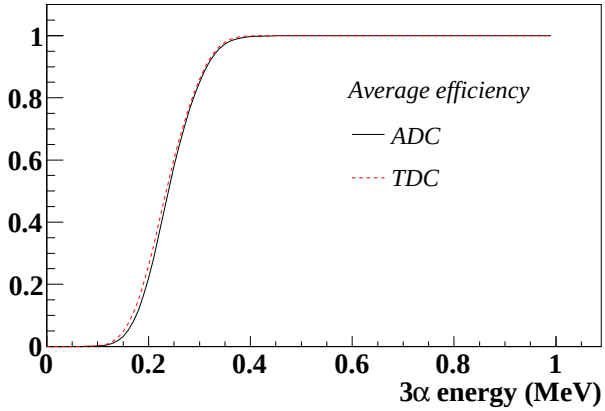

Figure 4.16: Average efficiency of all 96 strips from the calibrations in figure 4.15(a) (solid line) and 4.15(b) (dashed line).

A pulser signal is not identical to a physical signal from particle detection, so an alternative efficiency calibration has been performed using a Gd α source with air in the detector chamber at pressures between $\sim$ 100 mbar to atmospheric pressure providing α peaks between zero and one MeV. The α peaks are broadened due to straggling up to a FWHM of 0.15 MeV, so the deduced efficiencies vary more slowly. The α efficiency of each strip is illustrated in figure 4.18(a). These measurements were performed during a later run in december 2007 with the same setup, and true coincidences between ADC and TDC channels were obtained. A pulser calibration was also performed during the same run and it is shown in figure 4.18(b). The average efficiencies are shown in figure 4.19, and both calibrations confirm, that the Hoyle peak energy region is not affected.

The threshold settings in the 2006 and 2007 experiments were not exactly the same giving the slightly larger efficiency at low energies in the 2007 run. Decay of ^{12}N was also measured in 2007 to see the effect on the Hoyle peak, and the spectra are compared in figure 4.20. The dashed line is the 2006 spectrum and the filled area the spectrum from 2007. To compare the shapes the 2007 data have been scaled to the amount of counts in the 2006 spectrum and shown as the graph with statistical error bars. The two data sets are seen to be consistent within the uncertainty. The 2007 data contain more low-energy noise due to the lower thresholds.

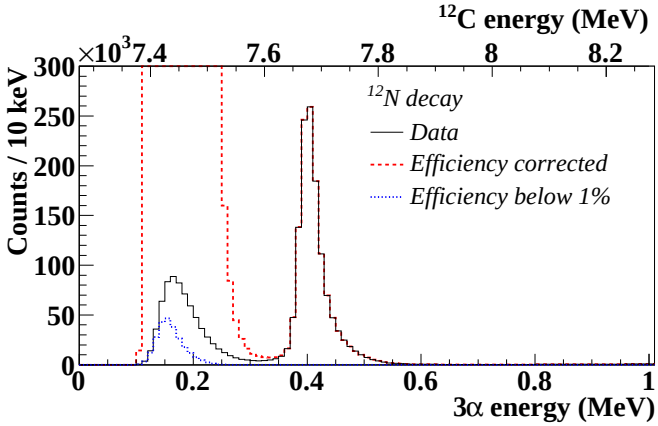

Figure 4.17: Low-energy ^{12}N decay spectrum. The soild line is the uncorrected data spectrum and the dashed line is the efficiency corrected spectrum using the calibration in figure 4.15(b). The dotted line is events for which the efficiency is below 1% and these have not been efficiency corrected.

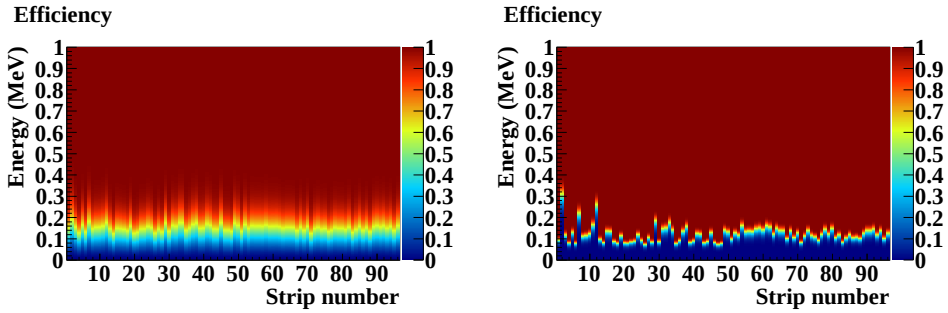

(a) (b)

Figure 4.18: Trigger efficiency calibrations from the 2007 run using α-particle (a) and pulser (b) signals.

4.5 Branching ratios

In this section, model independent branching ratios for β decay of ^{12}N and ^{12}B will be presented. The branching ratios to the broad components will be determined simply by integrating different energy regions, and this will facilitate comparison to previous branching ratio measurements. The precise composition of the broad components is still uncertain after the full R-matrix

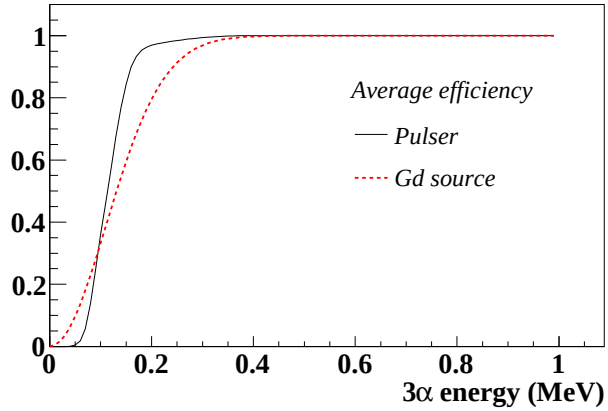

Figure 4.19: Average efficiency of all 96 strips from the calibrations in figure 4.18(a) (dashed line) and 4.18(b) (solid line).

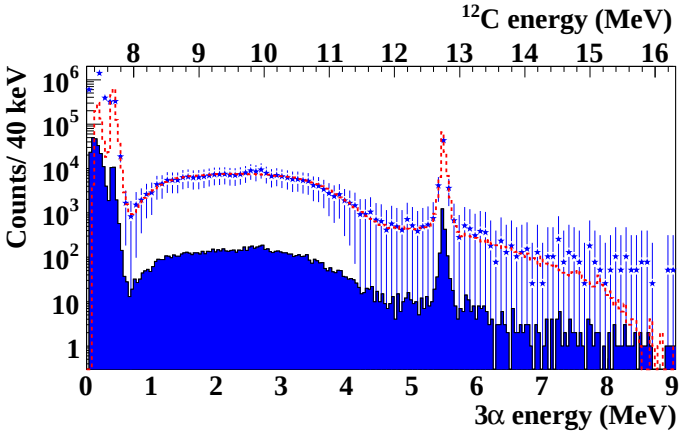

Figure 4.20: ^{12}N decay spectrum from implantation experiments at KVI in 2006 (dashed red line) and 2007 (filled spectrum). The 2007 data has been scaled to the same number of counts as the 2006 measurement for comparison (graph with error bars).

analysis presented in section 4.6, and for interfering broad states it is not obvious how to determine the branching ratios to the individual states. For such states the branching ratio is not a useful quantity, instead it is recommended to refer to matrix elements or B_{GT} values.

The relative branching ratios from the analysis of the triple-α and single-α JYFL data are brought to an absolute scale using the measured γ data and well

known decay branch to the 4.44 MeV particle-bound state in ^{12}C. The branching ratios to this state are 1.898(32)% for ^{12}N and 1.283(40)% for ^{12}B [Ajzenberg-Selove 1990]. An alternative value of 1.182(19)% for ^{12}B is given in [Ajzenberg-Selove 1990] but it has not been used in this evaluation. During most of the experiment only the DSSSDs were included in the trigger, providing the α data shown in figures 4.4 and 4.5. For the absolute normalisation, the thick back detectors behind the DSSSDs, registering only β particles from the decays, are used as trigger. The total number of detected γ-rays from the 4.44 MeV state is then

$$N_\gamma = \mathrm{BR}_\gamma N(^{12}\mathrm{N}/^{12}\mathrm{B})\varepsilon_\gamma\varepsilon_\beta, \tag{4.7}$$

where BR_γ is the branching ratio to the 4.44 MeV state, N is the number of decaying nuclei, ε_γ is the γ efficiency (see section 4.2.2) and ε_β the back detector efficiency. The total number of 3α breakups from an excited state in ^{12}C detected in the DSSSDs and triggered by the back detector is

$$N_\alpha = \mathrm{BR}_\alpha \frac{\Gamma_\alpha}{\Gamma} N(^{12}\mathrm{N}/^{12}\mathrm{B})\varepsilon_\alpha\varepsilon_\beta, \tag{4.8}$$

where BR_α is the branching ratio, Γ_α/Γ the relative α width and ε_α the assumed constant detection efficiency of the DSSSD. The absolute branching ratio to the α-emitting state can be found by combining equations 4.7 and 4.8:

$$\mathrm{BR}_\alpha = \mathrm{BR}_\gamma \frac{N_\alpha}{N_\gamma}\frac{\varepsilon_\gamma}{\varepsilon_\alpha}\frac{\Gamma}{\Gamma_\alpha}. \tag{4.9}$$

The γ-energy spectra are shown in figure 4.21. In both spectra the 4.44 MeV γ peak is seen as well as the single- and double-escape peaks. Other dominant peaks are the 511 keV annihilation peak and the 1460 keV peak from ^{40}K background radiation. Also visible are the Compton continuum and a significant background of bremsstrahlung, especially prominent in the ^{12}B spectrum.

The branching ratio to the $9 - 16.3$ MeV region is used for normalisation and N_α is extracted from the single-α spectra for events triggered by a back detector. The results are $\mathrm{BR}_\alpha(^{12}\mathrm{B}) = 0.060(7)\%$ and $\mathrm{BR}_\alpha(^{12}\mathrm{N}) = 0.50(6)\%$ ($9 - 16.3$ MeV region). From this the relative branching ratios in table 4.1 are brought to an absolute scale and are presented in table 4.2.

The KVI spectra are easily brought to an absolute scale by division with the number of implantations. The KVI and JYFL spectra normalised to branching

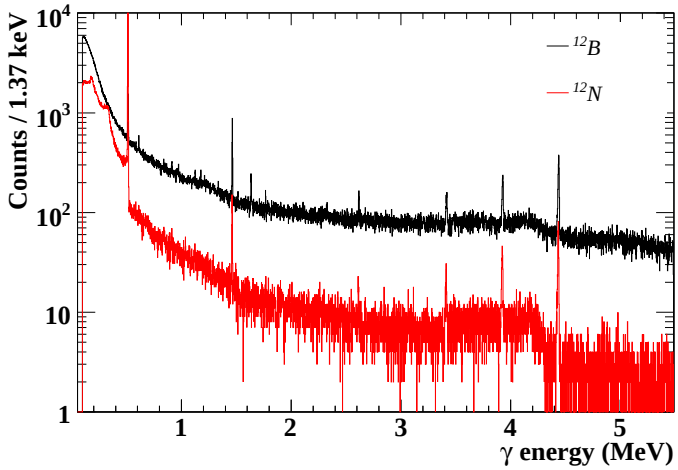

Figure 4.21: γ-ray spectra for ^{12}B and ^{12}N decay.

ratio per energy bin are shown in figure 4.22. Also shown are simulated JYFL spectra modified by the beta response in the KVI experiment. The two data sets are in good agreement within the uncertainties, and the energy shift due to beta response is nicely reproduced. The KVI branching ratios are found by integrating the spectra in figure 4.22. The small exponential tail of the beta peak is subtracted from the Hoyle peak and a linear background is subtracted from the 12.71 MeV peak.

Branching ratios from the two experiments are given in table 4.2, where they are also compared to literature values. Several of the literature values have been updated from the values tabulated in [Ajzenberg-Selove 1990] by renormalising to the 4.44 MeV state using updated values for the branching ratio to this state. In this work the value BR(4.44) = 1.283(40)% has been used of the two alternative values given in [Ajzenberg-Selove 1990]. The branching ratios to the ground state are found as one minus the sum of branching ratios to all excited states. The branching ratios for the KVI experiment in table 4.2 are a few percent smaller for the unbound states in [Hyldegaard 2009b] due to the erroneous interpretation of the slow component in figure 4.11 as decay events following an implantation event which was not detected.

Comparing the JYFL and KVI branching ratios, the results agree within the uncertainty as one would also expect from figure 4.22.

The branching ratios to the Hoyle state are only from the KVI experiment,

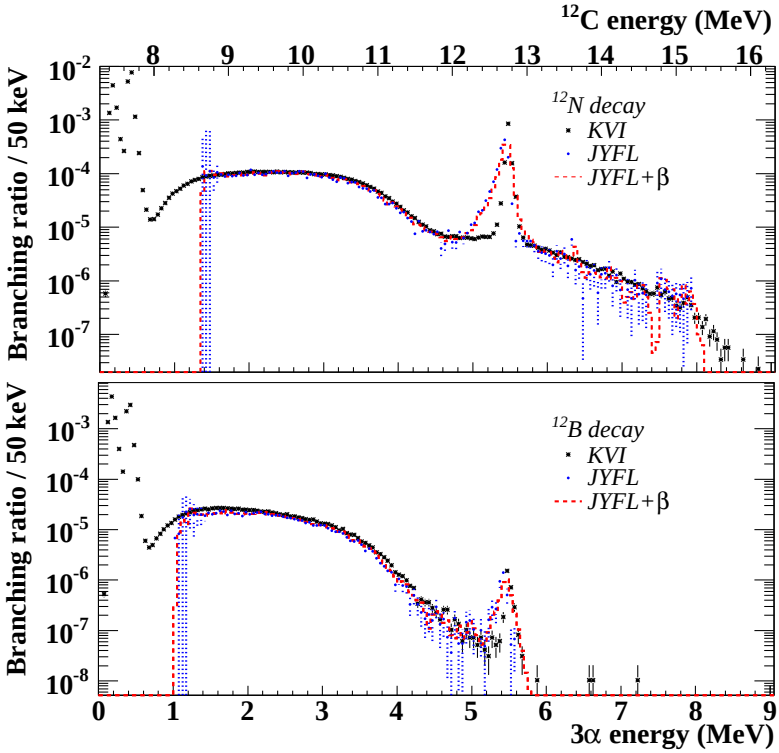

Figure 4.22: Spectra for ^{12}N decay (top) and ^{12}B decay (bottom) scaled to absolute branching ratios per energy bin with error bars. The black markers with solid line, statistical error bars are KVI data, the blue squares with dotted error bars (both statistical and from efficiency uncertainty) are the JYFL data, and the red, dashed curves are simulations of the JYFL data with beta response.

and they are only half the literature values, but are determined to much better precision. The ^{12}B branching ratio in [Ajzenberg-Selove 1990] is the combination of two experimental values, 1.3(4)% [Cook 1957] and 1.5(7)% [Alburger 1963]. The latter can be updated by renormalisation using the updated BR(4.44) and $\Gamma_\gamma(3.22)/\Gamma = 4.13(11) \cdot 10^{-4}$ to 1.2(4)%. In the first measurement, single α particles were measured with a magnetic spectrometer, and the obtained branching ratio of 1.3(4)% depends on the assumption that the absolute normalisation is correct [Cook 1957]. The number of created ^{12}B nuclei were not directly measured. The second measurement by Alburger [Alburger 1963] was a β-γ-γ coincidence measurement detecting electrons from ^{12}B β decay in coincidence with 3.22 MeV and 4.44 MeV γ rays from the sequential de-

^{12}C	^{12}N			^{12}B		
Energy (MeV)	Lit. %	JYFL %	KVI %	Lit. %	JYFL %	KVI %
g.s.	94.6(6)*	-	95.96(5)	97.4(3)*	-	98.02(4)
4.44	1.90(3)	-	-	1.28(4)	-	-
7.65	2.7(4)	-	1.44(3)	1.2(3)*	-	0.59(2)
7.9 – 12	-	-	0.548(2)	-	-	0.108(3)
9 – 12	0.46(15)	0.38(5)	0.416(9)	0.08(2)	0.060(7)	0.070(3)
12.7	0.28(8)*	0.11(2)	0.123(3)	-	$3.5(7)\cdot10^{-4}$	$2.8(2)\cdot10^{-4}$
12 – 16.3	-	0.021(6)	0.020(3)	-	-	-
15.11	$3.8(8)\cdot10^{-3}$*	-	$3.2(10)\cdot10^{-5}\Gamma/\Gamma_\alpha$	-	-	-
7.3 – 16.3	3.4(4)	-	2.11(3)	1.3(3)	-	0.69(2)

Table 4.2: Branching ratios to ^{12}C from complete kinematics (JYFL) and implantation (KVI) experiments. Literature values for comparison are from [Ajzenberg-Selove 1990]. * Updated literature value (see the text).

excitation of the 7.65 MeV state. The detector setup consisted of two NaI γ detectors and a scintillator β detector. The resolution in the NaI detectors is very low and the peak to Compton ratio is rather small. Furthermore, the β-γ-γ coincidence spectrum is significantly affected by bremsstrahlung, and the branching ratio relies on correct background subtraction. It is of interest to perform a similar experiment using Ge-detectors with a much better resolution and peak to Compton ratio.

For ^{12}N decay the branching ratio to the Hoyle state derives from Kurie-plot analyses of two experimental measurements of the β spectrum [Mayer-Kuckuk 1962, Glass 1963]. In the first experiment the absolute β spectrum was measured and the Hoyle-state branch determined after first extracting the ground state and 4.44 MeV state β spectra from their end points [Mayer-Kuckuk 1962]. The Hoyle-state branch of 3.0(4)% therefore depends on assumptions on the β spectrum shape and the branching ratio to the 4.44 MeV state, which was known to be 2.4(2)% at the time. Due to the extrapolation errors inherent in the method, the claimed 13% uncertainty on the third branch

seems underestimated. In the second experiment the relative β spectra normalised to the same end point were measured [Glass 1963]. The resulting ^{12}N branching ratios were determined by constraining the previously measured ^{12}B branching ratios to 1.3(4)% for the 7.65 MeV state and 0.13(4)% for the 10.1 MeV state. For both the analysis in [Mayer-Kuckuk 1962] and [Glass 1963] it is assumed that the next excited state above the 7.65 MeV state is at 10.1 MeV giving an end point energy 2.5 MeV below the end point for the 7.65 MeV state. From figure 4.22 this assumption is now known to be invalid, since the broad component is significant already at 0.5 MeV above the peak, and this will lead to overestimated branching ratios to the 7.65 MeV state from the Kurie plot analyses.

In the literature, the broad component between the 7.65 and 12.71 MeV peaks is denoted a 10.3 MeV state with $\Gamma^o = 3$ MeV. These assignments are questionable [Diget 2005] and the structure of this component will be analysed in detail in section 4.6. When the branching ratios to this state were first measured, the 12.71 MeV state was not known, and the branching ratio for ^{12}N decay, determined from the single-α spectrum, is overestimated in [Wilkinson 1963]. For both ^{12}N and ^{12}B the values from the evaluation in [Ajzenberg-Selove 1990] are dominated by the same work [Wilkinson 1963]. The given branching ratios of 0.44(15)% for ^{12}N and 0.07(2)% for ^{12}B corresponds to integrated single-α spectra from 9 to 12 MeV excitation energy, comparable to branching ratios from 3α spectra to the same region plus about two times the branching ratio to the 12.71 MeV peak (see figure 4.5). The branching ratio for ^{12}B agrees well with the new results and the value for ^{12}N is also consistent within 2σ, but somewhat underestimated when accounting for the contribution from the 12.71 MeV state. An other measurement of the branching ratio for ^{12}B found the value 0.13(4)% [Cook 1958]. The larger value is reasonable because it includes the energy region below 9 MeV, in good agreement with the branching ratio for the 7.9 to 12 MeV region from the KVI data.

The 12.71 MeV peak was measured with ^{12}B decay for the first time in the JYFL experment. In [Schwalm 1966] an upper limit for the ratio between β decays to the 12.71 MeV peak and the 10.3 MeV state is given as $3 \cdot 10^{-2}$, slightly smaller than the JYFL and KVI values. The evaluated branching ratios to the 12.71 MeV state and 15.11 MeV state for ^{12}N are dominated by the same ex-

periment [Alburger 1967], and these are updated using BR(4.44) = 1.898(32)%, $\Gamma_\gamma(12.71)/\Gamma = 1.93(12) \cdot 10^{-2}$ and $\Gamma_\gamma(15.11)/\Gamma = 0.88(3)$. The new result for the 12.71 MeV branching ratio for ^{12}N is marginally consistent with this updated value, but is a factor of ten more precise. Support for a lower value comes from the value of 0.20(5) for the ratio of the ^{12}N branching ratios to the 12.71 MeV state and the 10.3 MeV strength [Schwalm 1966]. A larger branching ratio to the 12.71 MeV peak would also be inconsistent with the branching ratio to the 9-12 MeV region from [Wilkinson 1963] discussed above.

The branching ratio to the broad region at high energies in the excitation energy spectrum (with the 12.71 MeV peak subtracted) has not previously been measured. The isobaric analogue state at 15.11 MeV has a small α branch, $\Gamma_\alpha/\Gamma = 0.041(9)$ [Balamuth 1974], and is seen as a small peak in the ^{12}N decay spectrum with 29(9) counts. Assuming a negligible GT strength (B_{GT} value) to this state, the corresponding branching ratio leads to a Fermi strength of 0.6(2), which is inconsistent with the expected value $B_F = 2$. Accepting the theoretical Fermi strength leads to a revised value for the α width, $\Gamma_\alpha/\Gamma = 0.011(3)$, which is consistent with the value 0.012(7) in [Reisman 1970].

4.5.1 B_{GT} values to narrow states

For narrow states, λ, B_{GT} values are determined from the branching ratios, BR_λ, as

$$B_{\mathrm{GT}} = \frac{g_V^2}{g_A^2}\frac{B}{f_\beta t_{1/2;\lambda}} = \frac{g_V^2}{g_A^2}\frac{B}{f_\beta t_{1/2}}\mathrm{BR}_\lambda. \tag{4.10}$$

Values are given in table 4.3. For the broad regions B_{GT} values can not be found from the branching ratios in table 4.2, since f_β is energy dependent. The B_{GT} values to the broad states will instead be extracted from R-matrix parameters obtained by fitting the data (see the discussion in section 2.5.5 on ft and B_{GT} values to broad states).

The isospin asymmetry is defined as $\delta = ft(\beta^+)/ft(\beta^-) - 1$ and values are given in table 4.3. Isospin is a good quantum number if $\delta = 0$ corresponding to equal strengths for β^+ and β^- transitions. The isospin asymmetry per energy bin is given in figure 4.23 along with the inverse ft values for the β^+ and β^- decays respectively. δ is seen to vary most in areas where the spectra change rapidly. These variations are mainly caused by differences in the amount of

^{12}C Energy (MeV)	B_{GT} ^{12}N	B_{GT} ^{12}B	$\delta = \frac{B_{GT}(^{12}B)}{B_{GT}(^{12}N)} - 1$
g.s.	0.2950(14)	0.331(2)	0.121(2)
4.44	0.0270(4)	0.0297(9)	0.10(4)
7.65	0.093(2)	0.110(3)	0.19(4)
12.7	0.462(12)	0.51(3)	0.10(8)

Table 4.3: B_{GT} values to narrow states in ^{12}C from the implantation experiment at KVI. Values for the 4.44 MeV state are from the literature, but are included here for completeness.

β summing in the two decays due to different Q-values in the two decays. A small constant positive shift is seen in favor of β^- decay in figure 4.23 as well as for the narrow peaks in table 4.3. The energy independence confirms that the origin of the asymmetry is mainly nuclear structure [Wilkinson 2000, Wilkinson 1971] as a second-class-currents explanation infers an energy dependent asymmetry [Wilkinson 2000].

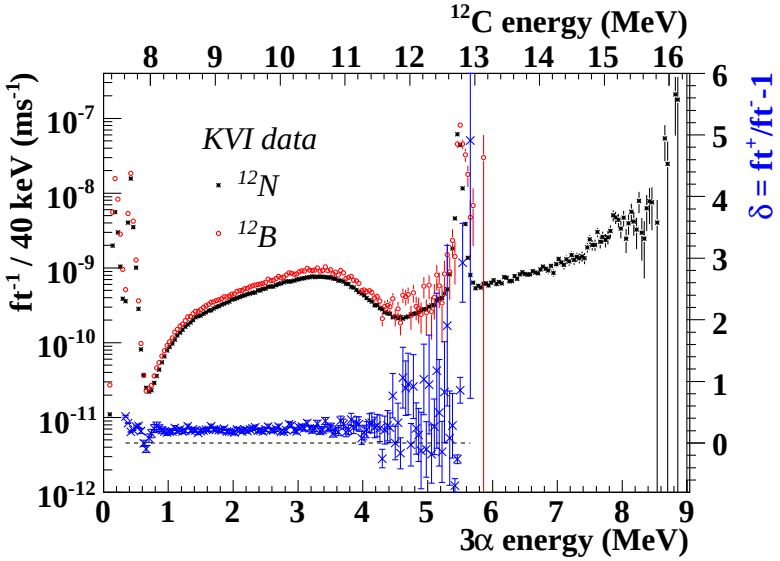

Figure 4.23: Spectra of inverse ft value per energy bin for ^{12}N and ^{12}B decays (left ordinate). The isospin asymmetry, δ, is also shown (right ordinate).

4.6 *R*-matrix analysis

The β-decay data has been analysed by performing a simultaneous *R*-matrix fit to the KVI data for ^{12}N and ^{12}B and the sum-energy spectra from JYFL for decay via the ground-state peak in ^{8}Be and excited states respectively, also for both ^{12}N and ^{12}B [Hyldegaard 2010]. The formalism for sequential decay via broad states, presented in section 2.6, has been applied. Results from a separate *R*-matrix analysis of the breakup kinematics in the JYFL data are used to constrain the fit model [Diget 2009].

4.6.1 Implementation

The function to minimise is the sum of a log-likelihood function for the KVI data,

$$\chi^2 = 2\sum_i \left(n_{i,fit} - n_{i,data} + n_{i,data} \ln\left(\frac{n_{i,data}}{n_{i,fit}}\right)\right), \tag{4.11}$$

and a least-squares minimisation for the efficiency-corrected JYFL data, as the JYFL data are not Poisson distributed after efficiency correction,

$$\chi^2 = \left(\frac{n_{i,fit} - n_{i,data}}{\sigma_i}\right)^2. \tag{4.12}$$

The uncertainty, σ, is the combination of the uncertainty of the efficiency correction and the statistical uncertainty from the number of counts in the spectrum. The 1^+ peak at 12.71 MeV is excluded and the upper fit limit is just below the 15.11 MeV peak. The Hoyle peak is included with its area only, as its shape is strongly affected by the β response. The area is calculated using the single-level, narrow-state approximation of equation 2.96. The width and energy of the Hoyle state are kept fixed at $\Gamma_H = 7.65 \cdot 10^{-6}$ MeV and $E_H = S_{3\alpha} + 0.3794$ MeV [Ajzenberg-Selove 1990], respectively.

The *R*-matrix parameters for the ^{8}Be ground state are found from the energy and observed width tabulated in [Tilley 2004]. The 2^+ excited-state parameters are from [Bhattacharya 2006] (Table II, column 3), and the channel radius used is 4.5 fm. Using these parameters the resonance forms, $\rho_{\lambda' c'}$, for the ground state and first excited states are calculated. These are shown in figure 4.24, where it is clearly seen, that the ^{8}Be ground state, only 91.8 keV above

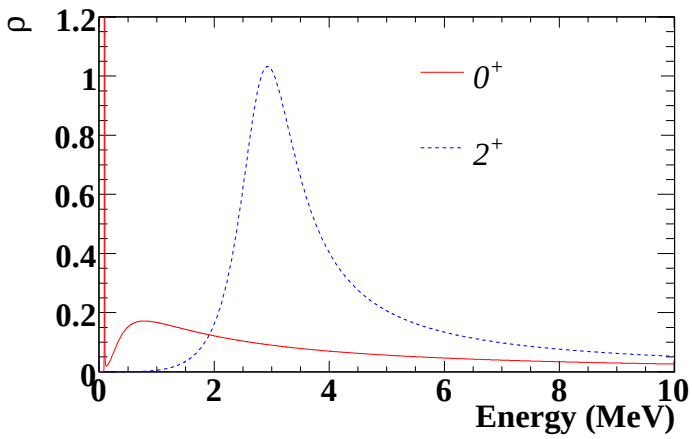

Figure 4.24: The ^{8}Be ground state and lowest 2^+ state in the single-level R-matrix model.

the 2α threshold, has a prominent ghost. The integration ranges used for the shift and penetration functions (equations 2.107 and 2.108) are 0 - 5 MeV for the ground state and 0 - 10 MeV for the 2^+ state, chosen so that the 0^+_1 and 2^+_1 states are the dominating states in their respective integration intervals. Infinity is not chosen as the upper integration limit because other 0^+ and 2^+ channels dominate at higher energy.

The alternative R-matrix parametrisation has been used in this work, providing the observables directly from the fit. To save computation time, the shift and penetration functions are calculated once for each energy bin, and only the shift functions $S_c(\tilde{E}_i)$ have to be re-calculated when the resonance energies, $\tilde{E}_i$ are varied.

The β response in the KVI data is taken into account by folding the calculated spectra with the simulated β-response functions before comparison to the KVI data. This has to be done at each step in the fitting routine before calculating χ^2. The uncertainty in the simulated β response is not taken into account, but in a reasonable assumption it is energy independent and the only effect of this neglect is to weight the KVI data slightly higher than appropriate in the fit.

The number of free parameters in the fit depends on the number of levels included. Each level is defined by a level energy, E_λ, β strengths, $g(^{12}\mathrm{N}/^{12}\mathrm{B})$, and reduced widths, $\gamma_{\lambda j_b l}$, where j_b is the spin of the ^{8}Be state and l the angular

momentum in the breakup of ^{12}C. The only 1^+ states below the ^{12}N Q-value are the narrow 12.71- and 15.11-MeV states, so the levels entering the fits must be either 0^+ or 2^+. This was verified by the separate analysis of the JYFL data, showing no evidence for additional 1^+ components [Diget 2009], which is as expected since a 1^+ state would be narrow [Fedorov 2003]. For the 0^+ states there are two possible breakup channels: $l = 0$, $j_b = 0$ and $l = 2$, $j_b = 2$. For 2^+ states in ^{12}C there are four possibilities: $j_b = 0$, $l = 2$ and $j_b = 2$, $l = 0, 2, 4$. The $l = 4$ channel is not considered here, because its only appreciable contribution would be at the very high-energy end of the ^{12}N spectrum [Diget 2009]. The channel radius is kept fixed in the fits at a value common for all states, $a = r_0(8^{1/3} + 4^{1/3})$. A first choice for r_0 is 1.71 fm, as in [Diget 2006]. This is a large value compared to typical applications of R-matrix theory but is physically motivated by the large extension of the Hoyle state.

4.6.2 Analysis

The analysis proceeds by testing increasingly more complex models of the triple-α continuum. The starting point is what is already known to be there: The Hoyle state at 7.654 MeV in ^{12}C or just 0.3794 MeV above the 3α threshold. It is also known from the separate analysis of the JYFL data presented in [Diget 2009], that the broad components in the spectrum arise from some combination of 0^+ and 2^+ states and are dominated by 0^+ below the 12.71 MeV peak and by 2^+ above it.

It is relevant at this point to look at the spectra for a qualitative assessment of their expected composition. From figure 4.23 it is seen that the broad components increase in strength with increasing energy. The broad component above the Hoyle peak has its maximum at 10.5 MeV, and it is evident that it consists of more than the Hoyle state ghost, as was already shown in [Wilkinson 1963]. Above the 12.71 MeV peak the ^{12}N spectrum continuously increases up to the Q-value. One would expect at least one resonance in this region or at higher energy.

In table 4.4 the nine different models considered are listed with their combination of 0^+ and 2^+ states, reduced χ^2 value, channel radius and the figures illustrating the respective fits. A discussion of each of these will follow next.

Model	χ^2/df	r_0 (fm)	Fig. no.(s.)
1: 0+	281	1.71	4.25, 4.26
2: 0+, 0+	15.9	1.71	4.25, 4.26
3: 0+, 2+	44.8	1.71	4.25, 4.26
4: 0+, 0+, 0+	3.24	1.71	4.25, 4.26
5: 0+, 0+, 2+	6.06	2.09	4.25, 4.26
6: 0+, 2+, 2+	18.4	1.71	4.25, 4.26
7: 0+, 0+, 0+, 2+	1.24	2.47	4.27
8: 0+, 0+, 2+, 2+	1.65	2.47	4.28
9: 0+, 0+, 0+, 2+, 2+	1.21	2.47	4.31

Table 4.4: Applied *R*-matrix models (different combinations of 0^+ and 2^+ states) and their reduced χ^2 values. The number of degrees of freedom (df) is 1251 minus the number of free parameters (see text).

- *The Hoyle state*

  In Model 1, only the Hoyle state is included in the fit. This model is already known to be insufficient as argued above, but the simplest models are included here for completeness, and to illustrate their properties. The fit spectra are shown in figure 4.25 compared to the ^{12}N and ^{12}B KVI sum spectra. The Hoyle state energy and width are kept fixed, so there are three free parameters in the fit. The only feature of the spectra, which is reproduced is the narrow Hoyle peak just above threshold. Above the peak, the Hoyle state ghost is seen as a small increase in the spectra, explaining part of the structure of the spectrum in this energy region. Looking at the value of χ^2/d.f. = 281 in table 4.4, it is much larger than unity, as expected. The spectra for decay through the ^{8}Be ground-state peak and excited states are separated in figure 4.26. Only breakup via the ground state contributes due to the low energy of the Hoyle state, and the component for decay via excited energies arises due to the ^{8}Be ground-state ghost seen in figure 4.24. In a fit with variable energy and width of the Hoyle state the energy goes to its lower limit and the width to its upper limit. Both serve to increase the ghost as shown in section

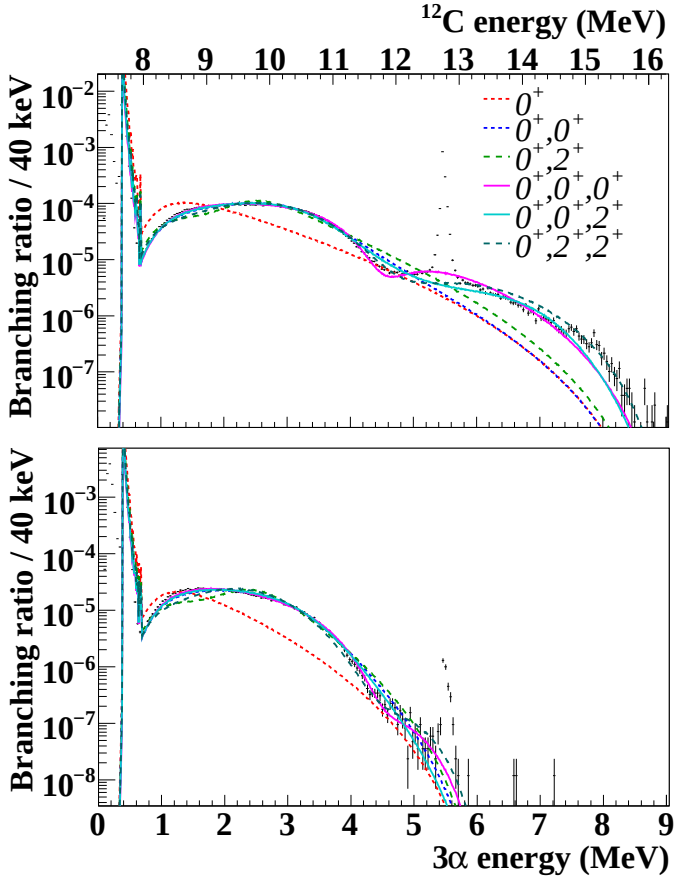

Figure 4.25: 3α energy spectra from the KVI experiment for ^{12}N (top) and ^{12}B (bottom) decay. Fits to Models 1 to 6 in Table 4.4 are shown.

2.5.4 and thus compensate for the missing strength at higher energies in the spectra.

- *The Hoyle state plus one additional state*

  The next step is the addition of a 0^+ state (Model 2). The resulting χ^2 is still much larger than the number of degrees of freedom, but it is a large improvement from Model 1. It is interesting to note that the energy region from 1 to 4 MeV is adequately described in figures 4.25 and 4.26. For the ^{12}B case, with the smaller beta-decay energy window, this model is sufficient and shows that 0^+ interference is an important ingredient for the understanding of the spectrum in this region.

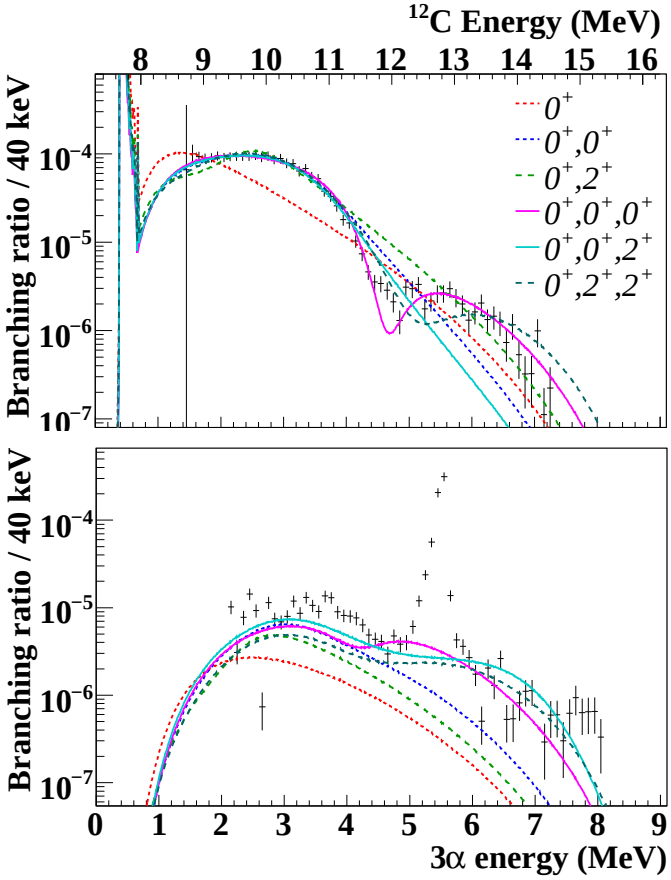

Figure 4.26: ^{12}N decay spectra from the JYFL experiment. 3α energy spectra for the ^{8}Be ground state peak (top) and excited states (bottom) channels are shown. The excited states channels are the ^{8}Be ground state ghost and the 2^+ contribution. Fits to Models 1 to 6 in Table 4.4 are shown.

Model 3 includes the Hoyle state and a 2^+ state. This fit is several times worse than the fit to the Hoyle state and a 0^+ state. A 2^+ component is known to contribute to the spectrum from [Diget 2009], but this analysis shows that a single 2^+ state above the Hoyle state is insufficient. This model is not able to explain the flat, broad structure from 8.8 to 10.5 MeV.

- *The Hoyle state plus two additional states*

  Model 4 and 5 shows that the addition of a 0^+ or a 2^+ state to Model 2 gives almost a factor 5 improvement in χ^2. Model 6 with two 2^+ states

above the Hoyle state fails to do this and the χ^2 fall in-between the results for Model 2 and 3. Model 6 also fails in describing the flat region at 8.8 - 10.5 MeV excitation energy as shown in figure 4.25. Also the upper 2^+-state energy and β strengths go to their upper limits.

The fit with three 0^+ states (Model 4) is the best fit so far. The only visible discrepancy in the spectra is a dip below the measured spectra at 11.8 MeV.

Model 5 (two 0^+ and one 2^+) fails at describing the data from breakup via the ^{8}Be ground state and has also problems in areas where the KVI spectra change rapidly (at 8.5 MeV and 11-12 MeV.). This model was found to be sufficient at describing the JYFL data in [Diget 2006], but the KVI data adds information about the low energy region below 8.5 MeV and the fit from [Diget 2006] overestimates the spectrum in this region.

- *The Hoyle state plus three additional states*

  At this point it seems clear that the addition of at least one more state is needed to describe the data. With four unbound states in the fit, the number of free parameters becomes high, and the fit program converges more slowly. For this reason it is worth excluding the two models with respectively three 0^+ states and three 2^+ states above the Hoyle state right away, because the first does not fulfill the requirement of at least one 2^+ state and for the second, the Hoyle state is not sufficient as the dominating broad 0^+ component below the 1^+ peak. This leaves us with Models 7 and 8 as the only realistic models with four unbound states.

  Figures 4.27 and 4.28 show the fits found to these two models. Both reproduce the spectra very well except for a small systematic deviation at high energy in the ^{8}Be peak channel. The χ^2 value reveals that three 0^+ and one 2^+ states is in fact the better model with $\chi^2/\mathrm{df} = 1.24$ compared to $\chi^2/\mathrm{df} = 1.65$. We can not argue for a more complex model from the data used in the fit since the *R*-matrix model used is only an approximation and the uncertainty in the beta response is not taken into account, so an improvement in reduced chi squared of 0.2 would be comparable to the systematic uncertainty. However both models are inconsistent with the results from angular correlations in the JYFL data [Diget 2009]

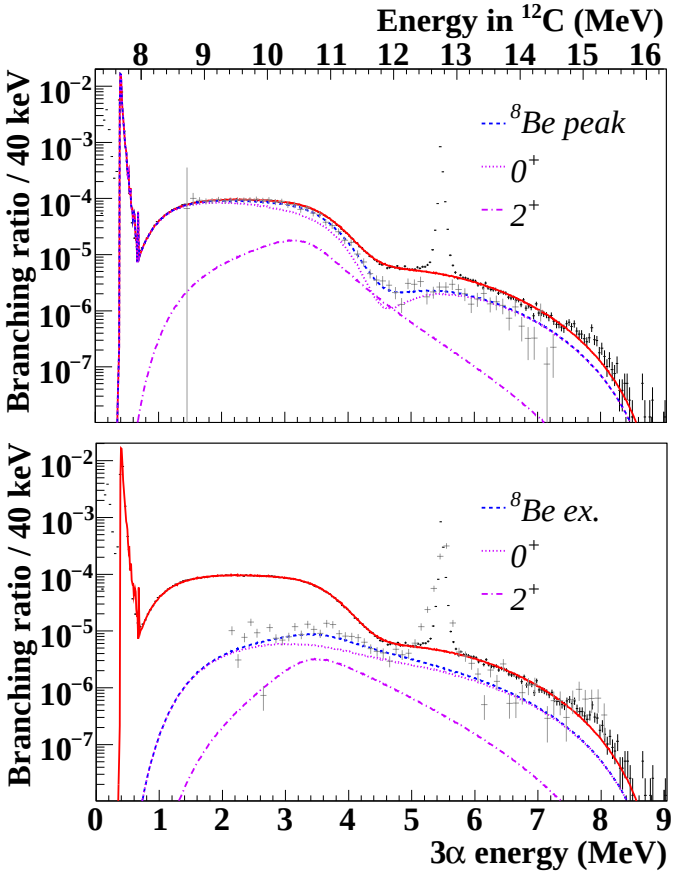

Figure 4.27: Fit to Model 7 in Table 4.4 (three 0^+ and one 2^+ states). Only the ^{12}N spectra are shown. The KVI 3α energy spectra are shown in both plots compared to the solid line showing the total fit spectrum summed over all channels. JYFL 3α energy spectra for the ^{8}Be peak (top) and excited states (bottom) channels are compared to the dashed curves which are the fit components for the respective channels. The dotted and dot-dashed lines are contributions to each decay channel from 0^+ and 2^+ states in ^{12}C respectively.

since the ^{8}Be excited states spectrum both below and above the 1^+ peak is dominated by 0^+ in Fig. 4.27 and 2^+ in Fig. 4.28.

The two fits are also shown in a different type of plot in figures 4.29 and 4.30. The component for each channel in the fits have been corrected for the phase space in the incoming β-decay channel and for the penetrability in the break-up channel. The measured spectrum has been corrected

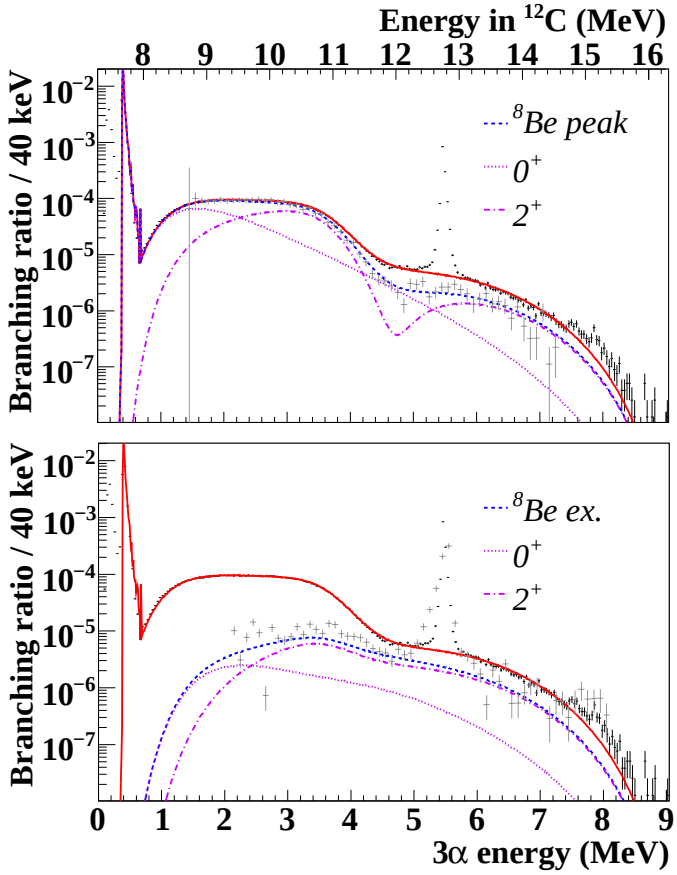

Figure 4.28: Fit to Model 8 in Table 4.4 (two 0^+ and two 2^+ states). See the caption of figure 4.27 for explanation.

using the weighted average penetrability from the fit, so it depends on the fit model. By removing the dependency on the entrance channel and some of the dependency on the exit channels, the spectra have come to illustrate the resonance structures in ^{12}C more clearly, in the same way as was done for ^{8}Be in figure 3.3. The Hoyle state ghost is no longer seen as an increase in the spectrum between 8 and 9 MeV, because the penetrability correction increases the weight of the peak. The structure at 10–11 MeV now looks more like a broad resonance peak with an asymmetric shape due to interference with the Hoyle state. Single levels without interference will have a less asymmetric shape in these plots, but due to

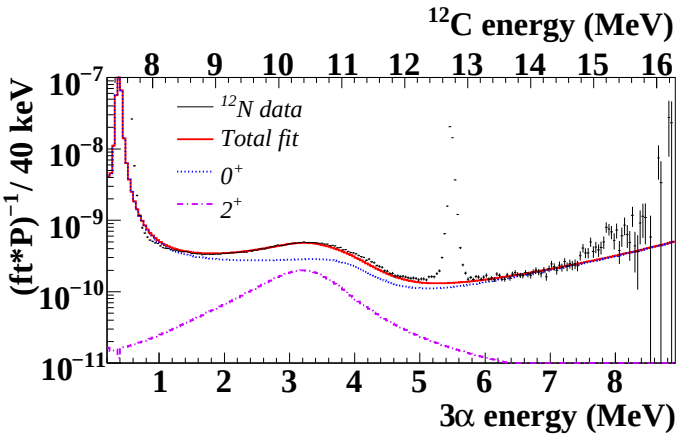

Figure 4.29: Fit to Model 7 in Table 4.4 (three 0^+ and one 2^+ states). The spectrum for ^{12}N is shown as inverse ft value divided by the penetrability to illustrate the resonance shapes. The total fit is shown as the solid line (not corrected for β summing) and the dotted and dot-dashed lines are the components for 0^+ and 2^+ states in ^{12}C respectively.

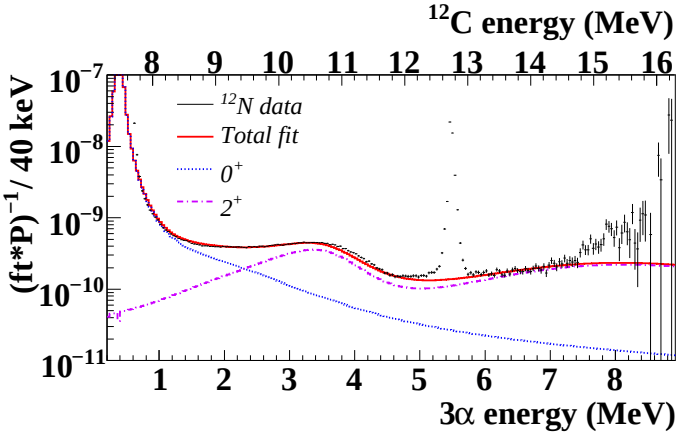

Figure 4.30: Fit to Model 8 in Table 4.4 (two 0^+ and two 2^+ states). See the caption of figure 4.29 for explanation.

the energy dependence of the width in the denominator of equation 2.69 for example the 2^+ level shape in figure 4.29 is slightly asymmetric.

- *The Hoyle state plus four additional states*

  The models with four unbound states have been shown to be insuffi-

cient. All models with five unbound states will not be tested, because the parameter space becomes very large, but a good guess at a model which might explain the data is Model 9 in table 4.4 where the upper 2^+ state from Model 8 is added to Model 7. A fit to this model is shown in figure 4.31, and the spectrum is consistent with both the data and the separate analysis of the JYFL data.

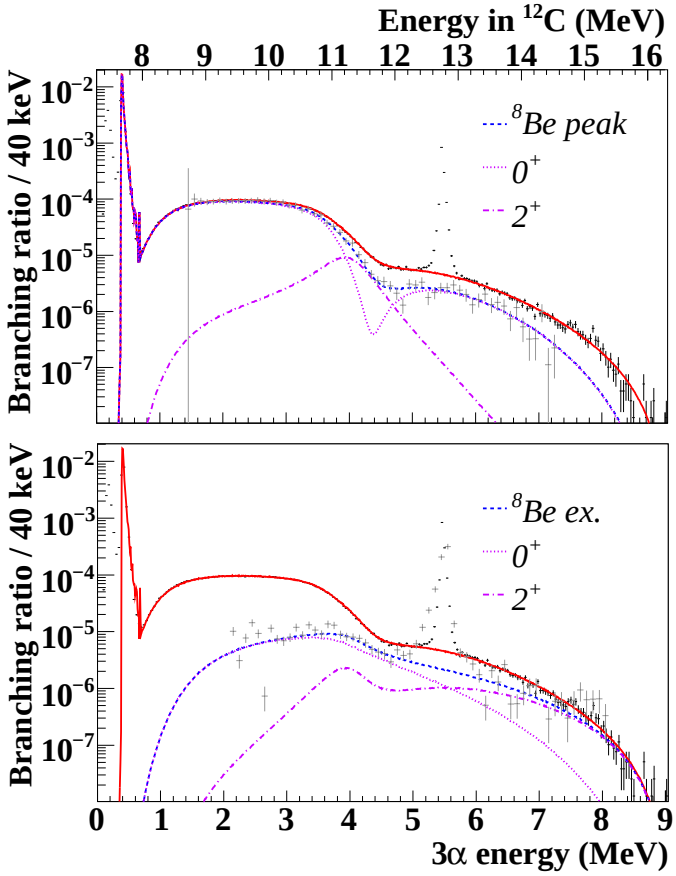

Figure 4.31: Example fit to Model 9 in Table 4.4 (three 0^+ and two 2^+ states). See the caption of figure 4.27 for explanation.

In all fit models the 12.71 MeV peak has been excluded. To test whether its tails has any effect on the spectrum, it is included with its known *R*-matrix parameters in the best fit model as shown in figure 4.33. It is clear from this graph that the state is so narrow, that the tails have no effect on the spectrum

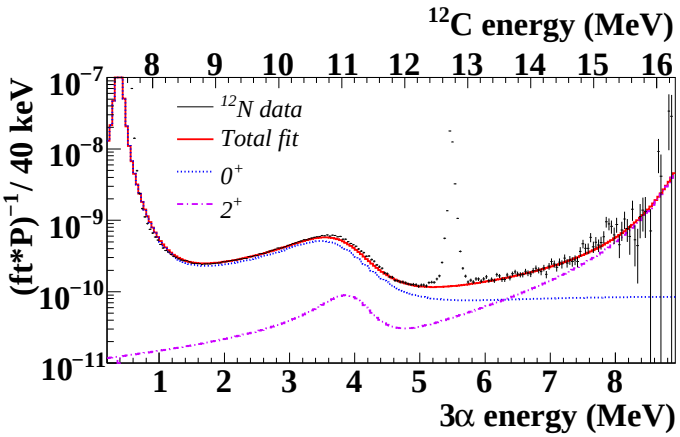

Figure 4.32: Fit to Model 9 in Table 4.4 (three 0^+ and two 2^+ states). See the caption of figure 4.29 for explanation.

in the fit ranges.

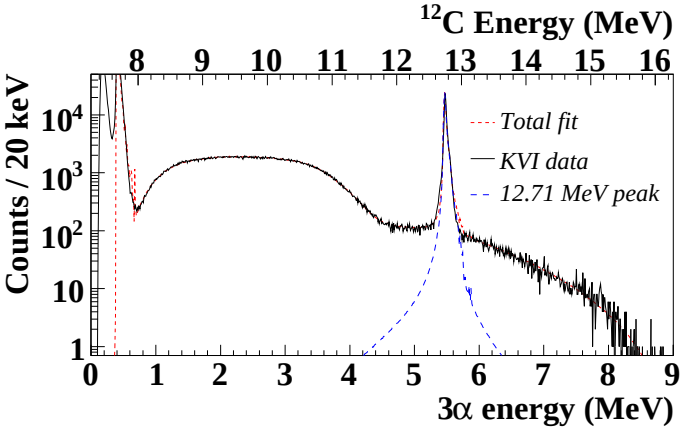

Figure 4.33: The 1^+ state added to the best fit (Model 9), here shown for ^{12}N decay. All *R*-matrix parameters are kept fixed. It is a good approximation to exclude the peak from the fit because of its small width.

The r_0 parameters used in the fits are shown in Table 4.4. For the simple models the value $r_0 = 1.71$ fm has been used and is generally not the optimized value since the models are easily rejected. Larger values were tested in the fit to Model 1 (Hoyle state only) but this gave a worse χ^2.

R-matrix parameters and observables from fits to Models 7–9 are shown

Parameter		Alt.	Alt.	Alt.	Std.
r_0 (fm)		1.71	2.09	2.47	2.47
0_2^+	E (MeV)	7.65	7.65	7.65	7.65
	θ_{00}	2.84	0.809	0.544	0.708
	θ_{22}	−3.66	0.511	1.14	2.58
	Γ^o (eV)	7.65	7.65	7.65	7.65
	$g_{\mathrm{GT}}(^{12}\mathrm{N})$	0.799	0.346	0.347	−0.386
	$g_{\mathrm{GT}}(^{12}\mathrm{B})$	0.869	0.377	0.377	−0.686
	$B_{\mathrm{GT}}(^{12}\mathrm{N})$	0.093	0.093	0.093	0.093
	$B_{\mathrm{GT}}(^{12}\mathrm{B})$	0.110	0.110	0.110	0.110
0_3^+	E (MeV)	12.2	11.2	11.6	11.1
	θ_{00}	2.60	1.21	2.65	1.08
	θ_{22}	3.11	1.99	4.48	0.939
	Γ^o (MeV)	4.62	1.33	2.68	1.61
	$g_{\mathrm{GT}}(^{12}\mathrm{N})$	0.357	−0.246	−0.423	0.228
	$g_{\mathrm{GT}}(^{12}\mathrm{B})$	0.504	−0.281	−0.398	0.422
	$B_{\mathrm{GT}}(^{12}\mathrm{N})$	0.027	0.026	0.027	0.053
	$B_{\mathrm{GT}}(^{12}\mathrm{B})$	0.053	0.033	0.024	0.068
2_2^+	E (MeV)	11.7	11.3	10.8	11.4
	θ_{02}	−0.670	−1.04	−2.97	2.16
	θ_{20}	$3.11 \cdot 10^{-6}$	2.16	4.48	−4.22
	θ_{22}	$1.71 \cdot 10^{-6}$	−2.03	$-2.99 \cdot 10^{-4}$	−0.0415
	Γ^o (MeV)	0.83	1.11	1.77	2.06
	$g_{\mathrm{GT}}(^{12}\mathrm{N})$	−0.0856	−0.376	−0.645	0.650
	$g_{\mathrm{GT}}(^{12}\mathrm{B})$	−0.100	−0.401	−0.752	1.10
	$B_{\mathrm{GT}}(^{12}\mathrm{N})$	0.007	0.053	0.053	0.092
	$B_{\mathrm{GT}}(^{12}\mathrm{B})$	0.010	0.060	0.072	0.099
0_4^+	E (MeV)	67.5	45.3	24.1	26.2
	θ_{00}	2.73	1.68	3.93	−0.961
	θ_{22}	0.659	2.44	4.47	−1.36
	Γ^o (MeV)	109	74.8	154	13.2
	$g_{\mathrm{GT}}(^{12}\mathrm{N})$	−18.4	−21.5	−7.49	−9.35
	$g_{\mathrm{GT}}(^{12}\mathrm{B})$	−22.7	−23.9	−8.15	−16.2
	$B_{\mathrm{GT}}(^{12}\mathrm{N})$	337	461	55	116
	$B_{\mathrm{GT}}(^{12}\mathrm{B})$	513	568	65	129
χ^2/df		2.10	1.35	1.25	1.24

Table 4.5: Level parameters for Model 7.

Parameter		Alt.	Alt.	Alt.
r_0 (fm)		1.71	2.09	2.47
0_2^+	E (MeV)	7.65	7.65	7.65
	θ_{00}	2.46	1.52	1.11
	θ_{22}	2.95	4.06	5.19
	Γ^o (eV)	7.65	7.65	7.65
	$g_{GT}(^{12}N)$	0.691	0.650	0.699
	$g_{GT}(^{12}B)$	0.752	0.707	0.760
	$B_{GT}(^{12}N)$	0.093	0.093	0.093
	$B_{GT}(^{12}B)$	0.110	0.110	0.110
0_3^+	E (MeV)	13.4	96.3	107
	θ_{00}	9.70	18.9	19.9
	θ_{22}	4.48	−2.20	−1.83
	Γ^o (MeV)	44.9	5030	5000
	$g_{GT}(^{12}N)$	−1.24	−2.95	−3.16
	$g_{GT}(^{12}B)$	−1.78	−3.73	−3.62
	$B_{GT}(^{12}N)$	0.20	8.63	9.95
	$B_{GT}(^{12}B)$	0.41	13.8	13.1
2_2^+	E (MeV)	10.9	10.9	10.9
	θ_{02}	−3.00	−1.23	−1.44
	θ_{20}	4.41	0.732	−0.844
	θ_{22}	−4.47	−1.10	−1.40
	Γ^o (MeV)	0.88	1.36	1.67
	$g_{GT}(^{12}N)$	−0.647	−0.331	−0.445
	$g_{GT}(^{12}B)$	−0.651	−0.370	−0.497
	$B_{GT}(^{12}N)$	0.024	0.064	0.103
	$B_{GT}(^{12}B)$	0.025	0.080	0.129
2_3^+	E (MeV)	15.7	16.2	17.5
	θ_{02}	0.682	1.17	1.59
	θ_{20}	−2.77	−0.651	0.835
	θ_{22}	−1.51	−0.640	−0.413
	Γ^o (MeV)	5.63	6.65	10.9
	$g_{GT}(^{12}N)$	0.830	0.949	1.36
	$g_{GT}(^{12}B)$	0.577	1.04	1.52
	$B_{GT}(^{12}N)$	0.55	0.86	1.81
	$B_{GT}(^{12}B)$	0.26	1.04	2.25
χ^2/df		6.37	2.80	1.65

Table 4.6: Level parameters for Model 8.

Parameter		Alt.	Std.	Parameter		Alt.	Std.
r_0 (fm)		2.47	2.47	r_0 (fm)		2.47	2.47
0_2^+	E (MeV)	7.65	7.65	2_3^+	E (MeV)	16.5	16.7
	θ_{00}	0.947	0.966		θ_{02}	−0.488	−0.0491
	θ_{22}	−4.18	−4.30		θ_{20}	0.419	−0.629
	Γ^o (eV)	7.65	7.65		θ_{22}	$9.78 \cdot 10^{-6}$	−0.0753
	$g_{GT}(^{12}N)$	0.653	0.666		Γ^o (MeV)	0.58	0.97
	$g_{GT}(^{12}B)$	0.588	0.600		$g_{GT}(^{12}N)$	2.47	−2.24
	$B_{GT}(^{12}N)$	0.093	0.093		$g_{GT}(^{12}B)$	−1.77	2.18
	$B_{GT}(^{12}B)$	0.110	0.110		$B_{GT}(^{12}N)$	5.1	4.1
0_3^+	E (MeV)	11.0	11.0		$B_{GT}(^{12}B)$	3.8	5.7
	θ_{00}	1.14	0.919	0_4^+	E (MeV)	61.0	65.8
	θ_{22}	1.64	0.433		θ_{00}	7.68	−4.58
	Γ^o (MeV)	1.31	1.33		θ_{22}	8.13	0.277
	$g_{GT}(^{12}N)$	0.653	0.666		Γ^o (MeV)	1109	200
	$g_{GT}(^{12}B)$	−0.414	−0.326		$g_{GT}(^{12}N)$	−8.18	4.87
	$B_{GT}(^{12}N)$	0.078	0.081		$g_{GT}(^{12}B)$	−7.35	4.34
	$B_{GT}(^{12}B)$	0.095	0.10		$B_{GT}(^{12}N)$	55	20
2_2^+	E (MeV)	11.3	11.4		$B_{GT}(^{12}B)$	65	22
	θ_{02}	−0.747	−1.46				
	θ_{20}	0.360	1.78				
	θ_{22}	$2.03 \cdot 10^{-5}$	−2.51				
	Γ^o (MeV)	0.87	1.44				
	$g_{GT}(^{12}N)$	0.179	0.461				
	$g_{GT}(^{12}B)$	−0.157	−0.384				
	$B_{GT}(^{12}N)$	0.025	0.047				
	$B_{GT}(^{12}B)$	0.028	0.047				
χ^2/df		1.21	1.22			1.21	1.22

Table 4.7: Level parameters for Model 9.

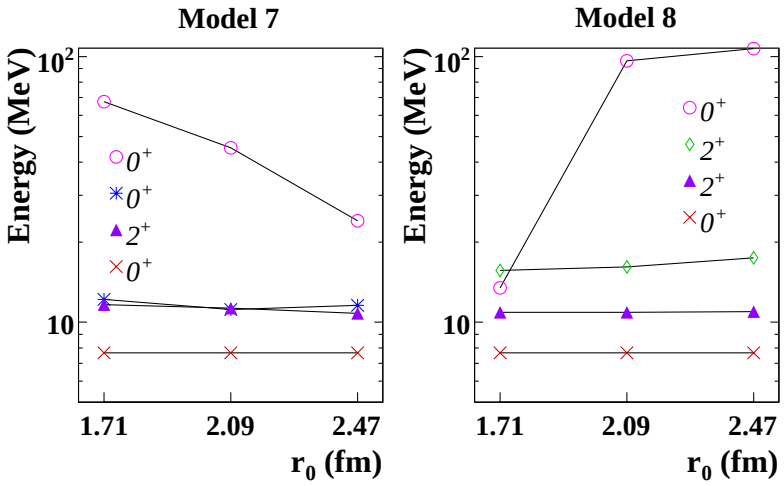

Figure 4.34: Level energies in R-matrix fits to different channel radii. Note the systematic uncertainty on the extracted energies (see the text).

in tables 4.5, 4.6 and 4.7. The fit spectra are uniquely defined by the energies, reduced widths and beta strengths and these are given here for future reference. It should be noted that the ^{8}Be intermediate states are integrated from 0–5 MeV for the ground state and 0–10 MeV for the first excited state. Other conventions will lead to different reduced widths. The reduced widths are given by the dimensionless, $\theta_{\lambda c}$ (equation 2.115), relative to the Wigner limit (equation 2.113). The beta strengths are normalised to the equality

$$B_{\mathrm{GT}} = \left|\frac{g_V}{g_A}\right|^2 \frac{|g_{\lambda\mathrm{GT}}|^2}{1 + \sum_c \gamma_{\lambda c}^2 \left.\frac{\delta S_c}{\delta E}\right|_{E=E_\lambda}} \tag{4.13}$$

and the B_{GT}-value for the Hoyle state shown in table 4.3, found from the peak branching ratio, defines the scale.

For the more complex models different r_0 values have been tested and for Models 7–9 the optimum value is $r_0 = 2.47$ fm (out of the discrete set: 1.71, 2.09, 2.47 and 2.85 fm). For Model 7 and 8 the level energy dependency on r_0 is illustrated in figure 4.34. For the three lowest energy states the level energy is largely independent of channel radius lending further support to these resonances being physical. The energy of the upper 0^+ state in Model 7 decreases with increasing r_0. This effect was also seen for ^{8}B decay (see figure 3.11 in chapter 3 and figure 4 in [Warburton 1986]), and indicates that this is

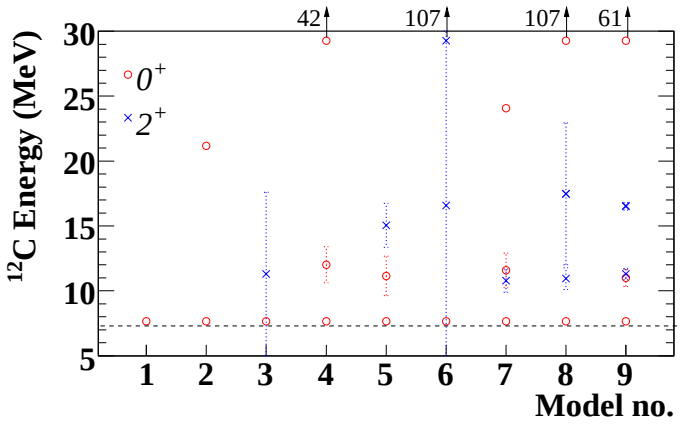

Figure 4.35: Level energies for the fits in table 4.4. Note the systematic uncertainty on the extracted energies (see the text). Dotted lines are not error bars but indicate observed widths. For clarity these are omitted for the upper 0^+ states which have extremely large widths. The triple-α threshold is indicated with a dashed line.

not a physical resonance. The physical effect responsible for this component might be the sum of contributions from several high-energy resonances, or decay directly via the continuum. This will be discussed in the next chapter. The upper 0^+ state of Model 8 does not show the same monotonous decrease in energy, but this is probably because an additional 0^+ state is needed in the 10–11 MeV energy region and the fit is trying to compensate for this.

All fits in table 4.4 were performed using the alternative *R*-matrix parametrisation. Fits within the standard parametrisation are shown for comparison in tables 4.5 and 4.7 to values from the two best models. Energies and χ^2 are similar in the two pairs of fits but widths and B_{GT} values differ substantially. These are the same tendencies as seen in fits within the same formalism but with different limits on the parameters or different initial parameters. This gives an indication of the systematic uncertainty of the formalism.

Figure 4.35 shows the level energies in the different fit models in table 4.4. The Hoyle state is fixed at its known energy of 7.654 MeV in all models. Due to its high-energy tail or ghost the Hoyle state contributes to the spectrum also at higher energies, and this leads to the interesting possibility of trying to measure the width of this state from the present data [Diget 2006]. However, due to the uncertainty in the contribution of other states it is not possible at

Level	Parameter	Recommended value
0_3^+	E (MeV)	11.2 ± 0.3
	Γ^o (MeV)	1.5 ± 0.6
	$B_{GT}(^{12}\mathrm{N})$	0.06 ± 0.02
	$B_{GT}(^{12}\mathrm{B})$	0.07 ± 0.03
2_2^+	E (MeV)	11.1 ± 0.3
	Γ^o (MeV)	1.4 ± 0.4
	$B_{GT}(^{12}\mathrm{N})$	0.05 ± 0.03
	$B_{GT}(^{12}\mathrm{B})$	0.06 ± 0.04

Table 4.8: Recommended observable values for the 0_3^+ and 2_2^+ states from this work.

the present stage to improve on the literature value using this idea. The width as well as the energy of the Hoyle state is therefore kept fixed in the fits. Both the $L = 0$ and $L = 2$ channels are included for the Hoyle state although the $L = 2$ channel only affects the very high-energy tail of the ghost. Only one of the reduced widths is varied while the other is defined by the total observed width. The dimensionless reduced width, θ_{00}, is ~ 1 for the fits in tables 4.5, 4.6 and 4.7 corresponding to a reduced width close to the Wigner limit.

At higher energy a 0^+ and 2^+ state are seen below the 12.71 MeV peak. Both have energies which do not vary much in fits to different models (Fig. 4.35) or different r_0 values (Fig. 4.34). The widths and B_{GT} values differ, however, by at least a factor of two in different fits, but the states are both known to be broad with reduced widths often surpassing the Wigner limit. Recommended observable values for these states are given in Table 4.8. The values and errors are found by comparing results from fits to Models 7–9 (except Model 8 for the 0_3^+ state) and fits for different r_0 values.

The next resonance in the fits is a 2^+ state with energy varying somewhat more than the low-energy 0^+ and 2^+ states, but remaining close to the ^{12}N Q-value. Its width and B_{GT} values can not be determined.

The upper 0^+ state has an energy above the Q-value, but otherwise it can not be determined. The reduced widths and beta strengths often go to the upper limits allowed in the fit so the width and B_{GT} values can not be determined, we can only see that they have to be very large. Especially the B_{GT}

values are much larger than the sum-rule limit.

4.7 Comparison to theory

In this section the B_{GT} values for the narrow states (table 4.3) and the properties for the 0_3^+ and 2_2^+ states found in this work are compared to predictions from theory. Different conventions are used in the literature for the front factors on the B_{GT} values, so the theoretical calculations are tabulated here for the definition used in this work (equation 4.10).

B_{GT} values calculated within the antisymmetrised molecular dynamics (AMD) approach are shown in table 4.9 in comparison to experimental values for transitions from ^{12}N [Kanada-En'yo 1998, Kanada-En'yo 2007]. The B_{GT} values for the narrow states are seen to be consistent within a factor two, except the older value for the Hoyle state from [Kanada-En'yo 1998]. Calculations for the third 0^+ state are in good agreement with the result from R-matrix fits, and the AMD energy of 11.7 MeV (3 MeV above the Hoyle state) is consistent with the level energy found in the fits. For the 2_2^+ state the energy, which is about the same as for the 0_3^+ state, is consistent with our experimental result, but the predicted feeding is very small. A 2_3^+ state was found in the same calculation around 13 MeV and the B_{GT} value for this state is also small considering that the β strength rises at higher energy. A 2_4^+ state was also found between 13 and 15 MeV in the same calculation as well as two 4^+ states between 10 and 13 MeV and a 6^+ state around 15 MeV.

In table 4.11 the experimental B_{GT} values are compared to the results from no-core shell model (NCSM) calculations [Hyldegaard 2009b]. The calculations were performed using high-precision nuclear Hamiltonians from chiral perturbation theory (ChPT) as in [Navrátil 2007]. This was done for a nucleon-nucleon (NN) interaction both with and without a three-nucleon force (3NF). Table 4.10 shows an earlier calculation of the strength to the ground state using the Argonne V8 nucleon-nucleon potential by itself and combined with the Tuscon-Melbourne TM(99) three-nucleon interaction respectively [Navrátil 2003]. The calculation from [Navrátil 2003] does not include the isospin breaking due to the Coulomb and the strong force as was the case for the ChPT nucleon-nucleon interaction in [Navrátil 2007], so the results are identi-

E_x (MeV)	J^π	Experiment	AMD	
		^{12}N	[Kanada-En'yo 1998]	[Kanada-En'yo 2007]
0	0_1^+	0.2950(14)	0.605	0.605
4.44	2_1^+	0.0270(4)	0.060	0.060
7.65	0_2^+	0.093(2)	0.381	0.191
11.2(3)	0_3^+	0.06(2)	0.076	0.076
12.71	1_1^+	0.462(12)	0.605	0.761
11.1(3)	2_2^+	0.05(3)		$0.002(2_2^+)$
				$0.038(2_3^+)$

Table 4.9: B_{GT} values calculated using AMD compared to experimental values from the present work.

cal for ^{12}B and ^{12}N transitions. For the ground state transition strength it is evident that a three-nucleon force is needed to describe the state, and the result from [Navrátil 2003] is in reasonable agreement with the experimental values but even better consistency is obtained for the newer calculations [Hyldegaard 2009b]. The calculated transition to the 1^+ 12.71 MeV state is in much better agreement with the present data that reduce the branching ratio by a factor of 2.5 compared to earlier measurements. The current NCSM calculations do not properly describe the Hoyle state, because of its dilute cluster structure. The NCSM 0_2^+ state is at about twice the excitation energy of the 7.654 MeV state and the B_{GT} values are strongly overestimated in table 4.11. A second 2^+ state was found around 15–16 MeV with a large GT strength. This could possibly correspond to the third 2^+ strength in Model 9 for which the strength could not be determined in the fits. Instead an estimate is given in table 4.11 obtained by integrating the inverse ft value in figure 4.23. These values are consistent with the calculations including the 3NF. The experimentally observed asymmetries are not reproduced in the calculations as no coupling to the continuum is included and the employed ChPT 3NF is isospin invariant.

The Gamow-Teller strength in the β-decays of ^{12}N and ^{12}B has also been studied with phenomenological approaches. Using a derived effective inter-

E_x (MeV)	AV8 + TM $4\hbar\omega$	AV8 $4\hbar\omega$
0	0.222	0.0850

Table 4.10: No-core shell model calculations of the Gamow-Teller strength to the ground state both with and without the Tuscon-Melbourne TM(99) three-nucleon interaction [Navrátil 2003].

E_x	J^π	^{12}N			^{12}B		
(MeV)		Exp.	NN	NN + 3NF	Exp.	NN	NN + 3NF
0	0^+	0.2950(14)	0.081(20)	0.337(79)	0.331(2)	0.082(20)	0.341(81)
4.44	2^+	0.0270(4)	0.0050(9)	0.0054(13)	0.0297(9)	0.0044(6)	0.0044(11)
7.65	0^+	0.093(2)	1.18(23)	0.85(11)	0.110(3)	0.98(15)	0.88(13)
12.71	1^+	0.462(12)	0.710(8)	0.662(26)	0.51(3)	0.837(12)	0.687(26)
15 – 16	2^+	0.6(2)	1.50(16)	0.80(8)			

Table 4.11: B_{GT} values from no-core shell model calculations compared to experimental values from the present work. Isospin breaking is included in the nucleon-nucleon (NN) interaction. The three-nucleon force (3NF) is isospin invariant [Hyldegaard 2009b].

action [Warburton 1992] for the 0p1sd shell-model space the GT strengths to the states listed in table 4.12 were calculated in [Chou 1993]. Their B_{GT}-values are very similar to the NCSM NN + 3NF results. The 7.654 MeV (0^+_2) state was considered to be outside the 0p1sd model space, but in contrast to NCSM a 0^+ state in the 9–12 MeV range was found in the model space. Note, however, that the experimental 10.3 MeV state was included in the list of states used to derive the effective interaction [Warburton 1992].

The shell-model calculations by [Suzuki 2003] and [Smirnova 2003] are only for the ground state and the 4.44 MeV state. The calculations are consistent within 10% to this work.

The broad 0^+_3 and 2^+_2 states are not explained by the NCSM indicating that these are strongly clustered states in ^{12}C. 3α cluster calculations give a

E_x (MeV)	J^π	Experiment		[Chou 1993]		[Suzuki 2003]	
		^{12}N	^{12}B	free	eff.	$0\hbar\omega$	$2\hbar\omega$
0	0^+	0.2950(14)	0.331(2)	0.502	0.341	0.3867	0.3228
4.44	2^+	0.0270(4)	0.0297(9)	0.039	0.033	0.0352	0.0299
11.2(3)	0^+	0.06(2)	0.07(3)	0.943	0.641		
12.7	1^+	0.462(12)	0.51(3)	0.887	0.638		
15.11	1^+			0.0346	0.0214		

Table 4.12: Shell-model calculations of B_{GT} values from [Chou 1993] and [Suzuki 2003].

	E_x (MeV)	J^π	INC + HO	I : INC + WS	II : INC + WS	II : (INC + WS)*
^{12}B	0	0^+	0.315	0.264(0.281)	0.292(0.291)	0.264
	4.44	2^+	0.0644	0.0607(0.0620)	0.0614(0.0611)	0.0592
^{12}N	0	0^+	0.313	0.225(0.243)	0.265(0.263)	0.216
	4.44	2^+	0.0648	0.0543(0.0557)	0.0569(0.0564)	0.0532

Table 4.13: Shell-model calculations of the Gamow-Teller strength to the ground state and first excited state. [Smirnova 2003].

11.3 MeV, $\Gamma^o = 1$, 0^+ state consistent with the experimental value found in this work [Álvarez Rodriguez 2007]. The coexistence of a 2_2^+ and a 0_3^+ state in the 9 to 12 MeV energy region is also consistent with results in the complex-scaling method [Kurokawa 2004].

CHAPTER 5

Direct decay

Common for the analysis of the $A = 8$ and 12 β-decay experiments is the need for one or more levels in the R-matrix model with unphysically large widths and or beta strengths. In the R-matrix framework the reason for this is that the basis has been truncated to a final size and the unphysical levels merely compensate for the lacking, and in principle infinitely many continuum levels. In this chapter the possibility will be explored whether the unphysical levels account for direct decay via the continuum rather than for higher lying resonances that can not be constrained further with the present data.

R-matrix formalism is specifically well suited for analysing resonant processes. Direct reactions or decay are not as easily treated. As noted in [Lane 1958, II 4 p. 265], *"..the only factor in R-matrix theory that could possibly correspond to direct mechanisms are the sums over the far-away levels"*. This short remark is consistent with the fact that not all R-matrix levels are resonances. Lane and Thomas discuss in XI 6 p. 318 how direct processes can be treated quantitatively within R-matrix. The principle is that direct decay must be associated with single-particle motion and to account for very short lifetimes (large widths) one must sum over many, longer-lived levels with long-range correlations between the levels in the sum.

A simple model of the direct decay component is a series of single-particle levels for the square-well potential with constant potential, V_0, in the internal region. The solutions for the level energies are [Lane 1958, IV 3 p. 275]

$$E_\lambda = V_0 + \frac{\pi^2\hbar^2}{2\mu_c a_c^2}\left(\lambda - \frac{1}{2}\right)^2, \qquad \lambda = 1, 2, 3, \cdots \tag{5.1}$$

and the reduced width amplitudes are equal to the Wigner limit with alternating signs,

$$\gamma_\lambda = (-1)^{\lambda+1}\left(\frac{\hbar^2}{\mu_c a_c^2}\right). \tag{5.2}$$

Even if $V_0 = 0$ there will be an infinite number of solutions, and such levels can not be interpreted as resonances in the sense that a compound nucleus has to be formed for a resonant process to take place, and that is not possible with no interaction between the particles. The solutions to the square-well potential with zero interaction sum to a total cross section at all energies of zero (in the case of scattering) as was already realised by Wigner and Eisenbud in 1947 [Wigner 1947]. The example was used as an illustration to show that the result can become very wrong if only the first few levels are included and that an energy level not always corresponds to an increase in the cross section at the level energy. Direct reactions were not seen experimentally before a few years after the paper by Wigner and Eisenbud.

The square-well energy levels depend on the channel radius. When the channel radius is increased the level energies decrease and this is exactly the tendency both seen in β decay of ^{8}B for the energy of the intruder state (figure 3.11) and in β decay of ^{12}N and ^{12}B for the energy of the upper 0^+ state (figure 4.34). Both the spectra for $A = 8$ and $A = 12$ are adequately described by a model where the high-energy levels are replaced by a series of e.g. 3–5 square-well levels with fixed level spacing and reduced widths. The only variable parameters are the offset V_0 and common β strength, g_λ.

The interpretation of Barker's intruder state in ^{8}Be as a resonance is difficult because no peak or other feature is seen in the spectrum. Barker's crucial argument for why a 2^+ state should exist between the 3 MeV state and the doublet is that the model fits both reaction, decay and scattering data simultaneously. This requirement is very reasonable, but looking at the results from Barkers' most recent analysis [Barker 1989], the agreement between the fits to the d-wave scattering phase shift and β-decay α spectrum is not impressive. Barker finds that the scattering phase shift suggests a 3 MeV peak that is more narrow than indicated by the β-decay α spectra and the simultaneous fits give reduced χ^2 values of about 2.5 [1]. In both β decay and α-α scattering a contribution from direct decay could reasonably contribute to the spectra, but not necessarily in the same way, and that might explain the deviations.

In the β decays to ^{12}C the unphysical upper 0^+ and 2^+ states appear when

[1] The values of $\chi^2/df \sim 2.5$ were obtained by re-calibrating the α-spectra measured by Wilkinson and Alburger [Wilkinson 1971]. Using the original calibration Barker obtains $\chi^2/df \sim 3.5$ in the best fits.

trying to fit the component above the 12.71 MeV peak in the spectrum for ^{12}N decay. From figures 4.29, 4.30 and 4.32 it is evident that the strength increases above the 12.71 MeV peak but otherwise the only structure seen is the 15.11 MeV peak. The strength between 15 and 16 MeV of 0.6(2) is a large fraction of the allowed strength, which was estimated to between 2 and 4 according to the sum rule in section 2.7.2, where ~ 1 has to be subtracted for the known strength to bound and unbound states. The spectrum is very slowly increasing between 13 and 15 MeV, and if this is due to the low-energy tail of a resonance it would either have to be very broad or lie above the Q-value with a very large strength as found in Models 8 and 9 (see tables 4.6 and 4.7). States with close to a reasonable strength were found below or close to the Q-value for Model 8, but those solutions were aided by the interference with a 2^+ state dominating below the 12.71 MeV peak, and the 15–16 MeV region, which is excluded from the fit, becomes somewhat underestimated.

For both ^{8}B- and ^{12}N-/^{12}B-decay the spectra are constructed of a few resonance peaks plus regions with virtually no structure. Of the two possible interpretations of the broad regions, either in terms of decay directly via the continuum or several broad, interfering states, the direct decay model seems the most adequate.

It is not possible to obtain further information about the break-up mechanism from R-matrix theory. Theories which can distinguish resonant from direct decay contributions are required for this purpose. One such candidate is the shell model in the continuum [Okolowicz 2003].

β decay directly to the continuum is a probable decay mechanism for systems with a dilute structure in the initial state providing a larger overlap with the continuum wave functions. A good example is halo nuclei such as ^{6}He and ^{11}Li. The ^{6}He nucleus decays predominantly to the ^{6}Li ground state but has a very small branch for decay directly to the $\alpha + d$ continuum, $BR = 1.65(10) \cdot 10^{-6}$ [Raabe 2009]. Measurements of the β decay of ^{11}Li indicate a direct decay component to $^{9}\mathrm{Li} + d$ [Raabe 2008]. Another nucleus which might possess a direct decay channel is ^{9}Li. The β-delayed breakup of ^{9}Li has been analysed in terms of resonant breakup via ^{9}Be [Prezado 2005], and because these resonances are all very broad, it is possible that direct decay could account for some of the β strength. For both ^{8}Be, ^{12}C and ^{6}He, direct decay is

observed close to the Q-value, and if this is a general aspect of direct decay, the experimental observation of the effect requires high-statistics measurements.

CHAPTER 6

Summary

In this work β-decay to light nuclei breaking up into α particles has been studied with different experimental techniques. The data has been analysed within the R-matrix formalism for multiple levels and many break-up channels.

The β decay of ^{8}B has been investigated using the IGISOL method and coincident detection of the two β-delayed α particles with a detector setup of large solid-angle coverage. The experiment has provided a high-quality spectrum of 2α coincidences and the accuracy of the measurement is further supported by the consistency between the coincidence and single-α spectra. Previous measurements of the β decay of ^{8}B did not provide this internal consistency check, and the amount of data in other coincidence measurements was significantly less. The spectrum presented here disagrees with the spectra in [Winter 2006] and [Bhattacharya 2006]. The 3 MeV peak energy in our data is 25 keV lower.

The 2α energy distribution has been fitted using R-matrix models for a single break-up channel ($L = 2$) serving as the simpler example of application of the formalism in the context of this thesis. Good fits were obtained for four unbound 2^+ levels in the model: The 2^+_1 state at 3 MeV, the two states forming the isospin doublet at 16.6 MeV and an additional level either below or above the doublet. This confirms the results in [Warburton 1986] and [Bhattacharya 2006], that no state below the doublet is needed to describe the data, but at the same time, Barker's model with a state below the doublet fits the data equally well [Barker 1969, Barker 1989]. In either case the contribution from the third level is small and very broad and the interpretation of such a level below the doublet as a resonance is questionable. A more likely explanation is probably in terms of direct decay.

The ^{8}Be(2α) final state distribution presented here is the most accurate

measurement to date, with a thorough understanding of the experimental effects and an excellent *R*-matrix parameterisation. It will be used to calculate a revised neutrino spectrum for ^{8}B β decay. A preliminary spectrum was presented here in comparison to the standard reference [Winter 2006], and the disagreement in the ^{8}Be energy spectra is seen to also give differences in the neutrino spectra.

A complementary measurement to the one presented here has been performed at KVI with the implantation technique described in section 4.4. The analysis of this experiment is currently being performed and the result will provide an interesting comparison with the final state distribution from JYFL.

Unbound states in the triple-α continuum of ^{12}C have been studied with β decay of the mirror isotopes ^{12}B and ^{12}N. This was done using the same method as for ^{8}B decay with a similar setup to obtain 3α coinidence data. As for ^{8}B the method provides an internal consistency check by comparing single-α and 3α spectra. The comparison is less straight forward for three α particles and some assumptions on the breakup are required. Results for the relative branching ratios from single and 3α data are in good agreement. The full kinematics of the breakup was measured and this has provided new insight in the breakup mechanism as a function of the excitation energy [Diget 2009].

A complementary experiment for studying β decay to ^{12}C was performed using inverse kinematics for production of ^{12}B and ^{12}N, which were implanted inside the detector. This allowed for studies of the low-energy region of the 3α continuum including the Hoyle state. High precision branching ratios and B_{GT} values for the narrow states was obtained model-independently from the data. The ^{12}N and ^{12}B spectra from this experiment have been analysed simultanously with spectra separated into the individual break-up channels from the IGISOL experiment within the *R*-matrix formalism adapted to sequential three-body breakup via broad intermediate states. It was possible to obtain good fits to models with four unbound states: The Hoyle state, a 0^{+} state, a 2^{+} state and an additional 0^{+} or 2^{+} state. To obtain consistency with the requirements from the separate analysis of the IGISOL data that 0^{+} dominates below the 12.71 MeV peak and 2^{+} above it, in the break-up channel to excited states in ^{8}Be, a fifth level was included in the parametrisation. The analysis shows

evidence for a 0^+ and a 2^+ state between 10.5 and 12 MeV confirming the result from [Diget 2005] that the 10.3 MeV state in the literature with $\Gamma = 3$ MeV and possible 0^+ assignment has been misinterpreted as a very broad state due to its interference with the Hoyle state and the threshold effect giving rise to the Hoyle state ghost between 8 and 9 MeV. That the resonance is located closer to 11 MeV is seen by plotting the spectra divided by the phase space and penetration function for the breakup channel as in figure 4.32. In general this type of plot is a better illustration of the resonance distribution than the measured spectra. The 2_2^+ state found in this work is broad and with its high energy it is not expected to contribute significantly to the triple-α process. The data presented here shows no evidence for an unbound 2^+ state at lower energies as suggested by other experiments [Itoh 2004, Freer 2009]. The two additional 0^+ and 2^+ levels above the Q-value are characterised by unphysical parameters and can not be interpreted as physical resonances. As discussed in chapter 5 the most adequate interpretation of the increase in strength above the 1^+ peak is in terms of direct decay. With the analysis of the 3α continuum in ^{12}C presented here, the applicability of *R*-matrix theory has reached its limits, and a better understanding of these processes can only be obtained by dedicated theoretical work.

Other experimental studies which might shed more light on the existence of a low-lying 2_2^+ state in ^{12}C are e.g. the reaction studies mentioned in the introduction performed at the Centro de Microanálisis de Materiales in Madrid [Kirsebom 2009]. The precise 2^+ contribution to the spectra in figure 1.5 is not expected to be determined unambiguously, but an assessment of the contribution of a 2^+ component between the peaks should be possible from a Dalitz plot analysis similar to that performed for the 3α coincidence experiment presented here [Diget 2009]. Such an analysis could determine if the suggested 2^+ states around 9 MeV are not seen in β decay studies merely because the state has a vanishing overlap with the ^{12}N and ^{12}B ground states.

New experimental studies of the β-delayed 3α breakup are planned at JYFL to repeat the 2004 experiment with increased statistics. This could improve our understanding of the high-energy region of the 3α spectrum, where the amount of events in the preceding experiment was too low to reject or confirm the shape of the spectrum measured at KVI. It will also constrain the

breakup mechanism of the high-energy components further.

APPENDIX A

Details of the formalism

A.1 The shift and penetration functions

The shift and penetration functions are given in equations 2.27 and 2.28. The negtive energy solution for the shift function was not given, so for completeness the full solutions are

$$S_c(\eta_c, \rho_c) = \begin{cases} \rho \mathrm{Re}\left(\frac{F_c \cdot F_c' + G_c \cdot G_c'}{|F_c^2| + |G_c^2|}\right), & E > 0 \\ 0, & E = 0 \\ \rho \mathrm{Re}\left(i\frac{H_c'}{H_c}\right), & E < 0 \end{cases} \tag{A.1}$$

$$P_c(\eta_c, \rho_c) = \begin{cases} \frac{\rho}{|F_c^2| + |G_c^2|}, & E > 0 \\ 0, & E \leq 0, \end{cases} \tag{A.2}$$

where $\mathrm{Re}(x)$ denotes the real part. η_c and ρ_c are defined as [Lane 1958]:

$$\eta_c = \alpha Z_1 Z_2 \sqrt{\frac{\mu_c c^2}{2|E|}} \tag{A.3}$$

$$\rho_c = \sqrt{\frac{2\mu_c |E|}{\hbar^2}} a_c \tag{A.4}$$

where α is the fine structure constant, μ_c is the reduced mass and a_c the channel radius $a_c = r_0(A_1^{1/3} + A_2^{1/3})$.

The Coulomb and Hankel functions are calculated using the C++ implementation cwfcomplex [Michel 2007]. This program has been tested and found to be consistent with a similar program in fortran using the CERNLIB routine WCLBES [Thompson 1985, Thompson 1986]. The Gnu Scientific Library routine gsl_sf_coulomb_wave_FGp_array can also be used to calculate Coulomb wave-functions, but only for positive energies [GSL 2010].

The shift and penetration functions for the α-α system with $L = 2$ are shown in figure A.1. Both are monotonically increasing functions.

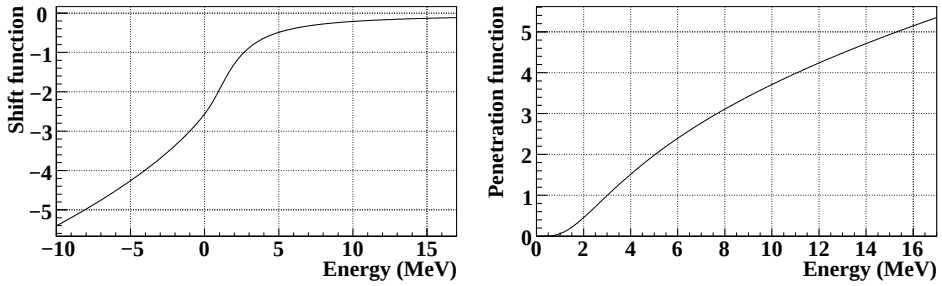

(a) Shift function. (b) Penetration function.

Figure A.1: Shift and penetration functions for the $L = 2$, α-α system.

A.2 Integral of the single-level energy profile

In this section the integrals of equations 2.69 and 2.71 will be shown to be given by the results in equations 2.97 and 2.96 respectively.

Considering first the narrow level approximation and choosing $S_c(E_\lambda) = B_c$,

$$w_\lambda(E) = C^2 f_\beta \sum_{\text{x=F,GT}} \frac{|g_{\lambda x}|^2}{\left(1 + \sum_c \gamma_{\lambda c}^2 \left.\frac{\delta S_c}{\delta E}\right|_{E=E_\lambda}\right)} \frac{\frac{1}{2}\Gamma_\lambda^o}{|E_\lambda - E + i\frac{1}{2}\Gamma_\lambda^o|^2}, \tag{A.5}$$

the integral over all energies is

$$\int_0^\infty w_\lambda(E)dE = C^2 f_\beta \sum_{\text{x=F,GT}} \frac{|g_{\lambda x}|^2}{\left(1 + \sum_c \gamma_{\lambda c}^2 \left.\frac{\delta S_c}{\delta E}\right|_{E=E_\lambda}\right)} \int_0^\infty \frac{\frac{1}{2}\Gamma_\lambda^o}{|E_\lambda - E + i\frac{1}{2}\Gamma_\lambda^o|^2} dE. \tag{A.6}$$

The integrant will now be denoted $f(E)$ and has complex poles for $E = E_\pm = E_\lambda \pm \frac{i}{2}\Gamma_\lambda^o$. The integral can be evaluated by performing the path integral along the contour shown in figure A.2 in the anticlockwise direction around the pole in the upper half-plane. The path integral along the contour, c, is given by Cauchy's residue theorem,

$$\oint_c f(E)dE = 2\pi i \,\text{Res}(f, E_\lambda + \frac{i}{2}\Gamma_\lambda), \tag{A.7}$$

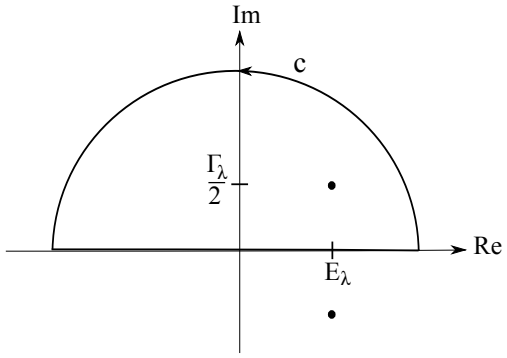

Figure A.2: Poles and contour in the complex plane.

where the residue at the pole is found using the formula for a pole of first order,

$$\mathrm{Res}(f, E_+) = \lim_{E \to E_+} (E - E_+) f(E) = \frac{-\Gamma_\lambda/2}{E_- - E_+} = \frac{1}{2i}. \tag{A.8}$$

The path integral along the arc of the contour vanishes as the radius goes to infinity, leaving $\oint_c f(E)dE = \int_{-\infty}^{\infty} f(E)dE$. Because E_λ is positive and the level narrow, the integral over the negative energies can be neglected and equation A.7 gives,

$$\int_0^\infty \frac{\frac{1}{2}\Gamma_\lambda^o}{|E_\lambda - E + i\frac{1}{2}\Gamma_\lambda^o|^2} dE = \pi, \tag{A.9}$$

leading to the result in equation 2.96.

For broad states the integral reads

$$\int_0^\infty w_\lambda(E)dE \approx C^2 f_\beta \sum_{\mathrm{x=F,GT}} |g_{\lambda x}|^2 \int_0^\infty \frac{\frac{1}{2}\Gamma_\lambda}{|E_\lambda - E + \Delta_\lambda + i\frac{1}{2}\Gamma_\lambda|^2} dE, \tag{A.10}$$

which is valid when the variation of the phase space factor can be neglected over the energy range of the level. This is a valid assumption for levels far from the Q-value. For the inverse ft value the integral is given by the exact expression,

$$\int_0^\infty (ft)_\lambda^{-1}(E)dE = C^2 \sum_{\mathrm{x=F,GT}} |g_{\lambda x}|^2 \int_0^\infty \frac{\frac{1}{2}\Gamma_\lambda}{|E_\lambda - E + \Delta_\lambda + i\frac{1}{2}\Gamma_\lambda|^2} dE. \tag{A.11}$$

In the single-level cross section formula an additional penetrability is added from the reaction channel,

$$\sigma_\lambda(E) = C^2\gamma_{\lambda c}^2 P_c(E)\frac{\frac{1}{2}\Gamma_\lambda}{|E_\lambda - E + \Delta_\lambda + i\frac{1}{2}\Gamma_\lambda|^2}, \tag{A.12}$$

so, similar to β decay, one has to correct for this energy dependency in the entrance channel for comparison of the level energy profile.

Γ_λ and Δ_λ vary with energy via the penetration and shift functions. The integrant has poles at $E_\pm = E_\lambda \pm \frac{i}{2}\Gamma_\lambda(E_\lambda)$. As for the narrow level case, the path integral along the contour, c, in figure A.2 is performed. The Coulomb functions in the shift and penetration functions are now replaced by the solutions for a complex energy. The asymptotic behaviour of F and G for large ρ are given for real energy solutions in [Lane 1958] III, equations 2.11a and 2.11b. The asymptotic behaviour of the penetration function is therefore determined by $\rho \propto \sqrt{E}$. It seems reasonable that the asymptotic behaviour of complex Coulomb functions is not much different, so $f(E)$ falls off as $\sqrt(E)/E^2$ for $E \to \infty$ and the integral along the arc goes to zero as the radius goes to infinity. $\int_{-\infty}^{\infty} f(E)dE = \int_0^{\infty} f(E)dE$ because $P(E) = 0$ for $E < 0$. The residue is equal to $\frac{1}{2i}$, using formula A.8, and the residue theorem leads to the result,

$$\int_0^{\infty} \frac{\frac{1}{2}\Gamma_\lambda}{|E_\lambda - E + \Delta_\lambda + i\frac{1}{2}\Gamma_\lambda|^2}dE = \pi, \qquad E_\lambda > 0. \tag{A.13}$$

This result has been verified numerically, for example for the single-level approximations of the ground and first-excited states in ^{8}Be.

The result is only valid for positive level energies. For negative E_λ the integrant has a pole of second order on the negative real axis, because $\Gamma_\lambda = 0$ for $E < 0$.

A.3 β-decay phase space

The β particle energy distribution in equation 3.23 is modified by the function $F(Z, E)$, which is the Coulomb correction or Fermi function, which corrects for the modification of the β-particle wave function by the Coulomb field of the nucleus. The Fermi function for a nucleus approximated by a point charge is

given by [Blatt 1952]:

$$F(Z,E) = \frac{2(1+s)}{[(2s)!]^2}(2p\rho)^{2s-2}e^{\pi\eta}\left[(s-1+i\eta)!\right]^2, \tag{A.14}$$

where $s = \sqrt{1-\left(\frac{Ze^2}{\hbar c}\right)^2}$; $\rho = \frac{R}{\hbar/mc}$, R is the nuclear radius and p the electron or positron momentum in units $m_e c$. η is defined as:

$$\eta = \begin{cases} +\frac{Ze^2}{\hbar v} & \beta^- - \text{decay} \\ -\frac{Ze^2}{\hbar v} & \beta^+ - \text{decay}, \end{cases}$$

where v is the electron or positron speed and Z_D is the charge of the daughter nucleus.

The β-decay phase space factor, f_β, provides the phase space available for the β particle and neutrino in the decay. It is calculated by integration of equation 3.23 over all β energies. In this work, the parametrisation in [Wilkinson 1974] has been used, which includes the finite size of the nucleus, screening by atomic electrons and an outer radiative correction:

$$f = S f_{z=0} \tag{A.15}$$

$$f_{z=0} = \frac{1}{60}\left(2W_0^4 - 9W_0^2 - 8\right)p_0 + \frac{1}{4}W_0 \ln\left(W_0 + p_0\right) \tag{A.16}$$

$$\ln S = a_0 + a_1 \ln E_0 + a_2(\ln E_0)^2 + a_3(\ln E_0)^3, \tag{A.17}$$

where E_0 is the electron kinetic energy end point, $Q_\beta - E$, in keV, W_0 is the total electron energy end point in units m_e ,$W_0 = (E_0 + m_e)/m_e$, and $p_0 = (W_0^2 - 1)^{1/2}$. The a_i are tabulated in [Wilkinson 1974].

Bibliography

[Abdurashitov 2002] J. N. Abdurashitov, E. P. Veretenkin, V. M. Vermul, V. N. Gavrin, S. V. Girin, V. V. Gorbachev, P. P. Gurkina, G. T. Zatsepin, T. V. Ibragimova, A. V. Kalikhov, T. V. Knodel, I. N. Mirmov, N. G. Khairnasov, A. A. Shikhin, V. E. Yants, T. J. Bowles, W. A. Teasdale, J. S. Nico, J. F. Wilkerson, B. T. Cleveland, S. R. Elliott and SAGE Collaboration. *Solar neutrino flux measurements by the Soviet-American gallium experiment (SAGE) for half the 22-year solar cycle*. Soviet Journal of Experimental and Theoretical Physics, vol. 95, pages 181–193, August 2002. 43

[Aharmim 2005] B. Aharmim, S. N. Ahmed, A. E. Anthony, E. W. Beier, A. Bellerive, M. Bergevin, S. D. Biller, J. Boger, M. G. Boulay, M. G. Bowler, T. V. Bullard, Y. D. Chan, M. Chen, X. Chen, B. T. Cleveland, G. A. Cox, C. A. Currat, X. Dai, F. Dalnoki-Veress, H. Deng, P. J. Doe, R. S. Dosanjh, G. Doucas, C. A. Duba, F. A. Duncan, M. Dunford and J. A. Dunmore. *Electron energy spectra, fluxes, and day-night asymmetries of ^{8}B solar neutrinos from measurements with NaCl dissolved in the heavy-water detector at the Sudbury Neutrino Observatory*. Physical Review C, vol. 72, no. 5, page 055502, Nov 2005. 44

[Aharmim 2008] B. Aharmim, S. N. Ahmed, J. F. Amsbaugh, A. E. Anthony, J. Banar, N. Barros, E. W. Beier, A. Bellerive, B. Beltran, M. Bergevin, S. D. Biller, K. Boudjemline, M. G. Boulay, T. J. Bowles, M. C. Browne, T. V. Bullard, T. H. Burritt, B. Cai, Y. D. Chan, D. Chauhan, M. Chen, B. T. Cleveland, G. A. Cox-Mobrand, C. A. Currat, X. Dai, H. Deng and J. Detwiler. *Independent Measurement of the Total Active ^{8}B Solar Neutrino Flux Using an Array of ^{3}He Proportional Counters at the Sudbury Neutrino Observatory*. Physical Review Letters, vol. 101, no. 11, page 111301, Sep 2008. 44

[Ahmad 2001] Q. R. Ahmad, R. C. Allen, T. C. Andersen, J. D. Anglin, G. Bühler, J. C. Barton, E. W. Beier, M. Bercovitch, J. Bigu, S. Biller, R. A. Black, I. Blevis, R. J. Boardman, J. Boger, E. Bonvin, M. G. Boulay, M. G.

Bowler, T. J. Bowles, S. J. Brice, M. C. Browne, T. V. Bullard, T. H. Burritt, K. Cameron, J. Cameron, Y. D. Chan, M. Chen and H. H. Chen. *Measurement of the Rate of $\nu_e + d \rightarrow p + p + e^-$ Interactions Produced by ^8B Solar Neutrinos at the Sudbury Neutrino Observatory*. Physical Review Letters, vol. 87, no. 7, page 071301, Jul 2001. 43

[Ajzenberg-Selove 1990] F. Ajzenberg-Selove. *Energy levels of light nuclei* A = 11 – 12. Nuclear Physics A, vol. 506, page 1, 1990. 98, 99, 100, 101, 102, 105

[Alburger 1963] D. E. Alburger. *Beta decay of* B^{12}. Physical Review, vol. 131, no. 4, 1963. 51, 100

[Alburger 1967] D. E. Alburger and D. H. Wilkinson. *Decay of* N^{12}. Physical Review, vol. 153, no. 4, pages 1061–1067, 1967. 103

[Allison 1972] D C S Allison, P G Burke and W D Robb. *R-matrix theory of atomic polarizabilities*. Journal of Physics B: Atomic and Molecular Physics, vol. 5, no. 1, page 55, 1972. 38

[Alpher 1948] R. A. Alpher, H. Bethe and G. Gamow. *The Origin of Chemical Elements*. Physical Review, vol. 73, no. 7, pages 803–804, Apr 1948. 1

[Álvarez Rodriguez 2007] R. Álvarez Rodriguez, E. Garrido, A. S. Jensen, D. V. Fedorov and H. O. U. Fynbo. *Structure of low-lying ^{12}C resonances*. The European Physical Journal A, vol. 31, no. 3, page 303, 2007. 126

[Angulo 1999] C. Angulo. *A compilation of charged-particle induced thermonuclear reaction rates*. Nuclear Physics A, vol. 656, pages 3–183, 1999. 72

[Aymar 1996] M. Aymar, C. H. Greene and E. Luc-Koenig. *Multichannel Rydberg spectroscopy of complex atoms*. Rev. Mod. Phys., vol. 68, no. 4, pages 1015–1123, Oct 1996. 38

[Äystö 2001] J. Äystö. *Development and applications of the* IGISOL *technique*. Nuclear Physics A, vol. 693, pages 477–494, 2001. 45

[B. Jäckel 1987] W. Westmeier B. Jäckel and P. Patzelt. *On the photopeak efficiency of germanium gamma-ray detectors*. Nuclear Instruments and

Methods in Physics Research Section A: Accelerators, Spectrometers, Detectors and Associated Equipment, vol. 261, pages 543–548, 1987. 75

[Bahcall 1996] J. N. Bahcall, E. Lisi, D. E. Alburger, L. De Braeckeleer, S. J. Freedman and J. Napolitano. *Standard neutrino spectrum from ^8B decay*. Physical Review C, vol. 54, no. 1, pages 411–422, Jul 1996. 44

[Balamuth 1974] D. P. Balamuth, R. W. Zurmühle and S. L. Tabor. *Isospin-forbidden alpha decay of the 15.11-MeV state in ^{12}C*. Physical Review C, vol. 10, no. 3, pages 975–986, Sep 1974. 35, 79, 103

[Baluja 1982] K. L. Baluja, P. G. Burke and L. A. Morgan. *R-matrix propagation program for solving coupled second-order differential equations*. Computer Physics Communications, vol. 27, no. 3, pages 299 – 307, 1982. 39

[Barker 1962] F. C. Barker and P. B. Treacy. *Nuclear levels near thresholds*. Nuclear Physics, vol. 38, pages 33–49, 1962. 29

[Barker 1966] F. C. Barker. *Intermediate coupling shell-model calculations for light nuclei*. Nuclear Physics, vol. 83, no. 2, pages 418 – 448, 1966. 48

[Barker 1968] F. C. Barker. *0^+ states of ^8Be*. Australian Journal of Physics, vol. 21, pages 239–257, 1968. 27, 41, 42

[Barker 1969] F. C. Barker. *2^+ states of ^8Be*. Australian Journal of Physics, vol. 22, pages 293–316, 1969. 8, 22, 41, 43, 48, 50, 56, 61, 131

[Barker 1972] F. C. Barker. *The boundary condition parameter in R-matrix theory*. Australian Journal of Physics, vol. 25, pages 341–348, August 1972. 25

[Barker 1975] F. C. Barker. *Isospin Mixing in Nuclear Levels*. Physical Review Letters, vol. 35, no. 9, pages 613–614, Sep 1975. 48

[Barker 1988a] F. C. Barker. *Consistent description of unbound states observed in scattering and reactions*. Australian Journal of Physics, vol. 41, pages 743–763, 1988. 41, 42

[Barker 1988b] F. C. Barker and E. K. Warburton. *The beta-decay of ^8He*. Nuclear Physics A, vol. 487, pages 269–278, 1988. 31

[Barker 1989] F. C. Barker. *Delayed alpha spectra from the beta decay of ^{8}Li and ^{8}B*. Australian Journal of Physics, vol. 42, pages 25–39, 1989. 43, 48, 50, 52, 54, 56, 61, 65, 128, 131

[Barker 1996] F. C. Barker. *The ^{8}He delayed triton spectrum and β-decay to unstable levels*. Nuclear Physics A, vol. 609, no. 1, pages 38 – 42, 1996. 30

[Berg 2006] G.P.A. Berg, O.C. Dermois, U. Dammalapati, P. Dendooven, M.N. Harakeh, K. Jungmann, C.J.G. Onderwater, A. Rogachevskiy, M. Sohani, E. Traykov, L. Willmann and H.W. Wilschut. *Dual magnetic separator for TRIμP*. Nuclear Instruments and Methods in Physics Research Section A: Accelerators, Spectrometers, Detectors and Associated Equipment, vol. 560, no. 2, pages 169 – 181, 2006. 82

[Berrington 1974] K. A. Berrington, P. G. Burke, J. J. Chang, A. T. Chivers, W. D. Robb and K. T. Taylor. *A general program to calculate atomic continuum processes using the R-matrix method*. Computer Physics Communications, vol. 8, no. 3, pages 149 – 198, 1974. 38

[Berrington 1995] K. A. Berrington, W. B. Eissner and P. H. Norrington. *RMATRX1: Belfast atomic R-matrix codes*. Computer Physics Communications, vol. 92, pages 290–420, 1995. 38

[Bethe 1938] H. A. Bethe and C. L. Critchfield. *The Formation of Deuterons by Proton Combination*. Physical Review, vol. 54, no. 4, pages 248–254, Aug 1938. 1

[Bethe 1939] H. A. Bethe. *Energy Production in Stars*. Physical Review, vol. 55, no. 5, pages 434–456, Mar 1939. 1

[Bhattacharya 2002] M. Bhattacharya and E. G. Adelberger. *Reanalysis of $\alpha+\alpha$ scattering and the β-delayed α spectra from ^{8}Li and ^{8}B decays*. Physical Review C, vol. 65, no. 5, page 055502, May 2002. 42, 63

[Bhattacharya 2006] M. Bhattacharya, E. G. Adelberger and H. E. Swanson. *Precise study of the final-state continua in ^{8}Li and ^{8}B decays*. Physical Review C, vol. 73, no. 5, page 055802, May 2006. 27, 42, 43, 44, 52, 64, 65, 66, 105, 131

[Blatt 1952] J. M. Blatt and V. F. Weisskopf. Theoretical nuclear physics. John Wiley & Sons, 1952. 139

[Brune 2002] C. R. Brune. *Alternative parametrization of R-matrix theory*. Physical Review C, vol. 66, page 044611, 2002. 27, 28

[Buchmann 2001] L. Buchmann, E. Gete, J. C. Chow, J. D. King and D. F. Measday. *$\beta-$delayed particle decay of ^9C and the $A = 9$, $T = 1/2$ nuclear system: $R-$matrix fits, the $A = 9$ nuclear system, and the stellar reaction rate of $^4He(\alpha n, \gamma)^9Be$*. Physical Review C, vol. 63, no. 3, page 034303, Feb 2001. 25, 27

[Burbidge 1957] E. M. Burbidge, G. R. Burbidge, William A. Fowler and F. Hoyle. *Synthesis of the Elements in Stars*. Reviews of Modern Physics, vol. 29, no. 4, pages 547–650, Oct 1957. 2

[Burke 1995] V. M. Burke and C. J. Noble. *Farm - A flexible asymptotic R-matrix package*. Computer Physics Communications, vol. 85, no. 3, pages 471 – 500, 1995. 39

[CAEN 2010] CAEN. *www.caen.it/nuclear*, 2010. 86

[Chang 1975] J.-J. Chang. *The R-matrix theory of electron-atom scattering using the Dirac Hamiltonian*. Journal of Physics B: Atomic and Molecular Physics, vol. 8, no. 14, page 2327, 1975. 38

[Chernykh 2007] M. Chernykh, H. Feldmeier, T. Neff, P. von Neumann-Cosel and A. Richter. *Structure of the Hoyle state in ^{12}C*. Physical Review Letters, vol. 98, page 032501, 2007. 5

[Chou 1993] W.-T. Chou, E. K. Warburton and B. A. Brown. *Gamow-Teller beta-decay rates for* A $\leq$ 18 *nuclei*. Physical Review C, vol. 47, no. 1, pages 163–177, 1993. 125, 126

[Cook 1957] C. W. Cook, W. A. Fowler, C. C. Lauritsen and T. Lauritsen. B^{12}, C^{12} *and the Red Giants*. Physical Review, vol. 107, page 508, 1957. 71, 100

[Cook 1958] C. W. Cook, W. A. Fowler, C. C. Lauritsen and T. Lauritsen. *High-Energy Alpha Particles from B^{12}*. Physical Review, vol. 111, no. 2, pages 567–571, Jul 1958. 6, 72, 73, 77, 80, 102

[Cravens 2008] J. P. Cravens, K. Abe, T. Iida, K. Ishihara, J. Kameda, Y. Koshio, A. Minamino, C. Mitsuda, M. Miura, S. Moriyama, M. Nakahata, S. Nakayama, Y. Obayashi, H. Ogawa, H. Sekiya, M. Shiozawa, Y. Suzuki, A. Takeda, Y. Takeuchi, K. Ueshima, H. Watanabe, S. Yamada, I. Higuchi, C. Ishihara, M. Ishitsuka, T. Kajita and K. Kaneyuki. *Solar neutrino measurements in Super-Kamiokande-II*. Physical Review D, vol. 78, no. 3, page 032002, Aug 2008. 44

[Davis 1968] R. Davis, D. S. Harmer and K. C. Hoffman. *Search for Neutrinos from the Sun*. Physical Review Letters, vol. 20, no. 21, pages 1205–1209, May 1968. 43

[Descouvemont 1987] P. Descouvemont and D. Baye. *Microscopic theory of the $^{8}Be(\alpha,\gamma)^{12}C$ reaction in a three-cluster model*. Physical Review C, vol. 36, no. 1, pages 54–59, Jul 1987. 72

[Descouvemont 2006] P. Descouvemont, E. Tursunov and D. Baye. *Three-body continuum states on a Lagrange mesh*. Nuclear Physics A, vol. 765, no. 3-4, pages 370 – 389, 2006. 38

[Descouvemont 2010a] P. Descouvemont. *Three-α continuum states*. Journal of Physics G: Nuclear and Particle Physics, vol. 37, no. 6, page 064010, 2010. 38

[Descouvemont 2010b] P Descouvemont and D Baye. *The R-matrix theory*. Reports on Progress in Physics, vol. 73, no. 3, page 036301, 2010. 38, 39

[Diget 2005] C.Aa. Diget, F.C. Barker, M.J.G. Borge, J. Cederkäll, V.N. Fedosseev, L.M. Fraile, B.R. Fulton, H.O.U. Fynbo, H.B. Jeppesen, B. Jonson, U. Köster, M. Meister, T. Nilsson, G. Nyman, Y. Prezado, K. Riisager, S. Rinta-Antila, O. Tengblad, M. Turrion, K. Wilhelmsen and J. Äystö. *Properties of the ^{12}C 10 MeV state determined through β-decay*. Nuclear Physics A, vol. 760, no. 1-2, pages 3 – 18, 2005. 72, 73, 102, 133

[Diget 2006] C. Aa. Diget. *Beta delayed particle emission: Probing the triple Alpha contiuum*. PhD thesis, University of Aarhus, 2006. 71, 74, 75, 77, 80, 81, 107, 111, 121

[Diget 2009] C. Aa. Diget, F. C. Barker, M. J. G. Borge, R. Boutami, P. Dendooven, T. Eronen, S. P. Fox, B. R. Fulton, H. O. U. Fynbo, J. Huikari, S. Hyldegaard, H. B. Jeppesen, A. Jokinen, B. Jonson, A. Kankainen, I. Moore, A. Nieminen, G. Nyman, H. Penttilä, V. F. E. Pucknell, K. Riisager, S. Rinta-Antila, O. Tengblad, Y. Wang, K. Wilhelmsen and J. Äystö. *Breakup channels for ^{12}C triple-α continuum states*. Physical Review C, vol. 80, no. 3, page 034316, Sep 2009. 77, 80, 105, 107, 110, 111, 132, 133

[Dunbar 1953] D. N. F. Dunbar, R. E. Pixley, W. A. Wenzel and W. Whaling. *The 7.68-Mev State in C^{12}*. Physical Review, vol. 92, no. 3, pages 649–650, Nov 1953. 2, 71

[Epelbaum 2009] E. Epelbaum, H.-W. Hammer and Ulf-G. Meiß ner. *Modern theory of nuclear forces*. Reviews of Modern Physics, vol. 81, no. 4, pages 1773–1825, Dec 2009. 3

[Fayache 1998] M. S. Fayache, E. Moya de Guerra, P. Sarriguren, Y. Y. Sharon and L. Zamick. *Question of low-lying intruder states in ^{8}Be and neighboring nuclei*. Physical Review C, vol. 57, no. 5, pages 2351–2358, May 1998. 42

[Fedorov 2003] D. V. Fedorov, A. S. Jensen and H. O. U. Fynbo. *The widths of the α decaying states of ^{12}C within the three-cluster model*. Nuclear Physics A, vol. 718, pages 685 – 687, 2003. 107

[Freer 2007a] M. Freer. *The clustered nucleus—cluster structures in stable and unstable nuclei*. Reports on Progress in Physics, vol. 70, no. 12, page 2149, 2007. 3

[Freer 2007b] M. Freer, I. Boztosun, C. A. Bremner, S. P. G. Chappell, R. L. Cowin, G. K. Dillon, B. R. Fulton, B. J. Greenhalgh, T. Munoz-Britton, M. P. Nicoli, W. D. M. Rae, S. M. Singer, N. Sparks, D. L. Watson and

D. C. Weisser. *Reexamination of the excited states of ^{12}C*. Physical Review C, vol. 76, no. 3, page 034320, 2007. 72

[Freer 2009] M. Freer, H. Fujita, Z. Buthelezi, J. Carter, R. W. Fearick, S. V. Förtsch, R. Neveling, S. M. Perez, P. Papka, F. D. Smit, J. A. Swartz and I. Usman. *2^+ excitation of the ^{12}C Hoyle state*. Physical Review C, vol. 80, no. 4, page 041303, Oct 2009. 71, 72, 133

[Fukuda 2001] S. Fukuda, Y. Fukuda, M. Ishitsuka, Y. Itow, T. Kajita, J. Kameda, K. Kaneyuki, K. Kobayashi, Y. Koshio, M. Miura, S. Moriyama, M. Nakahata, S. Nakayama, A. Okada, N. Sakurai, M. Shiozawa, Y. Suzuki, H. Takeuchi, Y. Takeuchi, T. Toshito, Y. Totsuka, S. Yamada, S. Desai, M. Earl, E. Kearns, M. D. Messier and K. Scholberg. *Solar ^8B and hep Neutrino Measurements from 1258 Days of Super-Kamiokande Data*. Physical Review Letters, vol. 86, no. 25, pages 5651–5655, Jun 2001. 43

[Fynbo 2003] H. O. U. Fynbo. *Clarification of the Three-Body Decay of ^{12}C (12.71 MeV)*. Physical Review Letters, vol. 91, no. 8, page 082502, 2003. 35, 79

[Fynbo 2005] H. O. U. Fynbo, C. Aa. Diget, U. C. Bergmann, M. J. G. Borge, J. Cederkäll, P. Dendooven, L. M. Fraile, S. Franchoo, N. Fedosseev, B. R. Fulton, W. Huang, J. Huikari, H. B. Jeppesen, A. S. Jokinen, P. Jones, B. Jonson, U. Köster, K. Langanke, M. Meister, T. Nilsson, G. Nyman, Y. Prezado, K. Riisager, S. Rinta-Antila, O. Tengblad, M. Turrion, Y. Wang, L. Weissman, K. Wilhelmsen, J. Äystö and The ISOLDE Collaboration. *Revised rates for the stellar triple-α process from measurement of ^{12}C nuclear resonances*. Nature, vol. 433, pages 136–139, 2005. 73

[Glass 1963] Neel W. Glass and Robert W. Peterson. *Direct Comparison of the B^{12} and N^{12} Beta Spectra*. Physical Review, vol. 130, no. 1, pages 299–305, Apr 1963. 101, 102

[Griffy 1960] T.A. Griffy and L.C. Biedenharn. *Beta decay involving the $Be^{8*}(2^+)$ state*. Nuclear Physics, vol. 15, pages 636 – 645, 1960. 51

[GSL 2010] Gnu Scientific Library. GSL. *http://www.gnu.org/software/gsl/manual/html_node/Coulomb-Wave-Functions.html*, 2010. 135

[Hafstad 1938] L. R. Hafstad and E. Teller. *The Alpha-Particle Model of the Nucleus*. Physical Review, vol. 54, no. 9, pages 681–692, Nov 1938. 4

[Hampel 1999] W. Hampel, J. Handt, G. Heusser, J. Kiko, T. Kirsten, M. Laubenstein, E. Pernicka, W. Rau, M. Wojcik, Y. Zakharov, R. von Ammon, K. H. Ebert, T. Fritsch, D. Heidt, E. Henrich, L. Stieglitz, F. Weirich, M. Balata, M. Sann, F. X. Hartmann, E. Bellotti, C. Cattadori, O. Cremonesi, N. Ferrari, E. Fiorini, L. Zanotti, M. Altmann, F. von Feilitzsch, R. Mössbauer, S. Wanninger, G. Berthomieu, E. Schatzman, I. Carmi, I. Dostrovsky, C. Bacci, P. Belli, R. Bernabei, S. D'Angelo, L. Paoluzi, M. Cribier, J. Rich, M. Spiro, C. Tao, D. Vignaud, J. Boger, R. L. Hahn, J. K. Rowley, R. W. Stoenner and J. Weneser. *GALLEX solar neutrino observations: results for GALLEX IV.* Physics Letters B, vol. 447, pages 127–133, February 1999. 43

[Harakeh 2001] M. N. Harakeh and A. van der Woude. Giant resonances: fundamental high-frequency modes of nuclear excitation. Oxford University Press, 2001. 36

[Hardy 2005] J. C. Hardy and I. S. Towner. *Superallowed* $0^+ \rightarrow 0^+$ *nuclear* β *decays: A critical survey with tests of the conserved vector current hypothesis and the standard model*. Physical Review C, vol. 71, no. 5, page 055501, May 2005. 24

[Haxel 1949] O. Haxel, J. H. D. Jensen and H. E. Suess. *On the "Magic Numbers" in Nuclear Structure*. Physical Review, vol. 75, no. 11, page 1766, Jun 1949. 3

[Hinterberger 1978] F. Hinterberger, P. D. Eversheim, P. Von Rossen, B. Schüller, R. Schönhagen, M. Thenée, R. Görgen, T. Braml and H. J. Hartmann. *The* $\alpha + \alpha \rightarrow^8$*Be double resonance at the 16.6 and 16.9 MeV levels*. Nuclear Physics A, vol. 299, no. 3, pages 397 – 411, 1978. 49, 50, 52

[Hodgson 1997] P. E. Hodgson, E. Gadioli and E. Gadioli Erba. Introductory nuclear physics. Oxford University Press, 1997. 6

[Hosaka 2006] J. Hosaka, K. Ishihara, J. Kameda, Y. Koshio, A. Minamino, C. Mitsuda, M. Miura, S. Moriyama, M. Nakahata, T. Namba, Y. Obayashi, N. Sakurai, A. Sarrat, M. Shiozawa, Y. Suzuki, Y. Takeuchi, S. Yamada, I. Higuchi, M. Ishitsuka, T. Kajita, K. Kaneyuki, G. Mitsuka, S. Nakayama, H. Nishino, A. Okada, K. Okumura and C. Saji. *Solar neutrino measurements in Super-Kamiokande-I*. Phys. Rev. D, vol. 73, no. 11, page 112001, Jun 2006. 44

[Hoyle 1953] F. Hoyle, D. N. F. Dunbar, W. A. Wenzel and W. Whaling. *A state in* C^{12} *predicted from astrophysical evidence*. Physical Review, vol. 92, page 1095c, 1953. 2, 71

[Humblet 1990] J. Humblet. *K-matrix analysis of resonance nuclear reactions*. Physical Review C, vol. 42, no. 4, pages 1582–1591, Oct 1990. 27

[Humblet 1998] J. Humblet, A. Csótó and K. Langanke. *R-matrix and K-matrix analysis of elastic* $\alpha - \alpha$ *scattering*. Nuclear Physics A, vol. 638, no. 3-4, pages 714 – 726, 1998. 27, 42

[Hyldegaard 2009a] S. Hyldegaard, C. Aa. Diget, M. J. G. Borge, R. Boutami, P. Dendooven, T. Eronen, S. P. Fox, L. M. Fraile, B. R. Fulton, H. O. U. Fynbo, J. Huikari, H. B. Jeppesen, A. S. Jokinen, B. Jonson, A. Kankainen, I. Moore, G. Nyman, H. Penttilä, K. Peräjärvi, K. Riisager, S. Rinta-Antila, O. Tengblad, Y. Wang, K. Wilhelmsen and J. Äystö. *Branching ratios in the* β *decays of* ^{12}N *and* ^{12}B. Physical Review C, vol. 80, no. 4, page 044304, Oct 2009. 82

[Hyldegaard 2009b] S. Hyldegaard, C. Forssén, C.Aa. Diget, M. Alcorta, F.C. Barker, B. Bastin, M.J.G. Borge, R. Boutami, S. Brandenburg, J. Büscher, P. Dendooven, P. Van Duppen, T. Eronen, S. Fox, B.R. Fulton, H.O.U. Fynbo, J. Huikari, M. Huyse, H.B. Jeppesen, A. Jokinen, B. Jonson, K. Jungmann, A. Kankainen, O. Kirsebom, M. Madurga, I. Moore, P. Navrátil, T. Nilsson, G. Nyman, G.J.G. Onderwater, H. Penttilä, K. Peräjärvi, R. Raabe, K. Riisager, S. Rinta-Antila, A. Rogachevskiy,

A. Saastamoinen, M. Sohani, O. Tengblad, E. Traykov, J.P. Vary, Y. Wang, K. Wilhelmsen, H.W. Wilschut and J. Äystö. *Precise branching ratios to unbound ^{12}C states from ^{12}N and ^{12}B β-decays*. Physics Letters B, vol. 678, no. 5, pages 459 – 464, 2009. 5, 99, 123, 124, 125

[Hyldegaard 2010] S. Hyldegaard, M. Alcorta, B. Bastin, M. J. G. Borge, R. Boutami, S. Brandenburg, J. Büscher, P. Dendooven, C. Aa. Diget, P. Van Duppen, T. Eronen, S. P. Fox, L. M. Fraile, B. R. Fulton, H. O. U. Fynbo, J. Huikari, M. Huyse, H. B. Jeppesen, A. S. Jokinen, B. Jonson, K. Jungmann, A. Kankainen, O. S. Kirsebom, M. Madurga, I. Moore, A. Nieminen and T. Nilsson. *R-matrix analysis of the β decays of ^{12}N and ^{12}B*. Physical Review C, vol. 81, no. 2, page 024303, Feb 2010. 42, 105

[Ikeda 1963] K. Ikeda, S. Fujii and J. I. Fujita. *The (p,n) reactions and beta decays*. Physics Letters, vol. 3, no. 6, pages 271 – 272, 1963. 37

[Ikeda 1968] K. Ikeda, N. Takigawa and H. Horiuchi. *The Systematic Structure-Change into the Molecule-like Structures in the Self-Conjugate 4n Nuclei*. Progress of Theoretical Physics Supplement, vol. E68, pages 464–475, 1968. 4

[ISOLDE 2010] ISOLDE. *http://isolde.web.cern.ch/ISOLDE/*, 2010. 7

[Itoh 2004] M. Itoh. *Study of the cluster state at* $E_x = 10.3$ MeV *in* ^{12}C. Nuclear Physics A, vol. 738, pages 268–272, 2004. 72, 133

[John 2003] Bency John, Y. Tokimoto, Y.-W. Lui, H. L. Clark, X. Chen and D. H. Youngblood. *Isoscalar electric multipole strength in ^{12}C*. Physical Review C, vol. 68, no. 1, page 014305, Jul 2003. 72

[Kanada-En'yo 1998] Y. Kanada-En'yo. *Variation after Angular Momentum Projection for the Study of Excited States Based on Antisymmetrized Molecular Dynamics*. Physical Review Letters, vol. 81, no. 24, pages 5291–3, 1998. 123, 124

[Kanada-En'yo 2007] Y. Kanada-En'yo. *The Structure of Ground and Excited States of ^{12}C*. Progress of theoretical physics, vol. 117, no. 4, pages 655–680, 2007. 123, 124

[Kankainen 2006] A. Kankainen, T. Eronen, S. P. Fox, H. O. U. Fynbo, U. Hager, J. Hakala, J. Huikari, D. G. Jenkins, A. Jokinen, S. Kopecky, I. Moore, A. Nieminen, H. Penttilä, S. Rinta-Antila, O. Tengblad, Y. Wang and J. Äystö. *Excited states in* ^{31}S *studied via beta decay of* ^{31}Cl. The European Physical Journal A, vol. 27, no. 1, page 67, 2006. 75

[Kirsebom 2009] O.S. Kirsebom, M. Alcorta, M.J.G. Borge, M. Cubero, C.A. Diget, R. Dominguez-Reyes, L. Fraile, B.R. Fulton, H.O.U. Fynbo, D. Galaviz, G. Garcia, S. Hyldegaard, H.B. Jeppesen, B. Jonson, P. Joshi, M. Madurga, A. Maira, A. Muñoz, T. Nilsson, G. Nyman, D. Obradors, A. Perea, K. Riisager, O. Tengblad and M. Turrion. *Observation of γ-delayed 3α breakup of the 15.11 and 12.71 MeV states in* ^{12}C. Physics Letters B, vol. 680, no. 1, pages 44 – 49, 2009. 7, 133

[Kirsebom 2010a] O. S. Kirsebom. PhD thesis, Aarhus University, 2010. 47, 67

[Kirsebom 2010b] O. S. Kirsebom, M. Alcorta, M. J. G. Borge, M. Cubero, C. A. Diget, R. Dominguez-Reyes, L. M. Fraile, B. R. Fulton, H. O. U. Fynbo, S. Hyldegaard, B. Jonson, M. Madurga, A. Muñoz Martin, T. Nilsson, G. Nyman, A. Perea, K. Riisager and O. Tengblad. *Breakup of* ^{12}C *resonances into three α particles*. Physical Review C, vol. 81, no. 6, page 064313, Jun 2010. 79, 81

[Krige 1996] J. Krige, editeur. History of cern, volume 3. Elsevier Science B. V., 1996. 6

[Kurokawa 2004] C. Kurokawa and K. Kato. *Three-alpha resonances in* ^{12}C. Nuclear Physics A, vol. 738, pages 455 – 458, 2004. Proceedings of the 8th International Conference on Clustering Aspects of Nuclear Structure and Dynamics. 126

[Lane 1958] A. M. Lane and R. G. Thomas. *R-Matrix Theory of Nuclear Reactions*. Reviews of Modern Physics, vol. 30, no. 2, pages 257–353, 1958. 8, 11, 19, 21, 25, 26, 33, 36, 38, 127, 135, 138

[Light 1976] John C. Light and Robert B. Walker. *An R matrix approach to the solution of coupled equations for atom-molecule reactive scattering*. The Journal of Chemical Physics, vol. 65, no. 10, pages 4272–4282, 1976. 39

[Mayer-Kuckuk 1962] T. Mayer-Kuckuk and F. C. Michel. *Comparison of the Beta Spectra of B^{12} and N^{12}*. Physical Review, vol. 127, no. 2, pages 545–554, Jul 1962. 101, 102

[Mayer 1949] Maria Goeppert Mayer. *On Closed Shells in Nuclei. II*. Physical Review, vol. 75, no. 12, pages 1969–1970, Jun 1949. 3

[mesytec 2010] mesytec. *www.mesytec.com*, 2010. 85

[Michel 2007] N. Michel. *Precise Coulomb wave functions for a wide range of complex l, η and z*. Computer Physics Communications, vol. 176, no. 3, pages 232 – 249, 2007. 135

[Minuit2 2010] Minuit2. *http://seal.web.cern.ch/seal/MathLibs/Minuit2/html/*, 2010. 51

[Morinaga 1956] H. Morinaga. *Interpretation of Some of the Excited States of 4n Self-Conjugate Nuclei*. Physical Review, vol. 101, no. 1, pages 254–258, Jan 1956. 71

[Morinaga 1966] H. Morinaga. *On the spin of a broad state around 10 MeV in ^{12}C*. Physics Letters, vol. 21, no. 1, pages 78 – 79, 1966. 72

[Napolitano 1987] J. Napolitano, S. J. Freedman and J. Camp. *Beta and neutrino spectra in the decay of ^{8}B*. Physical Review C, vol. 36, no. 1, pages 298–302, Jul 1987. 44

[Navrátil 1998] P. Navrátil and B. R. Barrett. *Large-basis shell-model calculations for p-shell nuclei*. Physical Review Letters, vol. 57, no. 6, pages 3119–3128, Jun 1998. 42

[Navrátil 2000] P. Navrátil, J. P. Vary and B. R. Barrett. *Large-basis ab initio no-core shell model and its application to ^{12}C*. Physical Review C, vol. 62, no. 5, page 054311, Oct 2000. 42

[Navrátil 2003] P. Navrátil and W. E. Ormand. *Ab initio shell model with a genuine three-nucleon force for the p-shell nuclei*. Physical Review C, vol. 68, no. 034305, pages 1–13, 2003. 42, 123, 124, 125

[Navrátil 2007] P. Navrátil, V. G. Gueorguiev, J. P. Vary, W. E. Ormand and A. Nogga. *Structure of $A = 10 - 13$ Nuclei with Two- Plus Three-Nucleon Interactions from Chiral Effective Field Theory*. Physical Review Letters, vol. 99, no. 4, page 042501, Jul 2007. 123

[NNDC 2010] NNDC. *http://www.nndc.bnl.gov/nudat2/*, 2010. 2

[Okolowicz 2003] J. Okolowicz, M. Ploszajczak and I. Rotter. *Dynamics of quantum systems embedded in a continuum*. Physics Reports, vol. 374, no. 4-5, pages 271 – 383, 2003. 129

[Ortiz 2000] C. E. Ortiz, A. García, R. A. Waltz, M. Bhattacharya and A. K. Komives. *Shape of the ^{8}B Alpha and Neutrino Spectra*. Phys. Rev. Lett., vol. 85, no. 14, pages 2909–2912, Oct 2000. 44, 64, 65, 66

[Osterfeld 1992] F. Osterfeld. *Nuclear spin and isospin excitations*. Reviews of Modern Physics, vol. 64, no. 2, pages 491–557, Apr 1992. 36

[Page 2005] P. R. Page. *New broad ^{8}Be nuclear resonances*. Physical Review C, vol. 72, no. 5, page 054312, Nov 2005. 42

[Pieper 2004] Steven C. Pieper, R. B. Wiringa and J. Carlson. *Quantum Monte Carlo calculations of excited states in $A = 6 - 8$ nuclei*. Physical Review C, vol. 70, no. 5, page 054325, Nov 2004. 42

[Prezado 2005] Y. Prezado, M.J.G. Borge, C.Aa. Diget, L.M. Fraile, B.R. Fulton, H.O.U. Fynbo, H.B. Jeppesen, B. Jonson, M. Meister, T. Nilsson, G. Nyman, K. Riisager, O. Tengblad and K. Wilhelmsen. *Low-lying resonance states in the ^{9}Be continuum*. Physics Letters B, vol. 618, no. 1-4, pages 43 – 50, 2005. 129

[Raabe 2008] R. Raabe, A. Andreyev, M. J. G. Borge, L. Buchmann, P. Capel, H. O. U. Fynbo, M. Huyse, R. Kanungo, T. Kirchner, C. Mattoon, A. C. Morton, I. Mukha, J. Pearson, J. Ponsaers, J. J. Ressler, K. Riisager, C. Ruiz, G. Ruprecht, F. Sarazin, O. Tengblad, P. Van Duppen and P. Walden. *β-Delayed Deuteron Emission from ^{11}Li: Decay of the Halo*. Physical Review Letters, vol. 101, no. 21, page 212501, Nov 2008. 129

[Raabe 2009] R. Raabe, J. Büscher, J. Ponsaers, F. Aksouh, M. Huyse, O. Ivanov, S. R. Lesher, I. Mukha, D. Pauwels, M. Sawicka, D. Smirnov, I. Stefanescu, J. Van de Walle, P. Van Duppen, C. Angulo, J. Cabrera, N. de Séréville, I. Martel, A. M. Sánchez-Benítez and C. Aa. Diget. *Measurement of the branching ratio of the ^{6}He β-decay channel into the α + d continuum*. Physical Review C, vol. 80, no. 5, page 054307, Nov 2009. 129

[Reisman 1970] F. D. Reisman, I. Connors and J. B. Marion. *$J^{\pi} = 1^{+}$ isospin doublet in ^{12}C*. Nuclear Physics A, vol. 153, pages 244–254, 1970. 103

[Rolfs 1988] C. E. Rolfs and W. S. Rodney. Cauldrons in the cosmos. The University of Chicago Press, 1988. 1

[ROOT 2010] ROOT. *http://root.cern.ch/*, 2010. 51

[Ruckstuhl 1984] W. Ruckstuhl, B. Aas, W. Beer, I. Beltrami, K. Bos, P. F. A. Goudsmit, H. J. Leisi, G. Strassner, A. Vacchi, F. W. N. De Boer, U. Kiebele and R. Weber. *Precision measurement of the 2p-1s transition in muonic ^{12}C: Search for new muon-nucleon interactions or accurate determination of the rms nuclear charge radius*. Nuclear Physics A, vol. 430, no. 3, pages 685 – 712, 1984. 26

[Schwalm 1966] D. Schwalm and B. Povh. *Alpha Particles Following the β-decay of ^{12}B and ^{12}N*. Nuclear Physics, vol. 89, pages 401–411, 1966. 6, 72, 73, 77, 79, 80, 102, 103

[Sellin 1992] P. J. Sellin, P. J. Woods, D. Branford, T. Davinson, N. J. Davis, D. G. Ireland, K. Livingston, R. D. Page, A. C. Shotter, S. Hofmann, R. A. Hunt, A. N. James, M. A. C. Hotchkis, M. A. Freer and S. L. Thomas. *A double-sided silicon strip detector system for proton radioactivity studies*. Nuclear Instruments and Methods in Physics Research Section A: Accelerators, Spectrometers, Detectors and Associated Equipment, vol. 311, no. 1-2, pages 217 – 223, 1992. 83

[Smirnov 2005] D. Smirnov, F. Aksouh, S. Dean, H. De Witte, M. Huyse, O. Ivanov, P. Mayet, I. Mukha, R. Raabe, J.-C. Thomas, P. Van Duppen, C. Angulo, J. Cabrera, A. Ninane and T. Davinson. *Application of a*

thin double-sided microstrip detector for the registration of β-delayed charge particles: The ^{6}He β decay into the two-body continuum of ^{6}Li. Nuclear Instruments and Methods in Physics Research Section A: Accelerators, Spectrometers, Detectors and Associated Equipment, vol. 547, no. 2-3, pages 480 – 489, 2005. 83

[Smirnova 2003] N. A. Smirnova and C. Volpe. *On the asymmetry of Gamow–Teller β-decay rates in mirror nuclei in relation with second-class currents*. Nuclear Physics A, vol. 714, pages 441–462, 2003. 125, 126

[SRIM 2006] SRIM. *http://www.srim.org/*, 2006. 86

[Suzuki 2003] T. Suzuki, R. Fujimoto and T. Otsuka. *Gamow-Teller transitions and magnetic properties of nuclei and shell evolution*. Physical Review C, vol. 67, no. 044302, pages 1–15, 2003. 125, 126

[Teichmann 1952] T. Teichmann and E. P. Wigner. *Sum Rules in the Dispersion Theory of Nuclear Reactions*. Physical Review, vol. 87, no. 1, pages 123–135, Jul 1952. 36

[Thompson 1985] I. J. Thompson and A. R. Barnett. *COULCC: A continued-fraction algorithm for Coulomb functions of complex order with complex arguments*. Computer Physics Communications, vol. 36, no. 4, pages 363 – 372, 1985. 135

[Thompson 1986] I. J. Thompson and A. R. Barnett. *Coulomb and Bessel functions of complex arguments and order*. Journal of Computational Physics, vol. 64, page 490, 1986. 135

[Thompson 2000] I. J. Thompson, B. V. Danilin, V. D. Efros, J. S. Vaagen, J. M. Bang and M. V. Zhukov. *Pauli blocking in three-body models of halo nuclei*. Physical Review C, vol. 61, no. 2, page 024318, Jan 2000. 38

[Tilley 2002] D. R. Tilley, C. M. Cheves, J. L. Godwin, G. M. Hale, H. M. Hofmann, J. H. Kelley, C. G. Sheu and H. R. Weller. *Energy levels of light nuclei A=5, 6, 7*. Nuclear Physics A, vol. 708, no. 1-2, pages 3 – 163, 2002. 67

[Tilley 2004] D.R. Tilley, J.H. Kelley, J.L. Godwin, D.J. Millener, J.E. Purcell, C.G. Sheu and H.R. Weller. *Energy levels of light nuclei A=8,9,10*. Nuclear Physics A, vol. 745, no. 3-4, pages 155 – 362, 2004. 45, 105

[Vogt 1962] E. Vogt. *Theory of Low Energy Nuclear Reactions*. Reviews of Modern Physics, vol. 34, no. 4, page 723, 1962. 11

[Vogt 2004] E. Vogt. *R-Matrix Theory*. Lecture notes for the R-Matrix School of the Joint Institute for Nuclear Astrophysics at Notre Dame University, South Bend Indiana, 2004. 11

[Warburton 1986] E. K. Warburton. *R-matrix analysis of the $\beta^{\mp}$-delayed alpha spectra from the decay of ^{8}Li and ^{8}B*. Physical Review C, vol. 33, no. 1, pages 303–313, Jan 1986. 42, 43, 49, 52, 53, 61, 120, 131

[Warburton 1992] E. K. Warburton and B. A. Brown. *Effective interactions for the 0p1sd nuclear shell-model space*. Physical Review C, vol. 46, no. 3, pages 923–944, Sep 1992. 125

[Wigner 1947] E. P. Wigner and L. Eisenbud. *Higher Angular Momenta and Long Range Interaction in Resonance Reactions*. Physical Review, vol. 72, no. 1, pages 29–41, Jul 1947. 128

[Wilkinson 1963] D. H. Wilkinson, D. E. Alburger, A. Gallmann and P. F. Donovan. *Alpha-Particle Emission in the Decays of* B^{12} *and* N^{12}. Physical Review, vol. 130, no. 5, pages 1953–1960, 1963. 6, 72, 73, 77, 79, 80, 102, 103, 107

[Wilkinson 1971] D. H. Wilkinson and D. E. Alburger. *β decay of* ^{8}Li *and* ^{8}B*: The second-class current problem*. Physical Review Letters, vol. 26, no. 18, pages 1127–1130, 1971. 6, 64, 65, 104, 128

[Wilkinson 1974] D. H. Wilkinson and B. E. F. Macefield. *A parametrization of the phase space factor for allowed β-decay*. Nuclear Physics A, vol. 232, pages 58–92, 1974. 139

[Wilkinson 2000] D. H. Wilkinson. *Limits to second-class nucleonic and mesonic currents*. The European Physical Journal A, vol. 7, pages 307–315, 2000. 104

[Winter 2006] W. T. Winter, S. J. Freedman, K. E. Rehm and J. P. Schiffer. *The ^{8}B neutrino spectrum*. Physical Review C, vol. 73, no. 2, page 025503, Feb 2006. 44, 52, 64, 65, 66, 68, 69, 131, 132

[Wiringa 2000] R. B. Wiringa, Steven C. Pieper, J. Carlson and V. R. Pandharipande. *Quantum Monte Carlo calculations of $A = 8$ nuclei*. Physical Review C, vol. 62, no. 1, page 014001, Jun 2000. 4

[Yao 2006] W-M Yao. *Review of Particle Physics*. Journal of Physics G: Nuclear and Particle Physics, vol. 33, no. 1, page 1, 2006. 24